Chemistry of Boron-Embedded Polycyclic π-Electron Systems

（ホウ素を中心に組み込んだ縮合多環式π電子系化合物の化学）

Kyohei Matsuo
松尾　恭平

Department of Chemistry, Graduate School of Science
Nagoya University

2016

Preface

The studies in this thesis have been carried out under the direction of Professor Dr. Shigehiro Yamaguchi at Nagoya University during April 2010 – March 2016. The studies are concerned with the synthesis and properties of boron-containing π-electron systems.

First of all, the author would like to express his sincerest gratitude to Professor Shigehiro Yamaguchi for his constant guidance, helpful discussions, and precise suggestions throughout the course of this study.

The author also expresses great appreciation to Assistant Professor Shohei Saito for his kind guidance, technical assistance, and valuable discussions.

The author is deeply grateful to Associate Professor Aiko Fukazawa and Masayasu Taki for the valuable suggestion, technical assistance and kind guidance.

The author expresses the appreciation to Professor Kazuo Takimiya and his research group members at RIKEN for their kind guidance and valuable discussion to the research on organic electronic devices.

The author is grateful to Professor Atsuhiro Osuka, Associate Professor Naoki Aratani, and Assistant Professor Takayuki Tanaka at Kyoto University for measurement of variable-temperature UV-Vis absorption spectroscopy. The author thanks to Professor Kunio Awaga, Associate Professor Michio M. Matsushita, Associate Professor Hirofumi Yoshikawa, and Ms. Chihiro Nanjo at Nagoya University for XRD measurements of the thin films.

The author appreciates to Mr. Toshiaki Noda, Ms. Hideko Natsume, Mr. Hisakazu Okamoto, and Ms. Masumi Kosaka for their excellent works of scientific glassware. The author also thanks to Research Center for Materials Science, Nagoya University for the use of chemical instruments. The author thanks to Mr. Tatsuo Hikage for powder XRD measurements. The author is thankful to Assistant Professor Ichiro Hisaki at Osaka University and Assistant Professor Shigeki Mori at Ehime University for their technical advises for X-ray measurements at Spring-8. The author is grateful to Assistant Professor Mitsuo Hara at Nagoya University for his crucial advises for powder XRD measurements.

The author gives his sincere thanks to former and present group members of Yamaguchi laboratory. Dr. Zhou Zuiguo, Dr. Libin Gao, Dr. Achim Bruch, Dr. Benedikt Neue, Dr. Marcel Harhausen, Dr, Zachary Hudson, Dr. Christoph Glotzbach, Dr. Julien Roger, Mr. Andreas Feldmann, Dr. Dou Chuangdong. Mr. Tobias Greulich, Mr Alexander Hübner, Dr. Chunxue Yuan, Dr. Chin-Ming Chou, Dr. Raúl Adler Yañez, Mr. Tobias Schaub, Mr. Soren Mellerup, Dr, Yongfa Xie, Mr. Xiang Li, Dr. Marek Gryzbowski, Dr. Takuhiro

Taniguchi, Dr. Azusa Iida, Dr. Kazuhiro Mouri, Dr. Kazuhiko Nagura, Dr. Tomokatsu Kushida, Dr. Shunpei Nobusue, Ms. Tomomi Atsumi, Mr. Kengo Asai, Mr. Naoya Sugita, Mr. Yuki Nekohashi, Mr. Satoshi Tange, Mr Takafumi Araki, Dr. Kodai Takeda, Dr. Eriko Yamaguchi, Mr. Kenzo Hayashi, Mr. Ken Nakakura, Mr. Daisuke Kishi, Mr. Kyohei Yamamoto, Mr. Kazuki Kimura, Ms. Anna Sekioka, Ms. Ayumi Shuto, Ms. Yuka Kureishi, Mr. Atsushi Hayakawa, Mr. Kousuke Usui, Mr. Toshiki Yoshikawa, Mr. Kazumitsu Minemura, Ms. Eri Tsuzaka, Mr. Hidenori Shirai, Mr. Oshima Hiroya, Mr. Hiroshi Osaki, Mr. masayoshi Mori, Mr. Yuki Yoshida, Ms. Chigusa Mori, Mr. Shinichiro Osumi, Mr. Makoto Adachi, Mr. Naoki Ando, Mr. Naoya Suzuki, Mr. Masahiko Yoshimura, Mr. Hideaki Iwahara, Mr. Ryo Ueno, Mr. Hiroaki Ogasawara, Mr. Akihiro Kashiwagi, Mr. Hiroaki Kawauchi, Mr. Hiroki Soutome, Mr. tomohiro Nakazaki, Ms. Yasuyo Ishio, Ms. Saki Ageyanagi, Mr. Mikinori Ando, Mr. Tomoya Kubota, Ms. Miki Kondo, Mr. Noriyuki Tanabe, Yusuke Toda, Mr. Yasumasa Namba, Mr. Yuki Mori, Mr. Hiroshi Baba, Mr. Yusuke Ito, Ms. Kieko Senda, Ms. Mayu Takekoshi, Mr. Kentaro Matsumoto, Mr. Masaya Yamazawa.

The author is thankful to Ms. Shima Tamaki, Ms. Komina Nakazawa, Ms. Aya Yamamoto, Mamiko Shinzawa, and Yuki Kobayashi for their detailed and kind assistance.

The author acknowledges the Japan Society for the Promotion of Science (JSPS) for the research fellowship for young scientists. The author also acknowledges the Program for Leading Graduate Schools “Integrative Graduate Education and Research Program in Green Natural Science” MEXT, Japan.

The author would like to express the deepest appreciation to his family, Mr. Tatsuyoshi Matsuo, Ms. Hiromi Matsuo, Mr. Ryuhei Matsuo, Mr. Shohei Matsuo, and Ms. Saki Matsuo for their financial support and constant help.

Kyohei Matsuo

Department of Chemistry
Graduate School of Science
Nagoya University
2016

Contents

General Introduction

The development of highly extended π-conjugated molecules with unique properties is a key issue in the current organic chemistry. They have attracted enormous interests from a wide range of research filed because of their electronic, optoelectronic and magnetic properties, which are related to the development of bioimaging probes and organic electronic devices. It is important to optimize the molecular geometries and electronic structures of π-conjugated skeletons for such applications. A number of approaches in the structural modification have been explored in order to afford intriguing properties to π-conjugated systems.

Incorporation of boron atoms into π-electron systems

The introduction of the main group elements is a simple but powerful method for the modification of π-skeleton, which provides significant changes to the electronic structure through an inductive effect and a resonance effect. Many kinds of π-conjugated molecules containing main group elements, such as boron,[1] nitrogen,[2] silicon,[3] phosphorous[4] and sulfur[5] have been synthesized, which display the characteristic properties due to the impact of main group elements.

Among a variety of possible main group elements, boron atom has received particular attention due to its unique characteristics including electron deficiency and Lewis acidity. A tricoordinate and trivalent boron atom, which is isoelectronic to a carbenium ion, has a trigonal planar structure with a vacant p orbital in a charge neutral form. The vacant p orbital interacts with unoccupied π^*-orbitals of π-skeleton on the boron atom, which results in the stabilization of LUMO and therefore enhancing the electron-accepting character (p–π^* conjugation). In addition, the reactivity toward Lewis bases, which have a lone pair of electrons, is acquired, affording corresponding tetracoordinate boron species with a covalent coordinate bond. This coordination number change is reversible and therefore leads to the switching ability of the electronic structure.

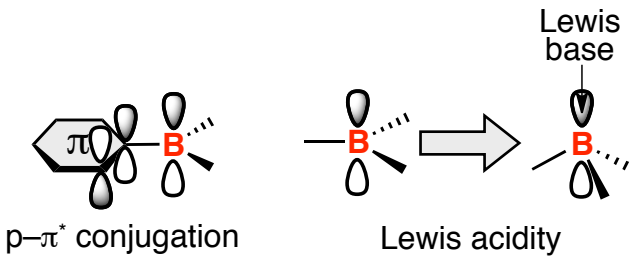

Figure 0-1. Characteristic features of a boron atom for the design of functional π-conjugated systems.

Stabilization of organoboron compounds: Steric protection

One of the critical issues in the development of new boron-containing π-conjugated systems is the intrinsic instability of tricoordinate organoboranes toward oxygen and water. Decomposition reaction easily proceeds through the vacant p orbital of boron, involving the B–C bond cleavage and B–O bond formation due to the high affinity of boron atom toward oxygen atom. One strategy to overcome this problem is the introduction of the bulky substituents to sterically protect the Lewis acidic boron sites. This method is referred as kinetic stabilization. Williams *et al*. demonstrated that organoboron compounds having two mesityl substituents (mesityl = Mes = 2,4,6-trimethylphenyl) on a boron atom were stable to be handled in the air.[6] This dimesitylboryl group (Mes_2B) is often utilized for the simple modification of π-skeletons with a boron atom as an electron-accepting substituent. More bulky substituents including 2,4,6-triisopropylphenyl (Tip) and 2,4,6-tri(*t*-butyl)phenyl (Mes*) groups are also utilized for stabilizing the boron-containing heterocycles, where only one substituent is allowed to be introduced. For example, while dibenzoboroles (9-borafluorenes) show high reactivity because of the electronic contribution of the Hückel 4π antiaromatic character, a corresponding derivative bearing a bulky Tip group on the boron atom is rather stable toward air and moisture.[7] On the other hand, the dibenzoborepin bearing a bulky Mes* group was found to be stable in the air, although another derivative bearing a less bulky Mes group gradually degrades under the same condition.[8]

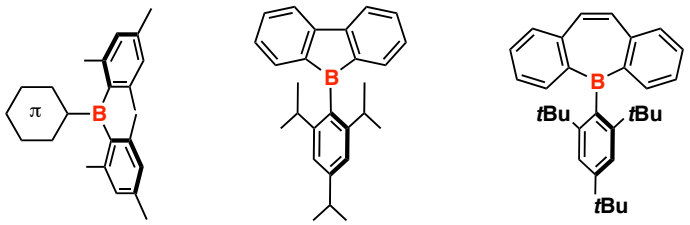

Figure 0-2. Sterically protected organoboron compounds.

Stabilization of organoboron compounds: Introduction of electron-donating atoms

The other approach to stabilize organoboron compounds is the introduction of another heteroatom having a lone pair of electron, such as oxygen and nitrogen atoms. The interaction between the lone pair electron and the vacant p orbital of boron decreases the Lewis acidity. This method is referred as thermodynamic stabilization. Most of the boronic acids and boronic esters are air-stable and employed in the Suzuki-Miyaura cross coupling reactions. Dewar *et al*. reported the synthesis of 9,10-azaboraphenanthrene having a B–N bond, which is stable under the ambient conditions despite the absence of steric protection

around the boron atom.[9]

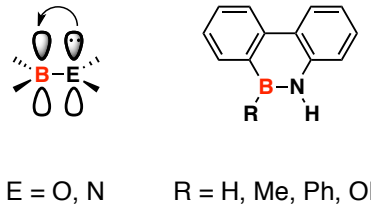

Figure 0-3. Thermodynamic stabilization of organoboron compounds.

Effects of tricoordinate boron in the π-electron systems: Optical properties

Various boron-containing π-conjugated materials with fascinating properties have been designed and synthesized based on the two stabilization methods described previously. For example, Fang *et al*. reported that bis(thienylethenyl)benzene bearing two Mes_2B group at the terminal positions exhibit large two-photon absorption cross section of 1340 GM at 775 nm and high fluorescence quantum yield of 0.61 in THF.[10] Wakamiya and Yamaguchi *et al*. disclosed that 2,2'-bithiophene-based π-conjugated materials possessing the Mes_2B group at the 3-position displayed intense solid-state full-color emissions with a wide range of visible regions.[11] These results are attributed to the strong electron-accepting character of the boryl substituents. On the other hand, replacement of C–C units in π-conjugated systems with the B–N units produces a different effect. Despite their isosterism, the local dipole moment arises and the polarizability of the molecular orbitals change. Piers *et al*. demonstrated that the BN-substituted pyrene analogue, whose C–C bond at its center was replaced with a B–N bond, showed a red-shifted emission in the visible regions compared to that of parent pyrene.[12]

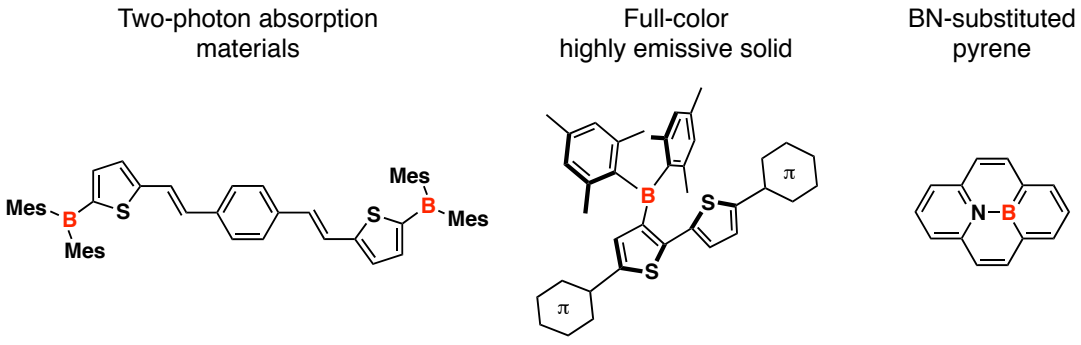

Figure 0-4. Boron-containing π-electron materials.

Effects of tricoordinate boron in the π-electron systems: Lewis acidity

Lewis acidity is also an attractive feature of the boron-containing materials because it enables π-systems to switch the electronic properties by the coordination with Lewis bases

including fluoride ion, cyanide ion and amines, leading to the potential application to chemosensors. Tamao and Yamaguchi *et al*. demonstrated colorimetric sensing of fluoride anions by triarylboranes.[13] While tri(9-anthryl)borane shows an absorption band in the visible region, it disappears and a new band in the UV region increases upon complexation with fluoride ion. Gabbaï *et al*. reported that the triarylborane bearing a cationic ammonium group at *ortho*-position of its boron substituent serves as a fluoride ion sensor even in water.[14] Lee *et al*. reported that the thin film of π-conjugated polymer incorporating borasiloxane cages in the main chain underwent a rapid and reversible color change upon exposure to volatile amines.[15]

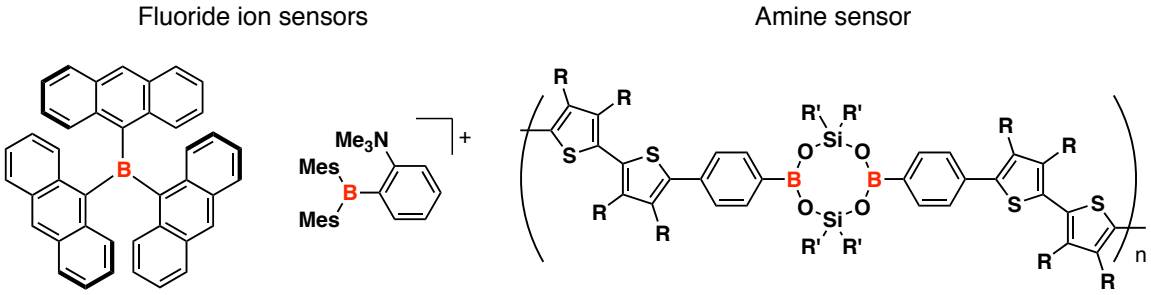

Figure 0-5. Boron-based chemosensors.

Organic electronic materials containing tricoordinate boron atom

Since the boron-containing π-conjugated compounds have low-lying LUMO levels, these materials are attractive in terms of not only intriguing optical properties but also electronic properties. Various types of organic electronic devices consisting of organoboron compounds have been investigated. Among them, application to organic light-emitting diodes (OLEDs) has been the most vigorous area of research. Shirota *et al*. demonstrated that oligothiophenes containing two Mes_2B groups at the terminal positions displayed excellent electron-transporting properties as amorphous materials.[16] The Mes_2B groups are involved in order to reduce the electron-injection barrier and stabilize the amorphous structure as electron-accepting bulky substituents. Tris[3-(3-pyridyl)mesityl]borane was synthesized as an efficient electron-transporting material by Kido *et al*.[17] Its twisted molecular structure is relevant to high triplet excitation energy, which suppresses exothermic reverse energy transfer from emitting materials to this electron-transporting material. Hatakeyama *et al*. disclosed that replacement of a C–C unit with a B–N unit of aromatic compounds is an effective approach to control triplet excitation energy of host materials in the OLED devices.[18] BN-substituted dibenzochrysene analogues exhibit ambipolar carrier transport abilities and higher triplet excitation energies than those of carbon analogues. OLED that employed the BN compounds as host materials showed superior performance over the device

using a representative host material of 4,4'-bis(*N*-carbazolyl)-1,1'-biphenyl.

In comparison with the OLEDs, applications of tricoordinate organoboron compounds in other organic electronic devices, such as organic field-effect transistors (OFETs) and organic photovoltaics (OPVs), are still in infancy. Only nitrogen- or oxygen-stabilized tricoordinate organoboron compounds have been utilized as organic semiconductors for OFETs. This is mainly due to the disadvantages in small orbital overlap between the organoboron molecules in the packing structure. Bulky substituents on the boron atom, which are necessary for the kinetic stabilization of organoboron compounds, decrease the orbital overlap and disturb sufficient charge carrier transport. Yamashita *et al*. reported that OFET devices consisting of organic semiconductors containing 1,3,2-diazaborole units displayed p-type FET performance with hole mobility of up to 1.4×10^{-2} cm^2 V^{-1} s^{-1}.[19]

On the other hand, employment for OPVs has been explored by Shirota *et al*.[20] The pn-heterojunction device consisting of the starburst-type triarylamine bearing Mes_2B groups as a p-type semiconductor and the perylene dye as an n-type semiconductor exhibits photovoltaic effect, although the conversion efficiency was very small (0.1 %). Pignataro *et al*. reported that conjugated polymer incorporating tricoordinate boron atoms in main chain function as an n-type semiconductor in a bulk heterojunction photovoltaic cell with poly(3-hexylthiophene) as a p-type material.[21] These results indicate that electron-accepting character of boron-containing π-electron systems could be utilized for organic semiconductors of OPVs.

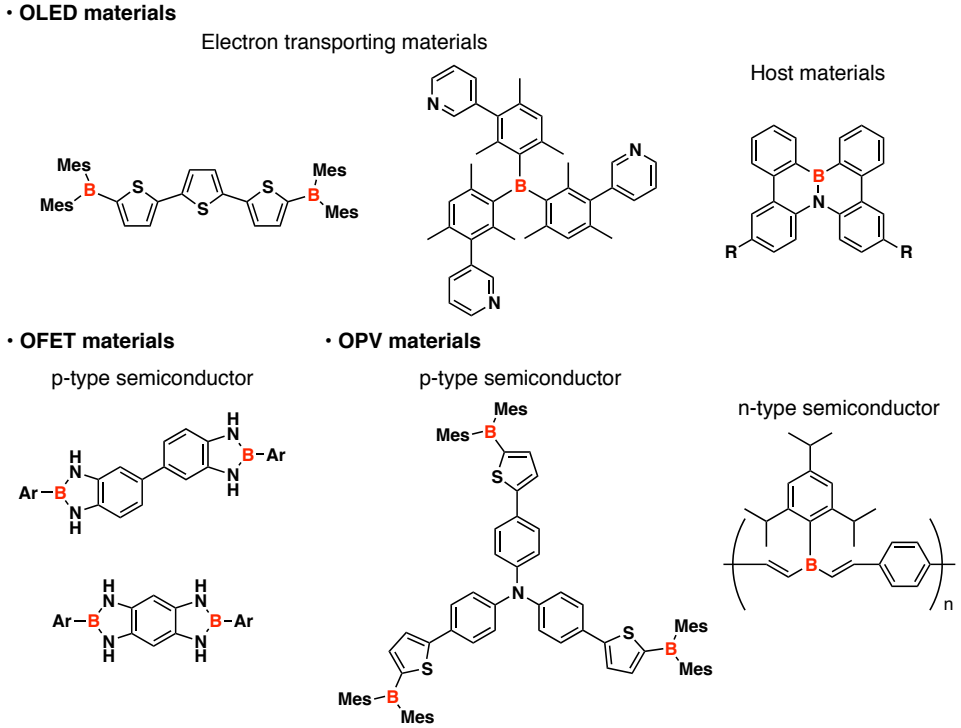

Figure 0-6. Organic electronic materials containing tricoordinate boron atoms.

Structurally constrained triarylboranes

Kinetic and thermodynamic stabilizations of organoboron compounds are practical methods to treat them under ambient conditions. However, there are still several problems in terms of the charge transporting ability. While bulky substituents retain electron-accepting character of boron atoms, they prevent overlapping of π orbitals in the solid state. On the other hand, introduction of heteroatoms possessing lone-pair electrons diminishes the electron deficiency and Lewis acidity of boron atoms despite a lack of steric hindrance. In other words, effective intermolecular interactions of π systems and valuable electronic features of boron atom have been in a trade-off relationship in boron-containing π materials.

Wakamiya and Yamaguchi *et al*. demonstrated that structural constraint, bridging the substituents and making the geometry of boron atom planar, is an alternative strategy for stabilization of organoboron compounds.[22] Planarized triphenylborane, whose phenyl substituents are fixed in a planar fashion with three sp^3-carbon tethers, is synthesized. This compound shows a high stability toward water, oxygen, amines, and silica gel despite the absence of steric protection. This remarkable stability should arise from the unique structural features. Namely, constraints of boron atom to keep planar geometry associate destabilizing tetrahedral structure of tetracoordinate boron in the reaction intermediates during oxidation or hydrolysis. Moreover, bridging the substituents on a boron atom inhibits B–C bond cleavages due to the chelate effect. The completely planar skeleton effectively extends the π-conjugation over the entire molecules through the boron atom and allows it to form π-stacked structure. However, the degree of π-electron delocalization is comparable to that of non-bridged trimesitylborane. The sp^3-carbon bridges do not lead to large perturbation in its absorption wavelength and reduction potential. Moreover, methyl substituents on the bridging sp^3-carbon moieties prevent efficient intermolecular π-orbital interactions in the crystal packing structure. Structural constraint strategy is a promising molecular design in the application for organic electronic devices because there is the potential to achieve the following improvements: high stability, desirable intermolecular interactions for charge transporting ability and intrinsic electronic impacts of boron atoms such as electron-accepting property and Lewis acidity.

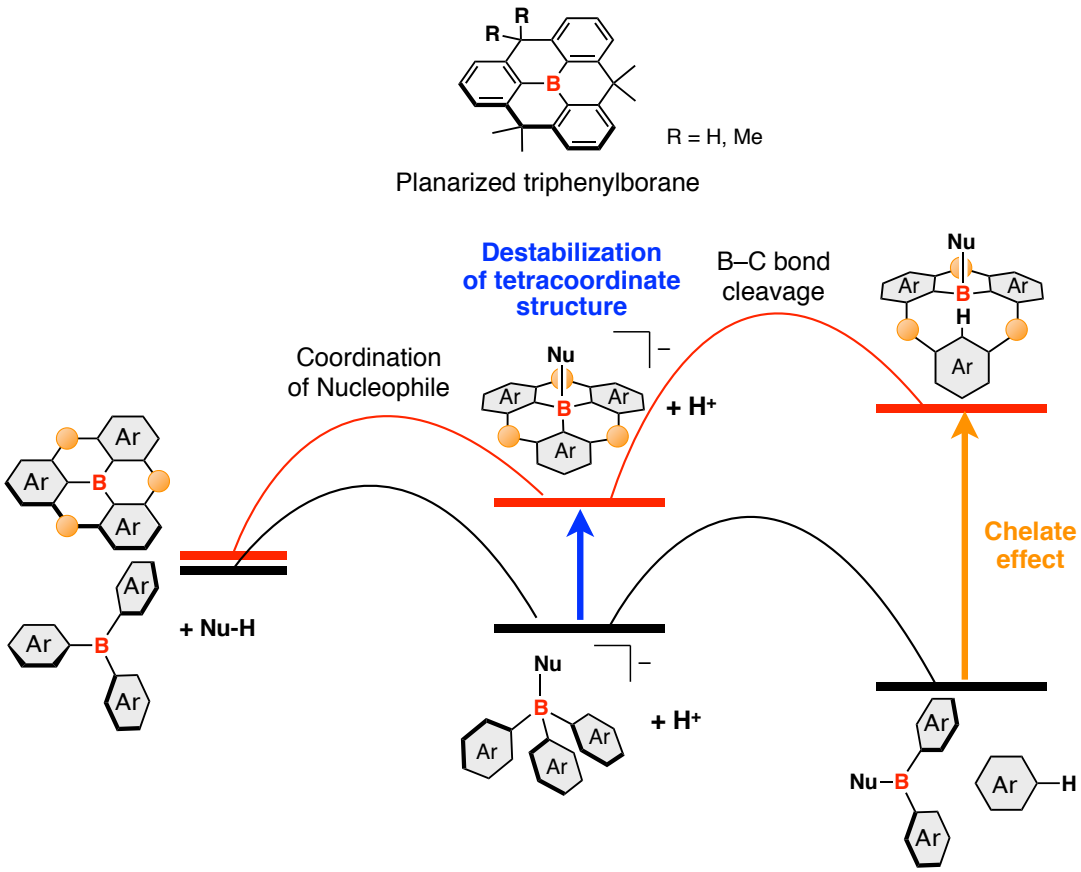

Figure 0-7. Structurally constrained triphenylborane with sp^3-carbon bridges and a postulated energy diagram for the reaction of triarylboranes with a nucleophile.

Survey of this thesis

As described in the previous sections, the key issue for the application to the organic electronic materials of the π-electron systems incorporating the tricoordinate boron atoms is to develop the new molecular design, which acquires high stability, effective intermolecular π-orbital interactions, strong electron-accepting ability, and appropriate Lewis acidity. In this thesis, the author has designed and synthesized the boron-embedded polycyclic π-conjugated systems as sophisticated planarized triarylboranes. The relationship between structures and properties has also been investigated from experimental and theoretical studies. The potential application for organic electronic materials has been explored.

Chapter 1 describes the development of a boron-embedded polycyclic π-conjugated system, in which the three aryl substituents on the boron atom are directly connected to one another through the sp^2-carbon atoms and consequently fully conjugated.[23] This compound shows high stability toward water, oxygen and silica gel despite the absence of steric protection around the boron atom. The highly planar framework with less steric bulkiness achieved unprecedented π-stacked structure in the solid state. Moreover, this 2D expanded π-conjugated molecule displays long-wavelength absorption bands that cover the entire visible region and fluorescence in the visible/near-IR region. In addition, this compound exhibit considerable Lewis acidity despite the rigid planar structure, which causes the formation of Lewis acid–base adducts with pyridine. Since the electronic structures of tri- and tetracoordinate boron species are largely different, its pyridine solution displayed thermochromic behavior in the equilibrium between those species.

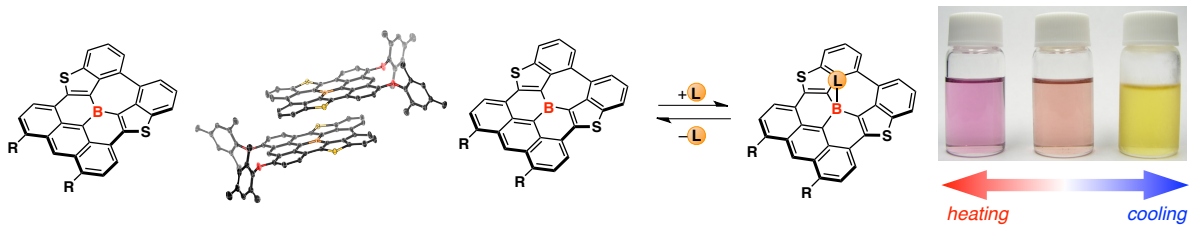

Chapter 2 describes the synthesis of a planarized trinaphthylborane with partially fused ring structure.[24] The smaller structural constraint gives rise to higher Lewis acidity than that of completely fused triarylborane, while high stability toward water and oxygen is maintained. This compound easily produces the Lewis acid–base adducts with pyridine derivatives in solution. The B–N Lewis adducts exhibit unprecedented dissociation behavior in the photoexcitated state, which causes a dual emission arising from the tetracoordinate Lewis

adducts and the photodissociated tricoordinate boranes. In addition, the photodissociation behavior of these systems was found to be strongly dependent on the Lewis basicity of the pyridine derivatives.

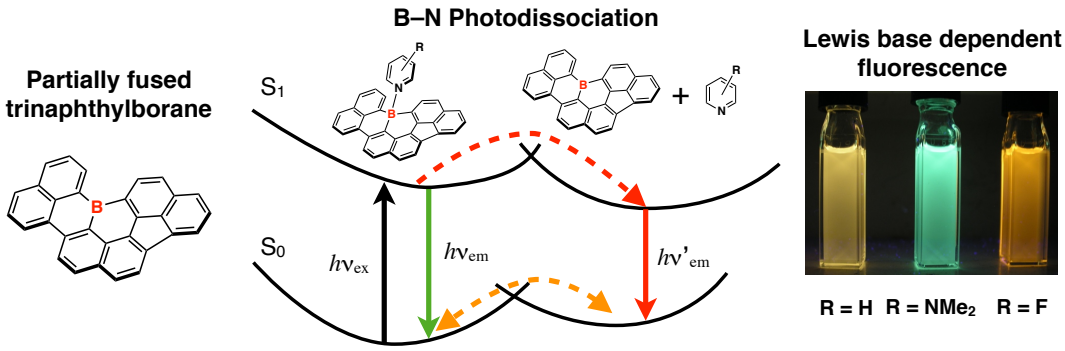

Chapter 3 describes the application of the partially fused trinaphthylborane to solution-processed OFET devices. Its sufficient Lewis acidity leads to temporarily enhanced solubility by reversible B–N coordinate bond formation with pyridine. The coordinating pyridine on the boron atom suppresses its inherent π-stacking feature similar to the function of solubilizing substituent. The amorphous thin films of the Lewis acid–base adducts can be prepared by solution process fabrication. In addition, the coordinating pyridine can be removed by thermal annealing, resulting in conversion into the crystalline thin films of parent tricoordinate boron compounds. The OFET devices consisting of obtained films exhibit typical p-type characteristics with hole mobility of up to 2.5×10^{-4} cm^2 V^{-1} s^{-1}.

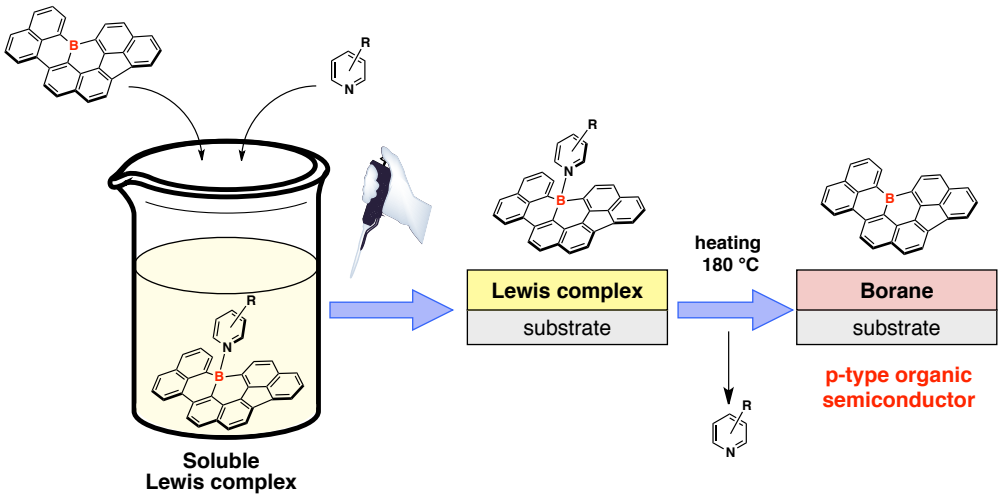

References

(1) (a) Entwistle, C. D.; Marder, T. B. *Chem. Mater.* **2004**, *16*, 4574. (b) Yamaguchi, S.; Wakamiya, A. *Pure Appl. Chem.* **2006**, *78*, 1413. (c) Bosdet, M. J. D.; Piers, W. E. *Can. J. Chem.* **2008**, *86*, 8. (d) Jäkle, F. *Chem. Rev.* **2010**, *110*, 3985. (e) Wade, C. R.; Broomsgrove, A. E. J.; Aldridge, S.; Gabbäi, F. P. *Chem. Rev.* **2010**, *110*, 3958. (f) Hudson, Z. M.; Wang, S. *Dalton Trans.* **2011**, *40*, 7805.

(2) (a) Bunz, U. H. *Pure Appl. Chem.* **2010**, *82*, 953. (b) Richards, G. J.; Hill, J. P.; Mori, T., Ariga, K. *Org. Biomol. Chem.* **2011**, *9*, 5005. (c) Janiga, A.; Gryko, D. T. *Chem. Asian J.* **2014**, *9*, 3036.

(3) (a) Ohshita, J.; Kunui, A. *Acta Polym.* **1998**, *49*, 379. (b) Yamaguchi, S.; Tamao, K. *J. Chem. Soc., Dalton Trans.* **1998**, 3693. (c) Chen, J.; Cao, Y. *Macromol. Rapid Commun.* **2007**, *28*, 1714.

(4) (a) Baumgartner, T.; Réau, R. *Chem. Rev.* **2006**, *106*, 4681. (b) Matano, Y.; Imahori, H. *Org. Biomol. Chem.* **2009**, *7*, 1258. (c) Ren, Y.; Baumgartner, T. *Dalton, Trans.* **2012**, *41*, 7792. (d) Stolar, M.; Baumgartner, T. *Chem. Asian. J.* **2014**, *9*, 1212.

(5) (a) Benedikov, M.; Wudl, F.; Perepichka, D. F. Chem. Rev. 2004, 104, 4891. (b) Iyoda, M.; Hasegawa, M.; Miyake, Y. *Chem. Rev.* **2004**, *104*, 5085. (c) Mishra, A.; Ma, C.-Q.; Bäuerle, P. *Chem. Rev.* **2009**, *109*, 1141. (d) Takimiya, K.; Shinamura, S.; Osaka, I.; Miyazaki, E. *Adv. Mater.* **2011**, *23*, 4347.

(6) Grisdale, P. J.; Williams, J. R. L.; Glogowski, M. E.; Babb, B. E. *J. Org. Chem.* **1971**, *36*, 544.

(7) Yamaguchi, S.; Shirasaka, T.; Akiyama, S.; Tamao, K. *J. Am. Chem. Soc.* **2002**, *124*, 8816.

(8) (a) Mercier, L. G.; Piers, W. E.; Parvez, M. *Angew. Chem. Int. Ed.* **2009**, *48*, 6108. (b) Caruso, Jr., A.; Siegler, M. A.; Tovar, J. D. *Angew. Chem. Int. Ed.* **2010**, *49*, 4213.

(9) Dewar, M. J. S.; Kubba, V. P.; Pettit, R. *J. Chem. Soc.* **1958**, 3073.

(10) Liu, Z.-Q.; Fang, Q.; Cao, D.-X.; Wang, D.; Xu, G.-B. *Org. Lett.* **2004**, *6*, 2933.

(11) Wakamiya, A.; Mori, K.; Yamaguchi, S. *Angew. Chem. Int. Ed.* **2007**, *46*, 4273.

(12) Bosdet, M. J. D.; Piers, W. E.; Sorensen, T. S.; Parves, M. *Angew. Chem. Int. Ed.* **2007**, *46*, 4940.

(13) Yamaguchi, S.; Akiyama, S.; Tamao, K. *J. Am. Chem. Soc.* **2001**, *123*, 11372.

(14) Hudnall, T. W.; Gabbaï, F. P. *J. Am. Chem. Soc.* **2007**, *129,* 11978.

(15) Liu, W.; Pink, M.; Lee, D. *J. Am. Chem. Soc.* **2009**, *131,* 8703.

(16) Noda, T.; Shirota, Y. *J. Am. Chem. Soc.* **1998**, *120,* 9714.

(17) Tanaka, D.; Takeda, T.; Chiba, T.; Watanabe, S.; Kido, J. *Chem. Lett.* **2007**, *36*, 262.

(18) Hashimoto, S.; Ikuta, T.; Shiren, K.; Nakatsuka, S.; Ni, J.; Nakamura, M.; Hatakeyama, T. *Chem. Mater.* **2014**, 26, 6265.

(19) Kojima, T.; Kumaki, D.; Nishida, J.; Tokito, S.; Yamashita, Y. *J. Mater. Chem.* **2011**, *21*, 6607.

(20) Kinoshita, M.; Fujii, N.; Tsuzuki, T.; Shirota, Y. *Synthetic Metals* **2001**, *121*, 1571.

(21) Cataldo, S.; Fabiano, S.; Ferrante, F.; Oreviti, F.; Patanè, S.; Pignataro, B. *Macromol. Rapid Commun.* **2010**, *31*, 1281.

(22) (a) Zhou, Z.; Wakamiya, A.; Kushida, T.; Yamaguchi, S. *J. Am. Chem. Soc.* **2012**, *134,* 4529. (b) Kushida, T.; Zhou, Z.; Wakamiya, A.; Yamaguchi, S. *Chem. Commun.* **2012**, *48*, 10715. (c) Kushida, T.; Yamaguchi, S. *Organometallics* **2013**, *32*, 6654. (d) Shuto, A.; Kushida, T.; Fukushima, T.; Kaji, H.; Yamaguchi, S. *Org. Lett.* **2013**, *15*, 6234. (e) Kushida, T.; Camacho, C.; Shuto, A.; Irle, S.; Muramatsu, M.; Katayama, T.; Ito, S.; Nagasawa, Y.; Miyasaka, H.; Sakuda, E.; Kitamura, N.; Zhou, Z.; Wakamiya, A.; Yamaguchi, S. *Chem. Sci.* **2014**, *5*, 1296.

(23) Saito, S.; Matsuo, K.; Yamaguchi, S. *J. Am. Chem. Soc.* **2012**, *134*, 9130.

(24) Matsuo, K.; Saito, S.; Yamaguchi, S. *J. Am. Chem. Soc.* **2014**, *136*, 12580.

Chapter 1

Polycyclic π-Electron Systems with Boron at its Center

Abstract: A new class of boron-containing π-electron systems, in which the tricoordinate boron atom is embedded in a fully fused polycyclic π-conjugated skeleton, was explored. The compound shows high stability toward oxygen, water, and silica gel, despite the absence of steric protection around the boron atom. Its highly planar structure displays unprecedented face-to-face π-stacking feature in the crystal packing. Reflecting the electron-donating character of effectively expanded π-conjugation and the electron-accepting character of the boron atom, this compound shows broad absorption bands that cover the entire visible region and fluorescence in the visible-near-IR region. In addition, this compound shows dramatic property changes upon formation of the Lewis acid–base adducts, such as thermochromism in the presence of pyridine.

1-1. Introduction

The incorporation of tricoordinate and trivalent boron atoms into π-conjugated systems is a powerful tool to provide the intriguing properties including the strong electron-accepting character and Lewis acidity derived from a vacant p orbital.[1] In designing new π-electron systems incorporating tricoordinate boron atoms, the intrinsic instability of the boron atom toward water and oxygen is the inevitable problem. Two approaches have been generally utilized to overcome that problem. One is the replacement of the carbon atoms bonding to the boron atom with oxygen or nitrogen atoms, which has yielded a number of fascinating π-systems with reasonable stabilities.[2] However, interaction between the lone-pair of the heteroatom and vacant p orbital of the boron atom diminishes the unique characteristics of boron atom. The other approach is introduction of bulky substituents to sterically protect the Lewis acidic boron atom.[3] Although this method can bring out the electron deficiency of boron atom, the structural diversity of organoboron compounds has been greatly limited. There are three types of possible motifs of the boron-containing π-systems (Figure 1-1).[4] First is the installation of the boryl groups into π-systems as the peripheral substituents, in which two bulky substituents such as Mes groups are attached to the boron atom (**A**). Second is the bridging of the bay region of π-systems with the boron atom bearing one bulky substituent (**B**). In other words, the boron-heterocycle was incorporated into the π-systems. Third is the embedding the boron atom into the π-systems at its center (**C**). Steric protection cannot construct the third system, even though that is the most drastic design because all three substituent of the boron atom were employed in its π-conjugation.

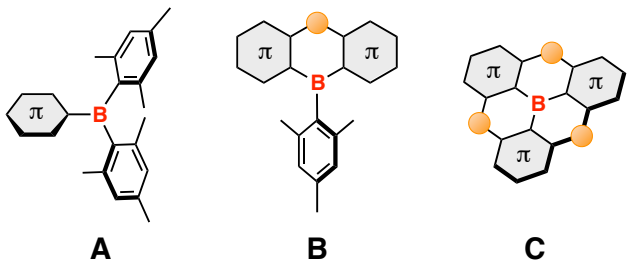

Figure 1-1. Three possible structures of boron-containing π- systems.

Recently, Wakamiya and Yamaguchi *et al*. disclosed the structural constraint as an alternative strategy for stabilizing organoboron compounds in order to construct the boron-embedded π-systems.[5] They synthesized a planarized triphenylborane **1**, whose phenyl substituents are fixed in a planar geometry by three methylene tethers (Figure 1-2).[5a] Compound **1** is stabilized by structural constraint instead of bulky substituent and shows high stability toward water, oxygen, amines, and silica gel. However, as the sp^3-carbon bridges do

not expand the π-conjugation, **1** showed only an absorption band in the UV region. Moreover, the dimethyl groups on the bridging methylene moieties in **1** prevented intermolecular contact in the crystalline state.

To overcome these problems, the author designed a sophisticated planarized triarylborane **2** as a new boron-embedded polycyclic π-conjugated system, in which the all three substituents of the boron atom are directly connected through the sp^2-carbon atoms and consequently fully conjugated to one another (Figure 1-2). Its structural features enables to not only expand the π-electron delocalization effectively but also form a π-stacked structure, which is favorable to effective charge transporting. In addition, this compound can be regarded as a model of a boron-doped graphene. Therefore, the investigation of its properties including molecular structure and Lewis acidity leads to experimental demonstration of the impact of boron-doping into a graphene system at a molecular level. In this chapter, the author described the synthesis, structure, photophysical and electrochemical properties, and Lewis acidity of boron-embedded polycyclic π-conjugated molecules **3**.

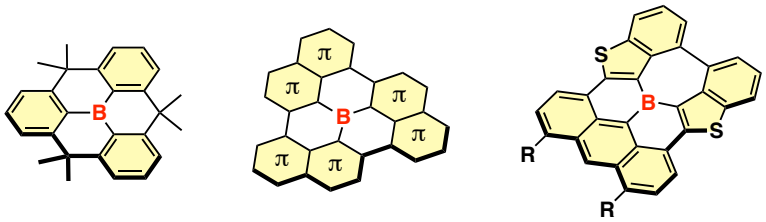

1 **2** **3**

Figure 1-2. Molecular structures of planarized triarylboranes. Reprinted with permission from [22]. Copyright © 2012, American Chemical Society.

1-2. Results and discussion

Synthesis

Initial target molecule for fully π-conjugated triarylborane was completely fused tris(benzo[*b*]thiophen-3-yl)borane **4**. The author envisioned that this skeleton could be synthesized by three-fold intramolecular cross-coupling reactions from tris(4-bromobenzothiophene-3-yl)borane **5** (Scheme 1-1). The precursor **5** was obtained by selective halogen/lithium exchange reaction of 4-bromo-3-iodobenzothiophene **6** with 1 equivalent of *n*-BuLi and following reaction with $BF_3{\cdot}OEt_2$. X-ray crystal structure analysis revealed that precursor **5** has a propeller-like structure suitable for C_3-symmetric three-fold cyclization (Figure 1-3).

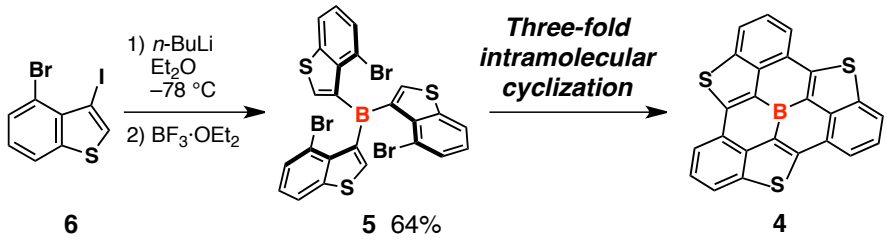

Scheme 1-1. Proposed synthetic route to tris(benzo[*b*]thiophen-3-yl)borane **4**. Reprinted with permission from [22]. Copyright © 2012, American Chemical Society.

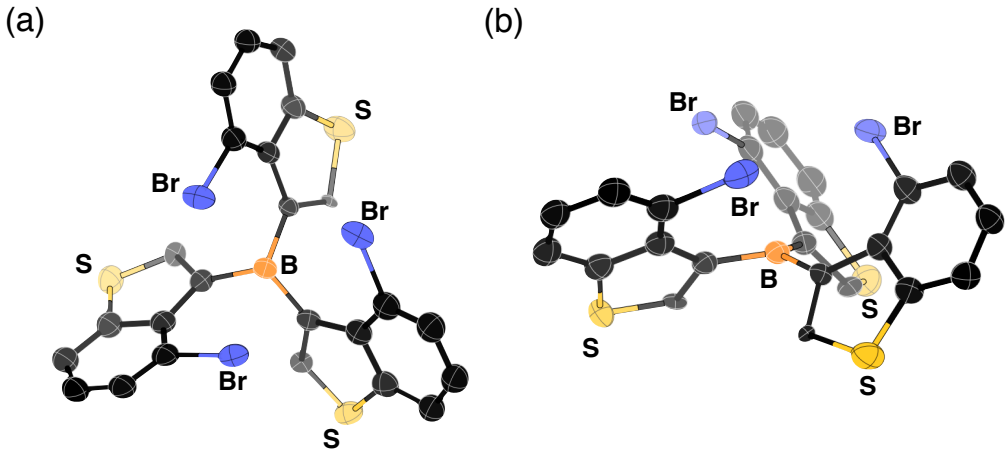

Figure 1-3. Crystal structure of **5** (50% probability of thermal ellipsoids, hydrogen atoms are omitted for clarity): (a) Top view and (b) side view. Reprinted with permission from [22]. Copyright © 2012, American Chemical Society.

At first, intramolecular Pd-catalyzed C–H arylations under various conditions with bases such as K_2CO_3 and DBU were conducted by using precursor **5**.[6] However, undesired products were obtained in these conditions through the Suzuki-Miyaura cross-coupling

reaction via B–C bond cleavage. Therefore, the author next focused on an intramolecular radical cyclization using *n*-Bu_3SnH with 2,2'-azobis(isobtyronitrile) (AIBN) as an initiator because this reaction is conducted in neutral condition.[7] Although this reaction did not produce the target compound, partially fused compound **7**, in which new two C–C bonds were formed, could be isolated in 7% yield (Scheme 1-2). The molecular structure of **7** was estimated from ^{1}H NMR and MS spectroscopy. This result suggested some important implications. Thus, the B–C bonds of the triarylboranes can remain intact under the radical reaction conditions. The homocoupling of the two C–Br bonds precedes the cross-coupling between the C–Br and C–H bonds, resulting in the formation of the seven-membered ring. Moreover, the doubly cyclized product **7** is barely stable in the air enough to isolate.

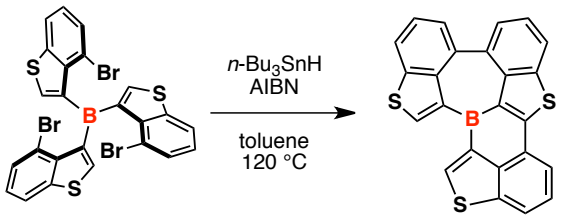

5 **7** 64%

Scheme 1-2. Synthesis of a partially fused tri(benzothienyl)borane **7**. Reprinted with permission from [22]. Copyright © 2012, American Chemical Society.

According to these insights, the author designed next target **3**, which has an anthracene skeleton in place of one of the benzothiophene skeletons (Scheme 1-3). The author planed stepwise intramolecular cyclizations for the synthesis of completely fused product **3**, including the intramolecular homocoupling to construct the same seven-membered ring and following oxidative cyclodehydrogenation for final step.[8] Anthrylbis(4-bromobenzothiophene-3-yl)borane **8** were prepared as the key precursor by halogen/lithium exchange reaction of 4-bromo-3-iodobenzothiophene **6** and following reaction with anthryldimethoxyborane **9**. Radical-promoted intramolecular homocoupling reaction of **8** was then conducted using $(TMS)_3SiH$ with 1,1'-azobis(cyclohexanecarbonitrile) (ABCN) as an initiator to give the cyclized products **10**. Formation of the seven-membered ring consisting of bis(benzothienyl)borane was confirmed by X-ray crystal structure analysis of **10** (Figure 1-4). In addition, the perpendicular arrangement of the anthryl group to the bis(benzothienyl)borane skeleton was revealed. When the oxidative cyclodehydrogenation of **10** using $FeCl_3$ was conducted, only a black complex mixture containing undefined products was obtained. This is probably due to the low selectivity of the intramolecular cyclization over the intermolecular reactions.[9]

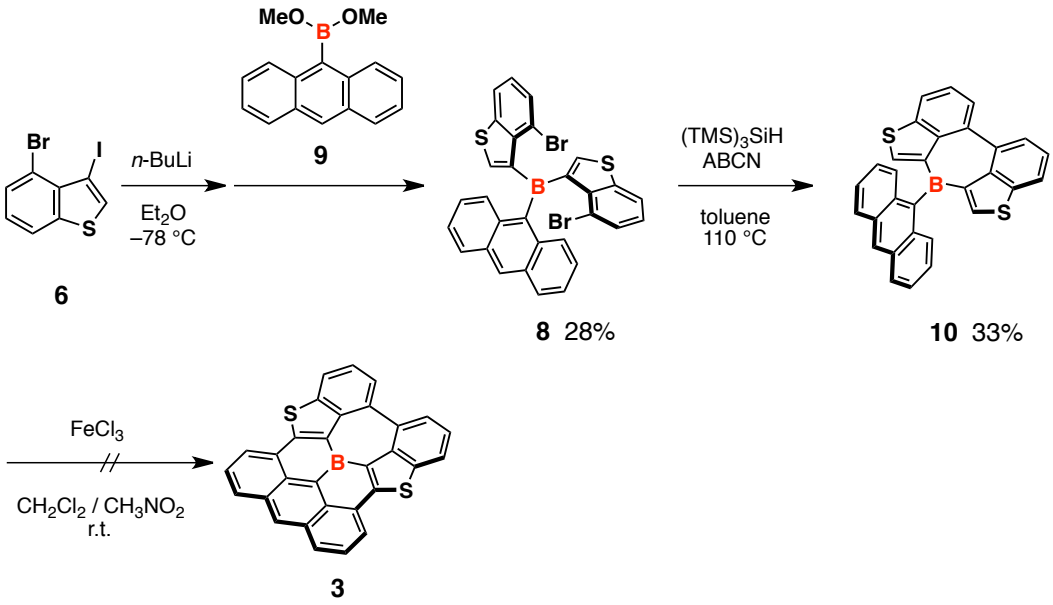

Scheme 1-3. Synthesis of completely fused triarylborane **3**. Reprinted with permission from [22]. Copyright © 2012, American Chemical Society.

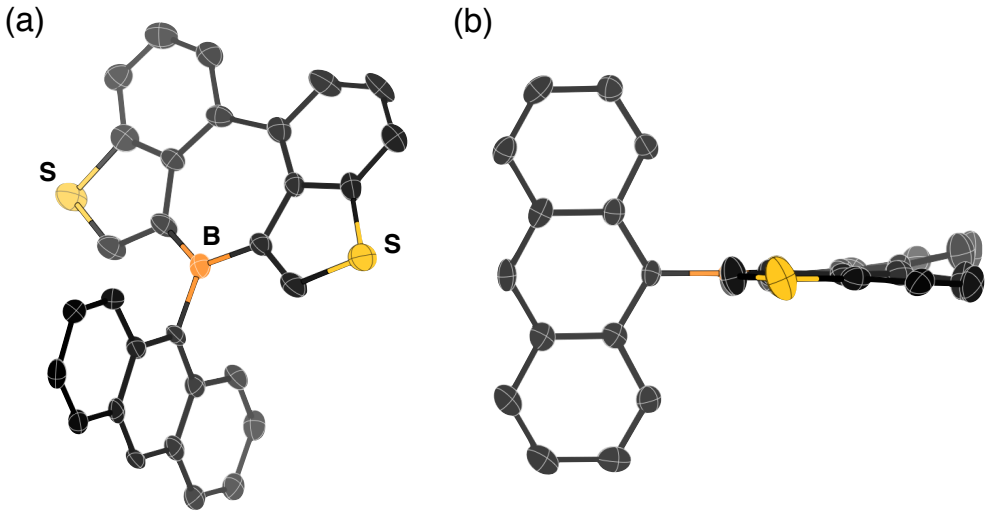

Figure 1-4. Crystal structure of **10** (50% probability of thermal ellipsoids, hydrogen atoms and solvent molecules are omitted for clarity): (a) Top view and (b) side view. Reprinted with permission from [22]. Copyright © 2012, American Chemical Society.

To solve this problem, electron-donating mesityloxy (-OMes) or octyloxy ($-OC_8H_{17}$) substituents were introduced to the 4,5-positions of the anthracene moiety, which increase the reactivity at the 1,8-positions, resulting in selective intramolecular cyclization.[10] Bulky mesityloxy groups may suppress the intermolecular interaction and enhance the solubility of the product. On the other hand, another derivative bearing the less bulky alkoxy groups were expected to construct the columnar π-stacking structure. New precursors **11** were prepared

from 4-bromo-3-iodobenzothiophene **6** and anthryldimethoxyboranes **12** in the same manner (Scheme 1-4). The reactions of **11** using $FeCl_3$ successfully produced **3** with moderate yields for the both mesityloxy and octyloxy substituents as deep purple solids. Products **3** are highly stable toward water, oxygen, and silica gel. The high stability of **3** despite the absence of steric protection is attribute to the effect of the structural constraint. Moreover, thermogravimetric analysis (TGA) displayed the high thermal stability of **3**. Their 5% weight loss temperatures were 424 °C and 372 °C for **3a** and **3b**, respectively. Compound **3a** bearing the bulky mesityloxy groups showed good solubility in common organic solvent such as chloroform and THF. In contrast, **3b** groups showed too poor solubility to be purified by standard solution-based procedure.

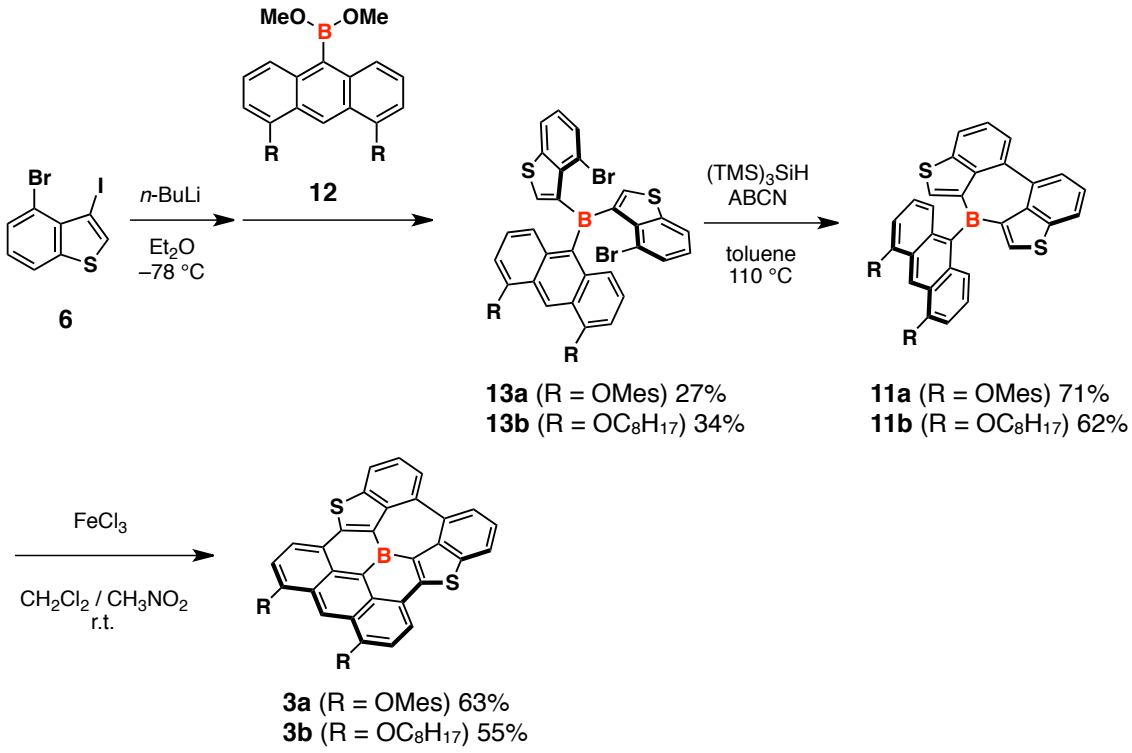

Scheme 1-4. Improved synthesis of completely fused triarylborane **3**. Reprinted with permission from [22]. Copyright © 2012, American Chemical Society.

X-ray crystallographic analysis

Single crystal X-ray diffraction analysis was conducted for compound **3a** (Figure 1-5). The result confirmed that the tricoordinate boron atom was embedded in the center of the 10-ring-fused π-skeleton containing a borepin-like[3d,e] seven-membered ring. The high planarity was confirmed by the small mean plane deviation of 0.15 Å as well as the small dihedral angles between the anthracene and benzothiophene planes (1.5° and 4.0°) and that between the two benzothiophene moieties (4.4°). The central boron atom showed trigonal

planar geometry with the sum of the three C–B–C bond angles of 360.0°. The B–C1, B–C2, and B–C3 bond lengths were 1.508(2) Å, 1.513(2) Å, and 1.539(2) Å, respectively. These values were much shorter than those of triphenylborane (1.57–1.59 Å)[11] and trimesitylborane (1.57–1.59 Å),[12] and comparable to those of the sp^3-carbon-bridged planarized triphenylborane **1** (1.52 Å).[5a] This result suggested that boron atom embedded in the π-skeleton was squeezed because of the longer B–C bond length compared to the C–C bond length. Such stress should decrease by bonding interactions between the peripheral π-orbitals and a vacant p orbital of boron atom. Indeed, the ^{11}B NMR signal for **3a** appeared at 39.5 ppm, which was upfield compared to those for precursors **11a** and **13a** (56.3 ppm and 61.5 ppm, respectively), indicating the increased electron density on the boron atom. In the crystal packing, **3a** formed face-to-face π-stacked dimers with a mean place distance of 3.53 Å (Figure 1-6). This is an unprecedented structure for an air-stable triarylborane-based π-system. The bulky Mes groups are arranged almost perpendicular to the π-skeleton, which is relevant to the high solubility of **3a**. Moreover, octanes, which were used for crystallization, are located above and below the π-stacked dimer. Unfortunately, single crystals of **3b** suitable for X-ray diffraction analysis were not obtained.

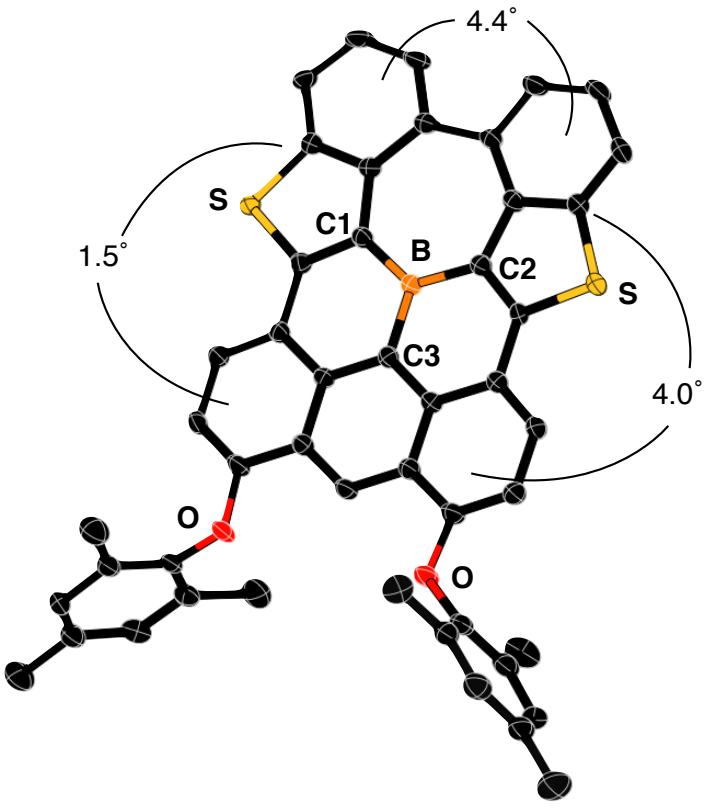

Figure 1-5. Crystal structure of **3a** (50% probability of thermal ellipsoids, hydrogen atoms and solvent molecules are omitted for clarity). Reprinted with permission from [22]. Copyright © 2012, American Chemical Society.

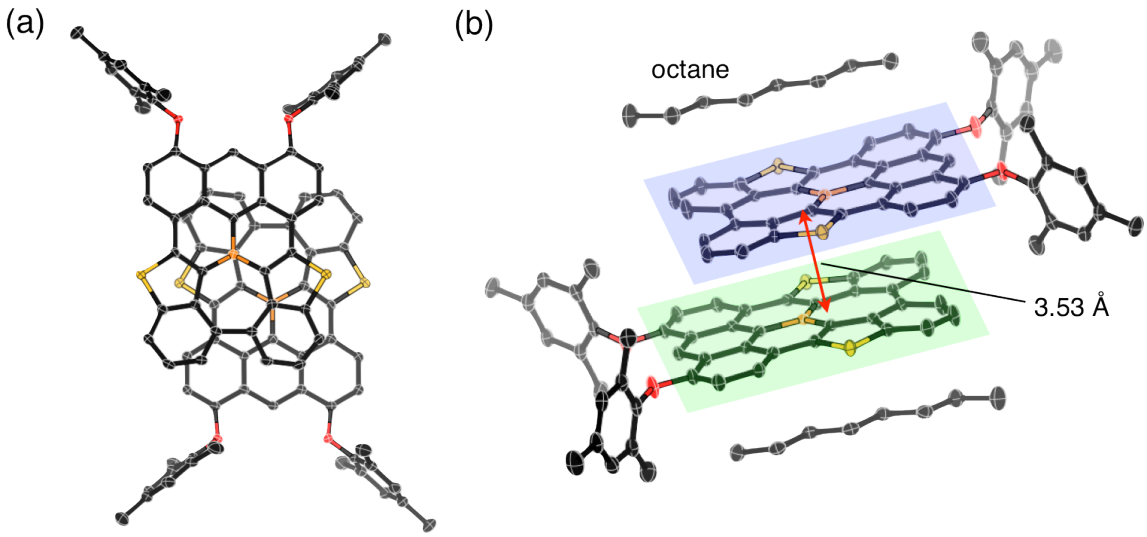

Figure 1-6. π-stacked dimer of **3a** in the crystal packing: (a) Top view and (b) side view. Reprinted with permission from [22]. Copyright © 2012, American Chemical Society.

Photophysical properties

The fully conjugated triarylborane **3** showed interesting photophysical properties (Figure 1-7). In UV-Vis absorption spectroscopy, the THF solutions of **3a** and **3b** exhibited a purple color and showed broad absorption bands that covered the entire visible region with the longest absorption wavelengths of 668 nm and 650 nm for **3a** and **3b**, respectively. Replacement of mesityloxy groups into octyloxy groups resulted in shortening of absorption wavelengths. These absorption maxima are significantly longer than that of **1** (320 nm), demonstrating the impact of the peripheral expansion of π-conjugation. Moreover, these compound showed fluorescence in the Vis-near-IR region with maximum wavelengths of 733 nm and 709 nm for **3a** and **3b**, respectively. Fluorescence wavelength was also shortened by the replacement of mesityloxy groups into octyloxy groups. Since most triarylboranes show only fluorescence in the visible region,[13] this Vis-near-IR fluorescence is a unique property for the present boron-containing π-system, even though the fluorescence quantum yield of **3a** was low (0.016). These absorption and emission bands showed negligible or only subtle solvent polarity effects (Figure 1-8 and Table 1-1), indicating the small contribution of intramolecular charge transfer character.

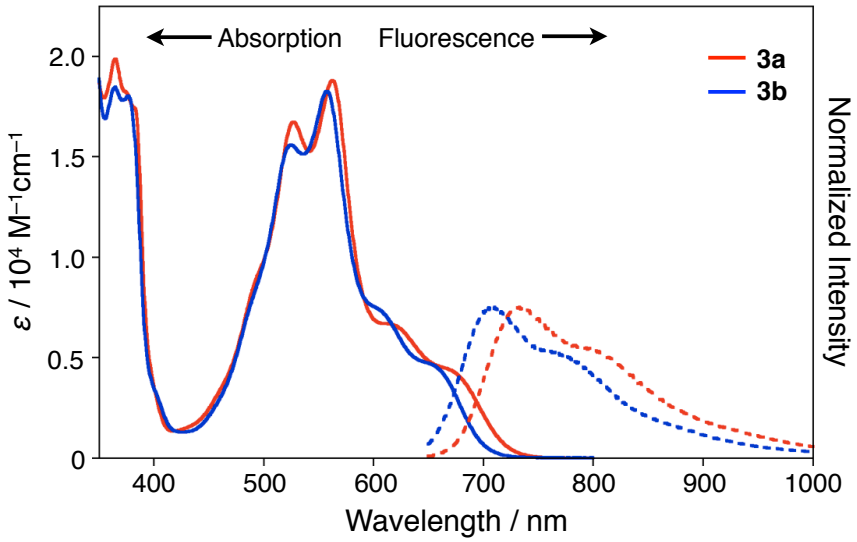

Figure 1-7. Absorption (solid line) and fluorescence spectra (dashed line) of **3a** (red) and **3b** (blue) in THF. Reprinted with permission from [22]. Copyright © 2012, American Chemical Society.

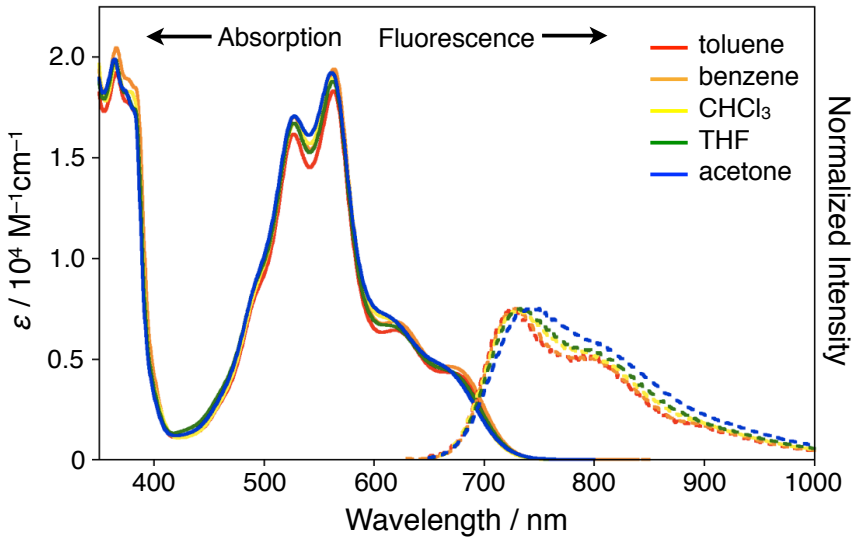

Figure 1-8. Absorption (solid line) and fluorescence spectra (dashed line) of **3a** in various solvents. Reprinted with permission from [22]. Copyright © 2012, American Chemical Society.

Table 1-1. The Maximum Wavelengths of Absorption and Fluorescence of **3a** in Various Solvents

solvent	toluene	benzene	$CHCl_3$	THF	acetone
λ_{abs} / nm	563	564	563	563	562
λ_{em} / nm	729	729	730	733	744

Electrochemical property

Cyclic voltammetry of **3a** was conducted in THF using *n*-Bu_4NPF_6 as supporting electrolyte in order to investigate the electrochemical properties (Figure 1-9). Compound **3a** showed reversible redox waves both for oxidation and reduction processes, demonstrating that the generated radical cation and radical anion are stable under the measurement conditions. The first half-reduction and oxidation potentials ($E_{1/2}$) were –1.37 V and 0.60 V (vs Fc/Fc^+), respectively. Its reduction potential was significantly positive value than that of sp^3-carbon-bridged planarized triarylborane **1** (–2.59 V vs Fc/Fc^+),[5a] indicating the higher electron-accepting ability of **3a**.

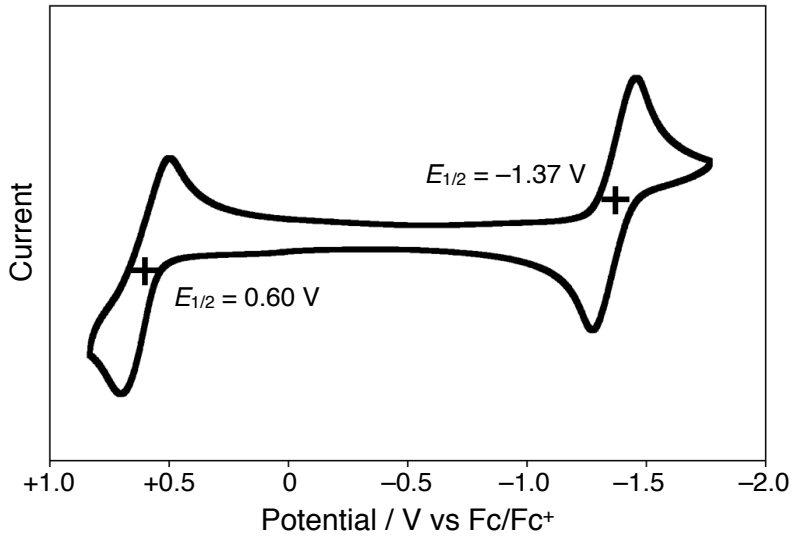

Figure 1-9. Cyclic voltammogram of **3a** in THF (1 mM), measured with *n*-Bu_4NPF_6 as supporting electrolyte at a scan rate of 100 mV s^{-1}. Reprinted with permission from [22]. Copyright © 2012, American Chemical Society.

Theoretical calculations

To elucidate the electronic structures, DFT (B3LYP/6-31G*) calculation was conducted for **3a**. The obtained optimized structure displayed good agreement with crystal

structure, including the short B–C bond lengths (Figure 1-10). The B'–C1', B'–C2', and B'–C3' bond lengths were 1.519 Å, 1.519 Å, and 1.539 Å, respectively. This skeleton has both a rather high-lying HOMO and a low-lying LUMO. The HOMO is mainly delocalized over "oxyphenylbenzothiophene dimer" moiety, while the HOMO–1 is delocalized over the entire π-skeleton with a contribution from the p orbital of the boron atom. Similar bonding interactions between the peripheral π-orbitals and the p-orbital of boron atom were observed for HOMO–3 and HOMO–6. These orbital interactions are probably relevant to the short B–C bond lengths. On the other hand, the LUMO is mostly localized on the borylanthracene moiety with a contribution from the p-π^* interaction. The LUMO level of **3a** (–2.56 eV) is much lower than that of **1** (–1.56 eV),[5a] which is consistent with the CV measurement.

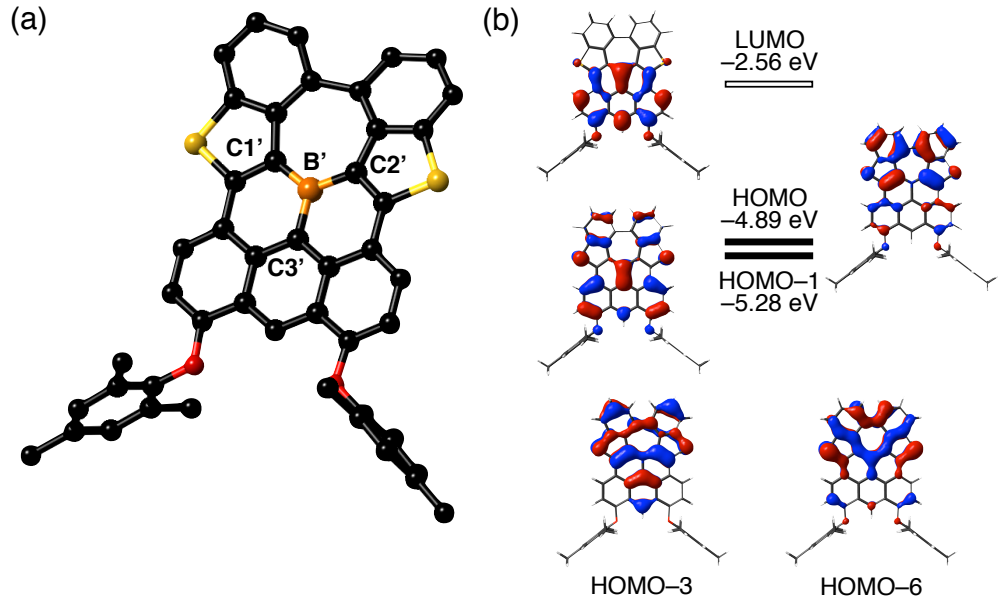

Figure 1-10. (a) The optimized structure of **3a** and (b) Kohn-Sham molecular orbitals of **3a** at the B3LYP/6-31G* level of theory. Reprinted with permission from [22]. Copyright © 2012, American Chemical Society.

DFT calculation of **3c** (R = OMe) was also conducted at the same level of theory as the model compound of **3b** for comparison with **3a** (Figure 1-11). Higher electron-donating character of alkoxy groups compared to mesityloxy groups slightly increased both HOMO and LUMO levels. The HOMO–LUMO gap of **3c** (2.36 eV) was slightly larger than that of **3a** (2.33 eV). The TD-DFT calculations at the same level of theory suggested that the broad visible absorption bands consist of two transitions for both **3a** and **3b**, which are assignable to the HOMO→LUMO and the HOMO–1→LUMO transitions. Their calculated energies are 1.86 eV (666 nm) and 2.38 eV (522 nm) for **3a**, while 1.90 eV (653 nm) and 2.41 eV (513 nm) for **3c**, respectively. The energy differences between **3a** and **3c** were consistent with the

experimental absorption spectra of **3a** and **3b**. These calculations demonstrated that the key factor for realizing absorption and emission at long wavelengths is to incorporate the electron-accepting tricoordinate boron atom into the highly electron-donating polycyclic π-skeleton.

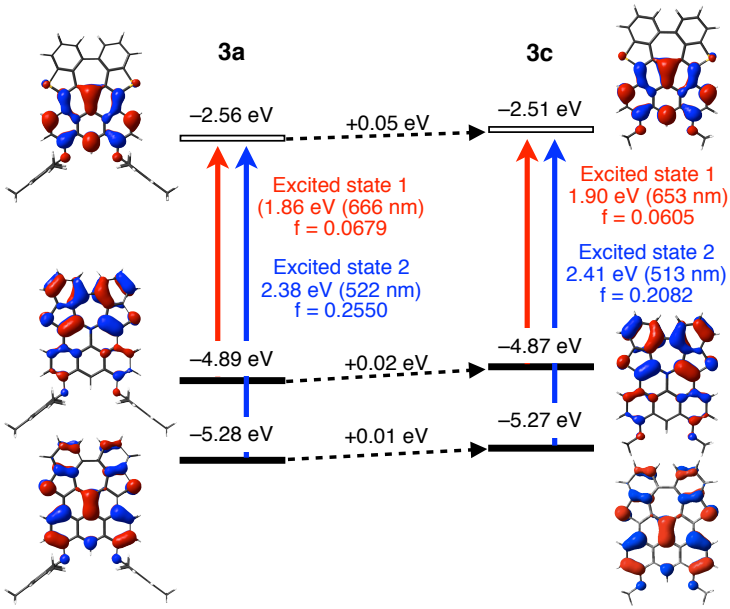

Figure 1-11. Kohn-Sham molecular orbitals and electronic transitions of **3a** and **3c** at the B3LYP/6-31G* level of theory. Reprinted with permission from [22]. Copyright © 2012, American Chemical Society.

Lewis acidity

The most important structural feature of **3** is that the tricoordinate boron atom is surrounded by a rigid and planar π-skeleton. A basic interest in this system is whether this boron atom still maintains Lewis acidity and forms a Lewis acid–base adduct. More importantly, the formation of Lewis acid–base adducts with **3** can be regarded as a model for chemical adsorption processes on the boron-doped graphene. The potential of boron-doped graphene for chemisorption has recently generated increasing attention, as this aspect may be beneficial for various applications including chemical sensing, hydrogen storage, and surface-enhanced Raman scattering.[14] Although several theoretical studies have addressed this issue, experimental insight still remains to be gathered. Therefore, the author evaluated the Lewis acidity of **3** in order to gain a quantitative understanding of the chemisorption properties of the boron atom embedded into π-skeleton. To study this issue, **3a** was treated with several Lewis bases (Scheme 1-5).[15]

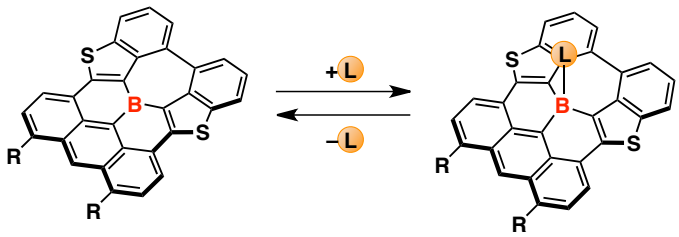

Scheme 1-5. Interconversion between **3** and the corresponding Lewis acid–base adduct by coordination with a Lewis base. Reprinted with permission from [22]. Copyright © 2012, American Chemical Society.

Upon the addition of *n*-Bu_4NF to a THF solution of **3a**, the color of the solution dramatically changed from purple to yellow (Figure 1-12). In line with this change, the ^{11}B NMR signal of **3a** was shifted from a broad peak at 39.5 ppm to a sharp one at 1.6 ppm in $CDCl_3$ by the addition of an excess amount of *n*-Bu_4NF, indicating the formation of tetracoordinate fluoroborate species.[16]

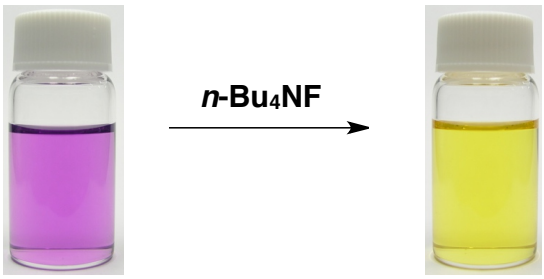

Figure 1-12. Color change of a THF solution of **3a** upon addition of *n*-Bu_4NF. Reprinted with permission from [22]. Copyright © 2012, American Chemical Society.

The UV-Vis absorption spectra showed that as the amount of the Lewis base increased, the absorption bands of **3a** around 670 and 560 nm disappeared and a new band at 478 nm appeared (Figure 1-13a), which is assignable to a tetracoordinate fluoroborate **3a**·F^-. The binding constant (*K*) of **3a** toward a fluoride ion in THF was determined by titration experiments[15a] monitoring the UV-Vis absorption spectra to be 1.3 (± 0.3) × 10^5 M^{-1} (Figure 1-13b), which is slightly smaller than those of **1** (7.0 × 10^5 M^{-1})[5a] and trimesitylborane (3.3 × 10^5 M^{-1}).[15a] This comparison demonstrates that **3a** keeps its Lewis acidity, although the degree is slightly diminished by the structural restriction. UV-Vis titration toward *n*-Bu_4NCN was also conducted using a THF solution of **3a** (Figure 1-14a). The binding constant (*K*) toward a cyanide ion in THF was calculated to be 2.5 (± 0.8) × 10^5 M^{-1} (Figure 1-14b), which is lower than that of **1** (2.5 × 10^6 M^{-1}).[5a] Compound **3a** did not show the selective affinity toward anionic strong Lewis bases.

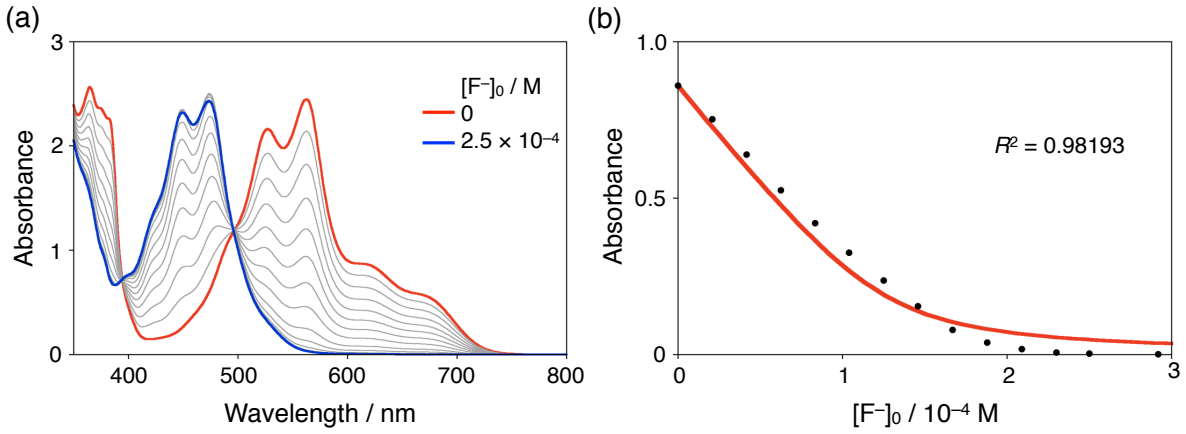

Figure 1-13. (a) UV-Vis absorption spectral change upon addition of *n*-Bu_4NF to a THF solution of **3a** (1.2×10^{-4} M) and (b) UV-Vis absorption titration plot of the absorbance at 620 nm (black dots) and the fitting curve for the binding constant of **3a** toward F^- (red line). Reprinted with permission from [22]. Copyright © 2012, American Chemical Society.

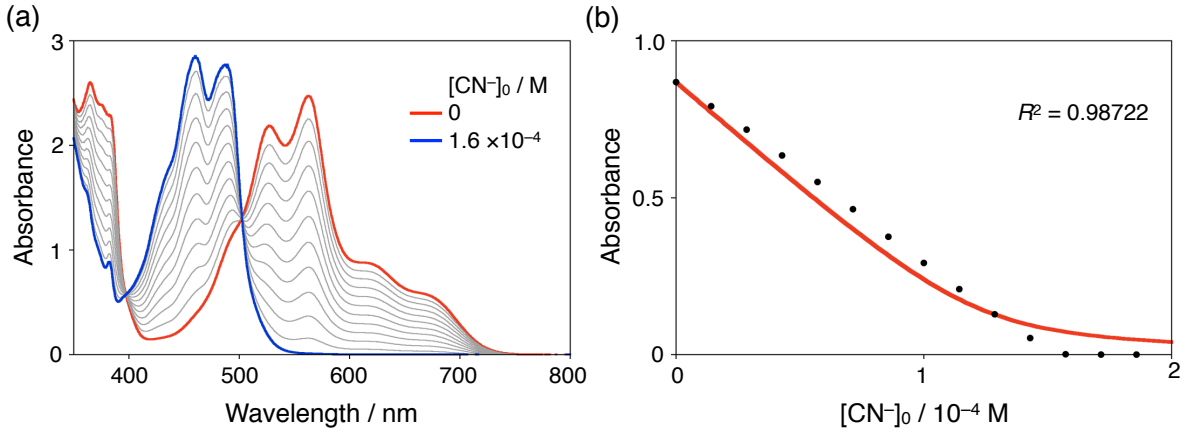

Figure 1-14. (a) UV-Vis absorption spectral change upon addition of *n*-Bu_4NCN to a THF solution of **3a** (1.3×10^{-4} M) and (b) UV-Vis absorption titration plot of the absorbance at 620 nm (black dots) and the fitting curve for the binding constant of **3a** toward CN^- (red line). Reprinted with permission from [22]. Copyright © 2012, American Chemical Society.

In addition, **3a** showed the fluorescence spectral change upon the addition of Lewis bases (figure 1-15). After the addition of the *n*-Bu_4NF or *n*-Bu_4NCN, the Vis-near-IR fluorescence of **3a** disappeared and a new visible fluorescence appeared at 599 and 576 nm for **3a·F⁻** and **3a·CN⁻**, respectively.

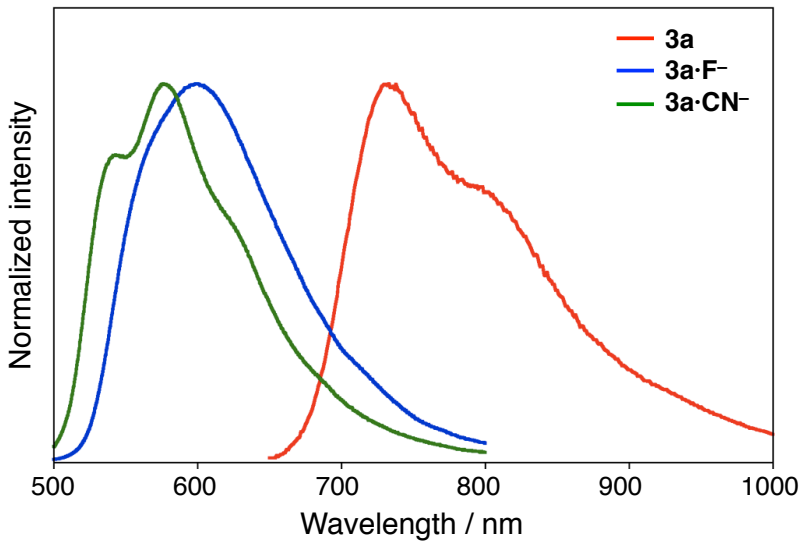

Figure 1-15. Fluorescence spectra of a THF solution of **3a** (red), **3a·F⁻** (blue) and **3a·CN⁻** (green). Reprinted with permission from [22]. Copyright © 2012, American Chemical Society.

The structure of tetracoordinate **3a·F⁻** was confirmed by X-ray crystallography as a K^+([2.2.2]cryptand) salt (Figure 1-16). In the crystal structure, two crystallographically independent molecules were observed, one of which showed a disorder in the core π-skeleton. Thus, the structural features of **3a·F⁻** are discussed for the other, non-disordered molecule. The polycyclic π-skeleton still had high planarity, and only the central boron atom deviates from the π-plane. The dihedral angles between the anthracene and benzothiophene moieties were 3.0° and 14.4°, and that between the two benzothiophene moieties was 16.3°. The B"–C1", B"–C2", and B"–C3" bond lengths were 1.596(9) Å, 1.584(8) Å, and 1.579(9) Å, respectively. These values were longer than those of **3a** but still shorter than those of typical fluoroborates (1.62–1.68 Å).[17] This result suggested that the structural constraint restrains the deformation of the boron atom to the tetracoordinate geometry.

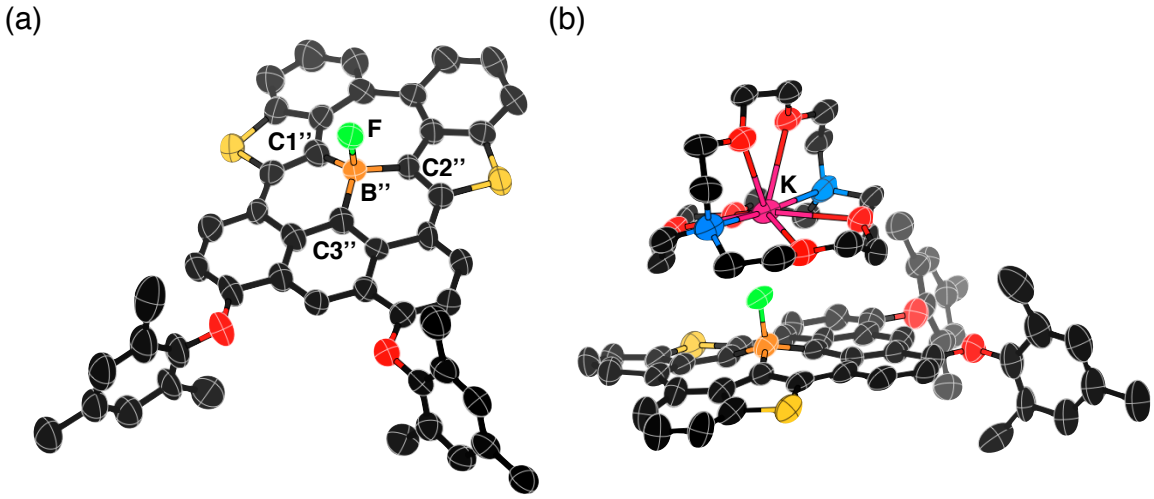

Figure 1-16. Crystal structure of **[K([2.2.2]cryptand)]$^{+}$·3aF^{-}** (50% probability of thermal ellipsoids, hydrogen atoms and solvent molecules are omitted for clarity): (a) Top view, in which [K([2.2.2]cryptand)]$^{+}$ was omitted for clarity, and (b) side view. Reprinted with permission from [22]. Copyright © 2012, American Chemical Society.

As the Lewis acidity of **3** was confirmed, the author tested the formation of Lewis acid–base adduct with a weaker neutral base, pyridine. UV-Vis absorption titration toward pyridine using a THF solution of **3a** displayed only small spectral changes upon the addition of excess amount of pyridine (Figure 1-17a). The binding constant toward pyridine in THF was determined to be 0.353 (± 0.002) M^{-1} at 23 °C (Figure 1-17b), which was much lower than those toward anionic Lewis bases. It is noteworthy that **1**, which showed slightly higher binding constant toward fluoride ion than **3a**, did not form the Lewis acid–base adduct with amine, such as DBU and DABCO.[5a] Therefore, **3a** was stronger Lewis acid toward neutral Lewis bases than **1**. This difference is probably due to the much higher electron-accepting ability of **3a** despite its more rigid structure. More importantly, this result suggested the chemisorption ability of the boron-doped graphene for amine binding.

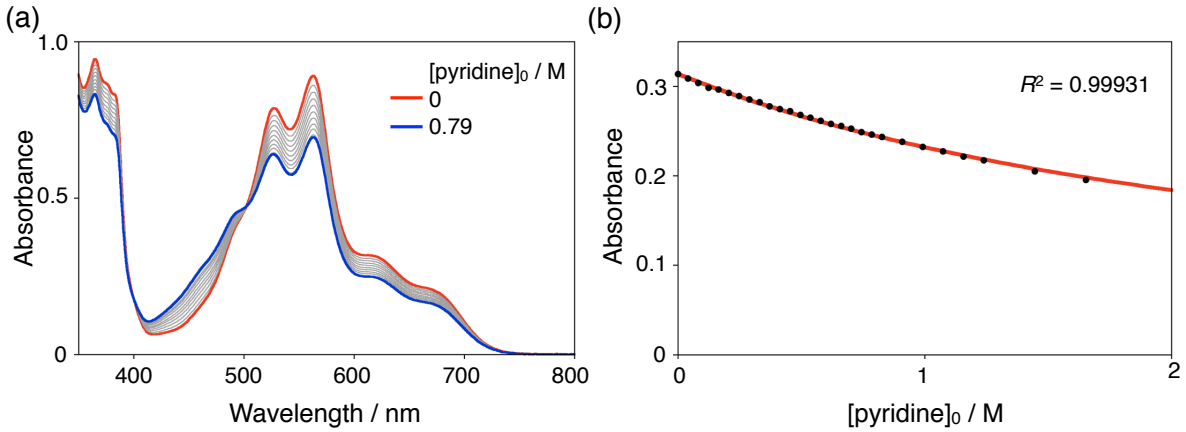

Figure 1-17. (a) UV-Vis absorption spectral change upon addition of pyridine to a THF solution of **3a** (4.9×10^{-5} M) and (b) UV-Vis absorption titration plot of the absorbance at 620 nm (black dots) and the fitting curve for the binding constant of **3a** toward pyridine (red line). Reprinted with permission from [22]. Copyright © 2012, American Chemical Society.

Although the binding constant of **3a** toward pyridine was small, it significantly depends on the temperature, resulting in an interesting thermochromism. The color of a pyridine/THF (1:3) solution of **3a** changed dramatically from purple at a higher temperature to yellow at a lower temperature (Figure 1-18). Variable-temperature UV-Vis absorption spectra displayed that as the temperature decreased from 60 to –80 °C, the absorbance at 563 nm and 668 nm decreased and those at 485 nm and 461 nm increased with isosbestic points at 508 nm and 397 nm (Figure 1-19). This thermochromic behavior is based on the temperature dependence of the binding constant, which caused the change in the ratio of tricoordinate species **3a** to tetracoordinate speceies **3a**·pyridine. Thermodynamic parameters for the equilibrium between **3a** and **3a**·pyridine were estimated to be ΔH = –21.3 kJ mol^{-1} and ΔS = –76.2 J K^{-1} mol^{-1} by using the van't Hoff plot (ln$K$ vs. 1/T) and ΔG–T plot (Figure 1-20).

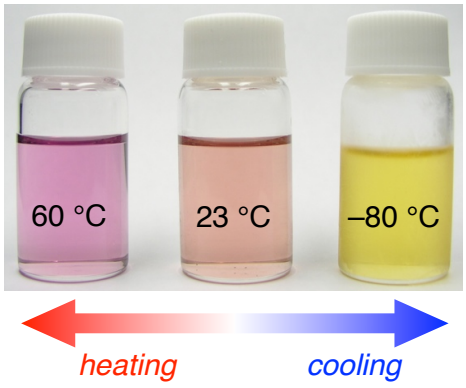

Figure 1-18. (a) Thermochromism of 1:3 pyridine/THF solution of **3a**. Reprinted with permission from [22]. Copyright © 2012, American Chemical Society.

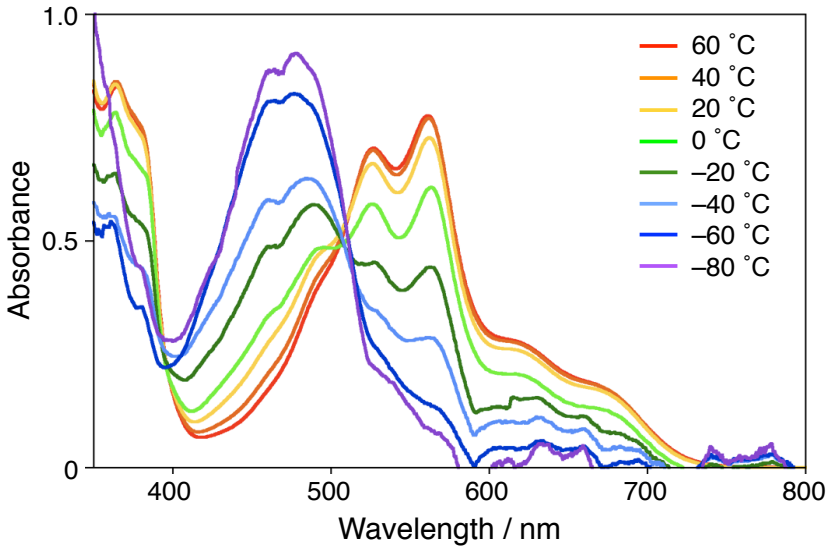

Figure 1-19. Variable-temperature UV-Vis absorption spectra of a 1:15 pyridine/THF solution of **3a** (4.7×10^{-5} M). Reprinted with permission from [22]. Copyright © 2012, American Chemical Society.

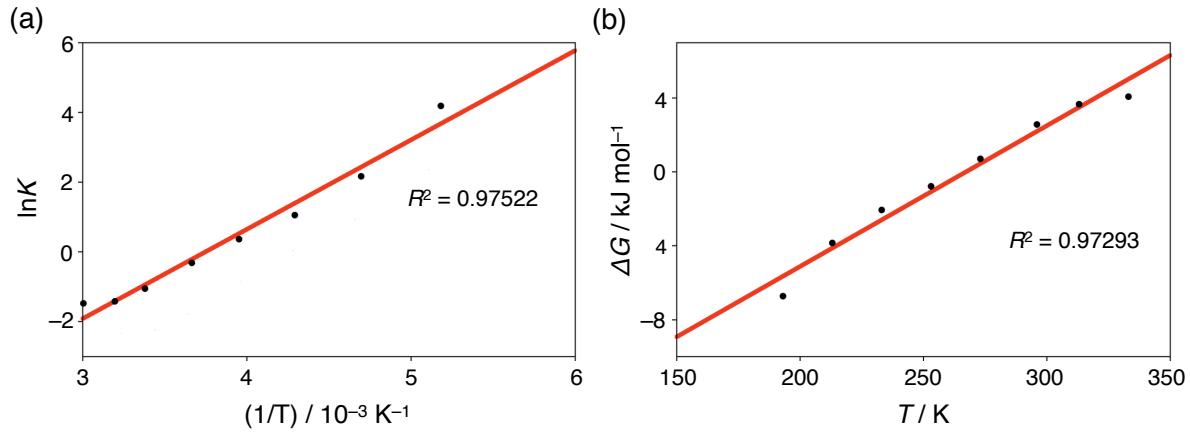

Figure 1-20. (a) The van't Hoff plot (black dots) and the fitting line for the *ΔH* (red line) and (b) the *ΔG*–T plot (black dots) and the fitting line for the *ΔS* (red line) in the equilibrium between **3a** and **3a**·pyridine. Reprinted with permission from [22]. Copyright © 2012, American Chemical Society.

1-3. Conclusion

The author has succeeded in the development of a new planarized triarylborane, in which tricoordinate boron atom is embedded in the electron-donating polycyclic π-skeleton. The compound shows remarkable chemical and thermal stabilities and it can be handled without special care. Unlike the previous sp^3-carbon-bridged planar triphenylborane, the highly planar structure with less steric hinderance around π-skeleton forms a face-to-face π-stacked structure. The narrower HOMO–LUMO gap also reflects its distinct electronic feature from other triarylboranes. In light of these unique characteristics, this expanded borane should have significant potential for optoelectronic applications. The interconversion between the tricoordinate borane and the tetracoordinate Lewis acid–base adduct is the other fascinating feature of this boron-embedded π-system. Since their absorption properties are largely different and the abundance ratio in the equilibrium depends on the temperature, its solution displays thermochromic behavior in the presence of pyridine.

1-4. Experimental section

General

Melting points (mp) were determined with a Yanaco MP-S3 instrument. ^{1}H, ^{13}C, and ^{11}B NMR spectra were measured with a JEOL A-400 or AL-400 (400 MHz for ^{1}H, 100 MHz for ^{13}C, and 128 MHz for ^{11}B) spectrometer. Chemical shifts are reported in δ ppm with reference to residual protons and carbons of $CDCl_3$ (7.26 ppm in ^{1}H NMR and 77.16 ppm in ^{13}C NMR), $(CD_3)_2SO$ (2.50 ppm in ^{1}H NMR and 39.52 ppm in ^{13}C NMR), and chlorobenzene-d_5 (7.14 ppm in ^{1}H NMR). The external standard of $BF_3{\cdot}OEt_2$ was used in ^{11}B NMR spectra. Mass spectra were measured with a Bruker micrOTOF Focus. Single crystal X-ray diffraction measurements were performed with a Rigaku X-ray diffractometer equipped with a molybdenum MicroMax-007 microfocus generator, VariMax-Mo optics, and a Saturn 70 CCD detector. The structures were solved by the direct method (SHELXL-97[18]) and refined by the full-matrix least-squares on F^2 (SHELXL-97[18]). All non-hydrogen atoms were refined anisotropically. Thin layer chromatography (TLC) was performed on the plates coated with 0.25 mm thickness of Silica Gel 60 F-254 (Merck). Column chromatography was performed using neutral silica gel PSQ 60B (Fuji Silysia Chemical). Recycling preparative high performance liquid chromatography (HPLC) was performed using LC-918 (Japan Analytical Industry) equipped with silica gel columns (Wakopak® Wakosil-II 5SIL Prep, Wako). Thermogravimetric analysis (TGA) was performed using Seiko TGA 6200 at a heating rate of 5 °C min^{-1} under a nitrogen atmosphere. UV-Vis absorption spectra were measured with a Shimadzu UV-3150 and a Shimadzu UV-2550 spectrometer, while fluorescence spectra were measured with a Hitachi F-4500 spectrometer and a Horiba Fluorolog spectrometer. Absolute fluorescence quantum yields (Φ) were determined with a Hamamatsu C9920-02 calibrated integrating sphere. Cyclic voltammetry (CV) was performed on an Als/chi-617A electrochemical analyzer. The CV cell consisted of a glassy carbon electrode, a Pt wire counter electrode, and a $Ag/AgNO_3$ reference electrode. The measurement was carried out with a scan rate of 100 mV s^{-1} under an argon atmosphere using a THF solution of sample with a concentration of 1 mM. Tetrabutylammonium hexafluorophosphate (n-Bu_4NPF_6) was used as a supporting electrolyte. The redox potentials were calibrated with ferrocene as an internal standard. All reactions were performed under a nitrogen atmosphere, unless stated otherwise. Commercially available solvents and reagents were used without further purification unless otherwise mentioned. Dry ether, toluene, THF, and CH_2Cl_2 were purchased from Kanto Chemical. n-BuLi (1.6 M in hexane) was purchased from Wako Pure Chemical Industries and used as received. $BF_3{\cdot}OEt_2$ was distilled in the presence of CaH_2 before use. n-Bu_3SnH was purchased from Aldrich. $(TMS)_3SiH$ (stabilized with TBBP) was

purchased from Tokyo Chemical Industry. 1,3-Dibromo-2-(trimethylsilylethynyl)benzene **14**,[19] 9-anthryldimethoxyborane **9**,[20] 4,5-bis(2,4,6-trimethylphenoxy)-9-bromoanthracene **18a**,[10] 9-bromo-4,5-dioctyloxyanthracene **18b**[10] were prepared according to the literatures.

Synthesis

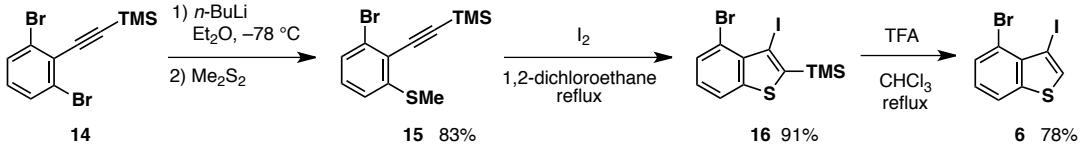

14 **15** 83% **16** 91% **6** 78%

1-Bromo-3-(methylthio)-2-(trimethylsilylethynyl)benzene (15). To a solution of **14** (37.5 g, 113 mmol) in dry ether (226 mL) cooled at –78 °C was added *n*-BuLi (1.64 M in hexane, 68.9 mL, 113 mmol) dropwise. After the reaction mixture was stirred at the same temperature for 1 h, dimethyldisulfide (10.3 mL, 113 mmol) was added dropwise. The reaction mixture was gradually warmed to room temperature. After addition of water, the resulting aqueous layer was extracted with ether. The combined organic layer was washed with aqueous $NaHCO_3$ and brine, dried over anhydrous Na_2SO_4, and concentrated under reduced pressure. The resulting mixture was subjected to a silica gel column chromatography (PSQ 60B, 20/1 hexane/ethyl acetate, R_f = 0.50) to afford 28.0 g (93.6 mmol, 83% yield) of **15** as a yellow solid. mp: 38–39 °C. ^{1}H NMR (400 MHz, $CDCl_3$) δ 0.31 (s, 9H), 2.46 (s, 3H), 7.04 (d, J = 8.0 Hz, 1H), 7.10 (t, J = 8.0 Hz, 1H), 7.33 (d, J = 8.0 Hz, 1H). ^{13}C NMR (100 MHz, $CDCl_3$): δ 0.0, 15.5, 100.4, 107.5, 122.3, 122.5, 126.6, 128.1, 129.3, 144.8. HRMS (APCI, positive): calcd for $C_{12}H_{15}BrSSi$: 297.9842 (M^+), found 297.9839.

4-Bromo-3-iodo-2-(trimethylsilyl)benzo[*b*]thiophene (16). To a solution of **15** (27.7 g, 92.5 mmol) in 1,2-dichloroethane (620 mL) was added iodine (33.0 g, 130 mmol). The mixture was refluxed for 17 h. The reaction mixture was allowed to cool down to room temperature and quenched with saturated aqueous Na_2SO_3. The aqueous layer was extracted with $CHCl_3$. The combined organic layer was washed with brine, dried over anhydrous Na_2SO_4, and concentrated under reduced pressure. The resulting mixture was subjected to a silica gel column chromatography (PSQ 60B, hexane, R_f = 0.65) to afford 34.7 g (84.4 mmol, 91% yield) of **16** as a yellow solid. mp: 78–79 °C. ^{1}H NMR (400 MHz, $CDCl_3$): δ 0.53 (s, 9H), 7.14 (t, J = 7.8 Hz, 1H), 7.63 (d, J = 7.8 Hz, 1H), 7.87 (d, J = 7.8 Hz, 1H). ^{13}C NMR (100 MHz, $CDCl_3$): δ –0.4, 82.4, 117.8, 122.1, 125.3, 131.5, 136.2, 143.4, 145.3. HRMS (APCI, positive): calcd for $C_{11}H_{12}BrISSi$: 409.8652 (M^+), found 409.8662.

4-Bromo-3-iodobenzo[*b*]thiophene (6). To a solution of **16** (34.6 g, 84.1 mmol) in $CHCl_3$ (420 mL) was added trifluoroacetic acid (TFA) (30 mL, 410 mmol) in the air. After the mixture was refluxed for 2 h, TFA (30 mL, 410 mmol) was added again. The mixture was refluxed for 1 h, then TFA (20 mL, 205 mmol) was added again and the mixture was refluxed for 2 h. The reaction mixture was allowed to cool down to room temperature, and neutralized with a saturated aqueous solution of $NaHCO_3$. The resulting aqueous layer was extracted with $CHCl_3$. The combined organic layer was washed with water and brine, dried over anhydrous Na_2SO_4, and concentrated under reduced pressure. The resulting mixture was recrystallized from a hot hexane/ethyl acetate solution to afford 22.1 g (65.2 mmol, 78% yield) of **6** as a colorless solid. mp: 133–134 °C. ^{1}H NMR (400 MHz, $CDCl_3$): δ 7.19 (t, J = 7.6 Hz, 1H), 7.64 (d, J = 7.6 Hz, 1H), 7.79 (s, 1H), 7.89 (d, J = 7.6 Hz, 1H). ^{13}C NMR (100 MHz, $CDCl_3$): δ 73.9, 118.1, 122.7, 125.7, 131.1, 133.6, 134.1, 140.2. HRMS (APCI, positive): calcd for C_8H_4BrIS: 337.8256 (M^+), found 337.8253.

Tris(4-bromobenzothiophen-3-yl)borane (5) . To a solution of **6** (4.07 g, 12.0 mmol) in dry ether (240 mL) cooled at –78 °C was added *n*-BuLi (1.64 M, 7.30 mL, 12.0 mmol) dropwise. After the reaction mixture was stirred at the same temperature for 45 min, $BF_3{\cdot}OEt_2$ (495 mL, 4.01 mmol) was added. The reaction mixture was gradually warmed to room temperature and filtered in the air. The filtrate was concentrated under reduced pressure. The resulting mixture was passed through a short silica gel column (toluene), then recrystallized from CH_2Cl_2/hexane by slow evaporation to afford 1.65 g (2.55 mmol, 64% yield) of **5** as a pale yellow solid. mp: 296–297 °C. ^{1}H NMR (400 MHz, $(CD_3)_2SO$, 35 °C): δ 7.23 (broad s, 3H), 7.31 (broad t, J = 7.2 Hz, 3H), 7.57 (broad d, J = 6.4 Hz, 3H), 8.11 (d, J = 8.0 Hz, 3H). ^{13}C NMR (100 MHz, $CDCl_3$): δ 119.8, 121.8, 125.7, 129.8, 136.9, 141.5, 143.6. One signals for the carbon atoms bonding to the boron atom were not observed due to the quadrupolar relaxation of the boron atom. ^{11}B NMR (128 MHz, $CDCl_3$): δ 55.3. HRMS (APCI, positive): calcd for $C_{24}H_{12}BBr_3S_3$: 643.7739 (M^+), found 643.7747.

A partly ring-fused tris(benzothiophen-3-yl)borane (7). A solution of *n*-Bu_3SnH (0.30 mL, 1.1 mmol) and 2,2′-azobis(isobutyronitrile) (AIBN, 45 mg, 0.274 mmol) in dry toluene (15 mL) was added dropwise by a syringe pump over 1 h to a stirred solution of **5** (201 mg, 0.310 mmol) in dry toluene (16 mL) at 120 °C. Stirring was continued at the same temperature for 14 h. The mixture was concentrated under reduced pressure, washed with hexane, and reprecipitated from CH_2Cl_2/hexane. The precipitate was subjected to a silica gel column chromatography (PSQ 60B, 3/1 hexane/CH_2Cl_2, R_f = 0.50) to afford 9 mg (0.022 mmol, 7%

yield) of **7** as an orange solid. mp: 243–244 °C. ^{1}H NMR (400 MHz, $CDCl_3$): δ 7.47 (t, J = 8.0 Hz, 1H), 7.48 (t, J = 8.0 Hz, 1H), 7.59 (t, J = 8.0 Hz, 1H), 7.88 (d, J = 8.0 Hz, 1H), 7.91 (d, J = 8.0 Hz, 1H), 7.93 (d, J = 8.0 Hz, 1H), 8.03 (d, J = 8.0 Hz, 1H), 8.05 (d, J = 8.0 Hz, 2H), 8.79 (s, 1H), 8.84 (s, 1H). ^{13}C NMR spectra was not obtained due to its poor solbility. ^{11}B NMR (128 MHz, $CDCl_3$): δ 41.9. HRMS (APCI, positive): calcd for $C_{24}H_{11}BS_3$: 406.0108 (M^+), found 406.0108.

(Anthracen-9-yl)bis(4-bromobenzothiophen-3-yl)borane (8). To a solution of **6** (427 mg, 1.26 mmol) in dry ether (30 mL) cooled at –78 °C was added *n*-BuLi (1.63 M, 0.77 mL, 1.26 mmol) dropwise. After the reaction mixture was stirred at the same temperature for 40 min, a solution of **9**[4] (150 mg, 0.60 mmol) in dry ether (10 mL) was added to the mixture dropwise. The reaction mixture was gradually warmed to room temperature and filtered in the air. The filtrate was concentrated under reduced pressure. The resulting mixture was subjected to a silica gel column chromatography (PSQ 60B, 3/1 hexane/CH_2Cl_2, R_f = 0.39) to afford 102 mg (0.167 mmol, 28% yield) of **8** as a yellow solid. mp: >152 °C (decomposed). The chemical shifts in NMR spectra are largely dependent on the temperature, because the rotational mode of the bulky anthryl group at room temperature is comparatively slow on the NMR time scale. ^{1}H NMR (400 MHz, $(CD_3)_2SO$, 120 °C): δ 7.21–7.29 (m, 4H), 7.40 (td, J = 7.6 Hz, 0.8 Hz, 2H), 7.46 (dd, J = 7.6 Hz, 0.8 Hz, 2H), 7.57 (s, 2H), 8.02–8.10 (m, 6H), 8.67 (s, 1H). ^{13}C NMR (100 MHz, $(CD_3)_2SO$, 120 °C): δ 117.4, 121.6, 124.0, 124.5, 125.2, 128.1, 128.6, 128.7, 128.8, 130.5, 133.9, 140.7, 140.9, 140.9, 143.1. Two signals for the carbon atoms bonding to the boron atom were not observed due to the quadrupolar relaxation of the boron atom. ^{11}B NMR (128 MHz, $CDCl_3$, 24 °C): δ 61.2. HRMS (APCI, positive): calcd for $C_{30}H_{18}BBr_2S_2$: 610.9304 [$(M+H)^+$], found 610.9287.

An anthrylborane precursor 10. To a solution of **8** (100 mg, 0.163 mmol) and 1,1′-azobis(cyclohexanecarbonitrile) (ABCN, 62 mg, 0.254 mmol) in dry toluene was added tris(trimethylsilyl)silane (170 mL, 0.498 mmol). The mixture was heated at 110 °C for 15 h. After removal of the solvent under reduced pressure, the mixture was dissolved into a small amount of toluene and poured into hexane. The precipitate was collected by filteration and washed with hexane to afford 24 mg of **10** (0.053 mmol, 33% yield) as a yellow solid. mp: >150 °C (decomposed). ^{1}H NMR (400 MHz, $CDCl_3$): δ 7.23 (t, J = 8.0 Hz, 2H), 7.43 (t, J = 8.0 Hz, 2H), 7.53 (t, J = 7.6 Hz, 2H), 7.69 (d, J = 8.0 Hz, 2H), 7.75 (s, 2H), 7.90 (d, J = 7.6 Hz, 2H), 8.07 (d, J = 8.0 Hz, 2H), 8.14 (d, J = 7.6 Hz, 2H), 8.51 (s, 1H). ^{13}C NMR (100 MHz, $CDCl_3$): δ 122.9, 124.7, 125.2, 125.5, 126.5, 127.3, 128.8, 130.3, 131.4, 133.7, 136.9, 141.9,

143.5, 151.3. Two signals for the carbon atoms bonding to the boron atom were not observed due to the quadrupolar relaxation of the boron atom. ^{11}B NMR (128 MHz, $CDCl_3$): δ 56.9. HRMS (APCI, positive): calcd for $C_{30}H_{17}BS_2$: 452.0859 (M^+), found 452.0865.

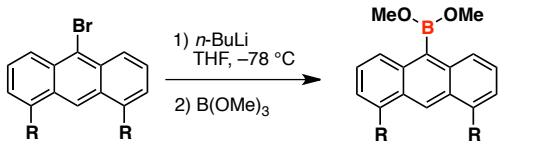

18a (R = OMes)
18b (R = OC_8H_{17})

12a (R = OMes) 89%
12b (R = OC_8H_{17})

[4,5-Bis(2,4,6-trimethylphenoxy)anthracen-9-yl]dimethoxyborane (12a). To a solution of **18a** (500 mg, 0.95 mmol) in dry THF (12 mL) cooled at –78 °C was added *n*-BuLi (1.64 M, 0.58 mL, 0.95 mmol) dropwise. After the reaction mixture was stirred at the same temperature for 30 min, trimethyl borate (130 μL, 1.2 mmol) was added. The reaction mixture was gradually warmed to room temperature. After addition of water, the resulting aqueous layer was extracted with CH_2Cl_2. The combined organic layer was washed with brine, dried over anhydrous Na_2SO_4, and concentrated under reduced pressure. The resulting mixture was suspended in methanol. After the mixture was refluxed for 5 min, the precipitate was filtered and washed with methanol to afford 440 mg (0.85 mmol, 89% yield) of **12a** as a pale yellow solid. mp: 185–186 °C. ^{1}H NMR (400 MHz, $CDCl_3$): δ 2.15 (s, 12H), 2.34 (s, 6H), 3.69 (s, 6H), 6.31 (d, J = 7.6 Hz, 2H), 6.96 (s, 4H), 7.26 (t, J = 7.6 Hz, 2H), 7.47 (d, J = 7.6 Hz, 2H), 9.81 (s, 1H). ^{13}C NMR (100 MHz, $CDCl_3$): δ 16.3, 21.0, 53.0, 104.3, 116.9, 120.9, 123.7, 126.2, 129.7, 131.2, 134.6, 135.1, 149.3, 154.6. One signal for the carbon atom bonding to the boron atom was not observed due to the quadrupolar relaxation of the boron atom. ^{11}B NMR (128 MHz, $CDCl_3$): δ 31.3. HRMS (APCI, positive): calcd for $C_{34}H_{36}BO_4$: 519.2701 [$(M+H)^+$], found 519.2710.

[4,5-Bis(2,4,6-trimethylphenoxy)anthracen-9-yl]bis(4-bromobenzothiophen-3-yl)borane (13a). Compound **13a** was prepared from **12a** as a yellow solid in 27% yield in the similar manner as described for **8**. mp: >205 °C (decomposed). The chemical shifts in NMR spectra are largely dependent on the temperature, because the rotational mode of bulky anthryl group at room temperature is comparatively slow on the NMR time scale. ^{1}H NMR (400 MHz, $CDCl_3$, 0 °C): δ 2.21 (s, 12H), 2.35 (s, 6H), 6.29, (broad d, J = 4.0 Hz, 2H), 6.98 (s, 4H), 7.16 (broad s, 2H), 7.38 (broad s, 2H), 7.74 (broad s, 2H), 7.84 (d, J = 8.0 Hz, 2H), 7.99 (broad s, 2H), 9.96 (s, 1H). ^{13}C NMR (100 MHz, $CDCl_3$, 0 °C): δ 16.4, 21.0, 103.8, 117.3, 118.8, 121.8, 123.3, 123.8, 125.5, 125.7, 129.7, 131.2, 134.6, 135.9, 142.2, 143.6, 143.9, 148.8, 149.2, 154.1. Two signals for the carbon atoms bonding to the boron atom were not observed due to

the quadrupolar relaxation of the boron atom. ^{11}B NMR (128 MHz, $CDCl_3$): δ 61.5. HRMS (APCI, positive): calcd for $C_{48}H_{38}BBrO_2S_2$: 879.0768 [$(M+H)^+$], found 879.0766.

[4,5-Bis(octyloxy)anthracen-9-yl]bis(4-bromobenzothiophen-3-yl)borane (13b). To a solution of **18b** (650 mg, 1.27 mmol) in dry Et_2O (50 mL) was added *n*-BuLi (1.62 M, 0.785 mL, 1.27 mmol) dropwise. After the reaction mixture was stirred at the same temperature for 40 min, trimethyl borate (1.13 mL, 10.1 mmol) was added. After stirring for 2 h, the reaction mixture was concentrated under reduced pressure. After the addition of dry hexane, the mixture was filtered. The filtrate was concentrated under reduced pressure to afford 657 mg (1.26 mmol, if pure) of **12b** as a crude product. Then, to a solution of **6** (898 mg, 2.65 mmol) in dry ether (53 mL) cooled at –78 °C was added *n*-BuLi (1.62 M, 1.64 mL, 2.66 mmol) dropwise. After the reaction mixture was stirred at the same temperature for 40 min, a solution of **12b** in dry ether (10 mL) was added to the mixture dropwise. The reaction mixture was gradually warmed to room temperature and filtered in the air. The filtrate was concentrated under reduced pressure. The resulting mixture was subjected to a silica gel column chromatography (PSQ 60B, 5/1 hexane/CH_2Cl_2, R_f = 0.25) to afford 370 mg (0.426 mmol, 34% yield, 2 steps) of **13b** as a yellow solid. mp: 141-142 °C. ^{1}H NMR (400 MHz, $(CD_3)_2SO$, 120 °C): *d* 0.88 (t, *J* = 6.8 Hz, 6H), 1.32-1.51 (m, 16H), 1.66 (quintet, *J* = 7.3 Hz, 4H), 1.96 (quintet, *J* = 6.9 Hz, 4H), 4.25 (t, *J* = 6.2 Hz, 4H), 6.77 (d, *J* = 7.6 Hz, 2H), 7.12 (t, *J* = 8.0 Hz, 2H), 7.26 (t, *J* = 7.8 Hz, 2H), 7.45 (d, *J* = 8.0 Hz, 2H), 7.54-7.56 (m, 4H), 8.04 (d, *J* = 8.0 Hz, 2H), 9.44 (s, 1H). ^{13}C NMR (100 MHz, $(CD_3)_2SO$, 120 °C): *d* 12.9, 21.2, 25.2, 28.0, 28.1, 28.3, 30.5, 67.7, 102.2, 117.1, 117.4, 120.9, 121.6, 123.5, 124.9, 125.2, 128.8, 134.9, 140.8, 143.0, 148.3, 154.4. Two signals for the carbon atoms bonding to the boron atom were not observed due to the quadrupolar relaxation of the boron atom. ^{11}B NMR (128 MHz, $CDCl_3$, 24 °C): *d* 61.0. HRMS (APCI, positive): calcd for $C_{46}H_{50}BBr_2O_2S_2$: 867.1707 [$(M+H)^+$], found 867.1714.

An anthrylborane precursor 11a. Compound **11a** was prepared from **13a** as a yellow solid in 71% yield in the similar manner as described for **10**. mp: >300 °C. ^{1}H NMR (400 MHz, $CDCl_3$): δ 2.23 (s, 12H), 2.35 (s, 6H), 6.27, (d, *J* = 8.0 Hz, 2H), 6.98 (s, 4H), 6.98 (t, *J* = 8.0 Hz, 2H), 7.26 (d, *J* = 8.0 Hz, 2H), 7.52 (t, *J* = 7.6 Hz, 2H), 7.88 (s, 2H), 7.90 (d, *J* = 7.6 Hz, 2H), 8.13 (d, *J* = 7.6 Hz, 2H), 9.87 (s, 1H). ^{13}C NMR (100 MHz, $CDCl_3$): δ 16.4, 21.0, 104.0, 115.6, 122.9, 123.0, 123.8, 124.9, 125.4, 127.2, 129.7, 131.2, 134.6, 135.1, 136.9, 142.0, 143.5, 149.4, 151.4, 154.2. Two signals for the carbon atoms bonding to the boron atom were not observed due to the quadrupolar relaxation of the boron atom. ^{11}B NMR (128 MHz,

$CDCl_3$): δ 56.3. HRMS (APCI, positive): calcd for $C_{48}H_{38}BO_2S_2$: 721.2401 [$(M+H)^+$], found 721.2406.

An anthrylborane precursor 11b. Compound **11b** was prepared from **13a** as a yellow solid in 62% yield in the similar manner as described for **10**. mp: 189-190 °C. ^{1}H NMR (400 MHz, $CDCl_3$): *d* 0.91 (t, *J* = 6.6 Hz, 6H), 1.33-1.52 (m, 16H), 1.69 (quintet, *J* = 7.4 Hz, 4H), 2.05 (quintet, *J* = 6.9 Hz, 4H), 4.24 (t, *J* = 6.4 Hz, 4H), 6.68, (d, *J* = 7.2 Hz, 2H), 7.11 (t, *J* = 7.8 Hz, 2H), 7.19 (d, *J* = 8.8 Hz, 2H), 7.51 (t, *J* = 7.8 Hz, 2H), 7.74 (s, 2H), 7.89 (d, *J* = 8.0 Hz, 2H), 8.13 (d, *J* = 7.6 Hz, 2H), 9.44 (s, 1H). ^{13}C NMR (100 MHz, $CDCl_3$): *d* 14.3, 22.9, 26.6, 29.6, 29.6, 29.7, 32.1, 68.3, 102.13, 116.0, 122.1, 122.9, 124.4, 125.0, 125.4, 127.2, 134.7, 136.9, 142.0, 143.6, 151.1, 155.7. Two signals for the carbon atoms bonding to the boron atom were not observed due to the quadrupolar relaxation of the boron atom. ^{11}B NMR (128 MHz, $CDCl_3$): *d* 58.1. HRMS (APCI, positive): calcd for $C_{46}H_{49}BO_2S_2$: 708.3262 (M^+), found 708.3269.

A planarized triarylborane 3a. To a solution of **11a** (100 mg, 0.139 mmol) in dry CH_2Cl_2 (14 mL) cooled at 0 °C was added 1.0 mL nitromethane solution of $FeCl_3$ (183 mg, 1.13 mmol) dropwise. After stirring for 22 h at room temperature, methanol (1 mL) was added to the reaction mixture. The mixture was passed through a short silica gel column (CH_2Cl_2 as an eluent), then reprecipitated from CH_2Cl_2/hexane by concentration under reduced pressure to afford 63 mg (0.088 mmol, 63% yield) of **3a** as a purple solid. mp: 282–283 °C. T_{d5}: 423.8 °C. ^{1}H NMR (400 MHz, $CDCl_3$): δ 2.25 (s, 12H), 2.39 (s, 6H), 6.62, (d, *J* = 8.0 Hz, 2H), 7.03 (s, 4H), 7.40 (t, *J* = 7.6 Hz, 2H), 7.86 (d, *J* = 7.6 Hz, 2H), 8.16 (d, *J* = 7.6 Hz, 2H), 8.31 (d, *J* = 8.0 Hz, 2H), 10.41 (s, 1H). ^{13}C NMR (100 MHz, $CDCl_3$): δ 16.5, 21.1, 116.1, 122.3, 122.6, 124.7, 125.3, 125.7, 125.9, 130.1, 130.9, 132.4, 132.9, 135.5, 136.5, 142.3, 143.7, 148.8, 151.9, 158.8, Two signals for the carbon atoms bonding to the boron atom were not observed due to the quadrupolar relaxation of the boron atom. ^{11}B NMR (128 MHz, $CDCl_3$): δ 39.5. HRMS (APCI, positive): calcd for $C_{48}H_{34}BO_2S_2$: 717.2088 [$(M+H)^+$], found 717.2090.

A planarized triarylborane 3b. To a solution of **11b** (175 mg, 0.246 mmol) in dry CH_2Cl_2 (25 mL) cooled at 0 °C was added 2 mL nitromethane solution of $FeCl_3$ (400 mg, 2.46 mmol) dropwise. After stirring for 1 h at room temperature, methanol (20 mL) was added to the reaction mixture. The mixture was filtered and solid was washed with CH_2Cl_2 and MeOH. The resulting solid was recrystalized from refluxed chlorobenzene to afford 95 mg (0.135 mmol, 55% yield) of **3b** as a purple solid. mp: > 300 °C. T_{d5}: 372.1 °C. ^{1}H NMR (400 MHz,

C_6D_5Cl, 100 °C): *d* 0.91 (t, *J* = 6.6 Hz, 6H), 1.34-1.52 (m, 16H), 1.62 (quintet, *J* = 7.2 Hz, 4H), 1.96 (quintet, *J* = 7.0 Hz, 4H), 4.18 (t, *J* = 6.4 Hz, 4H), 6.76, (d, *J* = 8.4 Hz, 2H), 7.30 (t, *J* = 7.8 Hz, 2H), 7.79 (d, *J* = 8.0 Hz, 2H), 8.14 (d, *J* = 8.0 Hz, 2H), 8.32 (d, *J* = 7.6 Hz, 2H), 9.99 (s, 1H). ^{13}C NMR and ^{11}B NMR were not obtained due to its poor solubility.

X-ray crystallographic analysis

X-ray crystallographic analysis of 5. Single crystals of **5** suitable for X-ray crystallographic analysis were obtained by recrystallization from CH_2Cl_2 and hexane using vapor diffusion method. The measurement was performed at 123 K. Total 29716 reflections were collected, among which 7918 reflections were independent (R_{int} = 0.0579). The crystal data are as follows: Formula $C_{24}H_{12}BBr_3S_3$; FW = 647.06, crystal size 0.20 × 0.20 × 0.02 mm, monoclinic, $P2_1/a$, (#14), a = 13.411(5), b = 21.868(8), c = 16.401(6) Å, β = 107.830(2)°, V = 4579(3) Å^3, Z = 8, D_{calcd} = 1.877 g cm^{-3}; R_1 = 0.1206 ($I > 2s(I)$), wR_2 = 0.2849 (all data), GOF = 1.146.

X-ray crystallographic analysis of 10. Single crystals of **10** suitable for X-ray crystallographic analysis were obtained by recrystallization from 1,2-dichloroethane and heptane using vapor diffusion method. The measurement was performed at 123 K. Total 71585 reflections were collected, among which 14620 reflections were independent (R_{int} = 0.0901). The crystal data are as follows: Formula $C_{31}H_{19}BClS_2$; FW = 501.84, crystal size 0.30 × 0.01 × 0.01 mm, monoclinic, $P2_1/n$, (#14), a = 17.584(7), b = 20.312(8), c = 26.769(10) Å, β = 97.9550(14)°, V = 9469 (6) Å^3, Z = 16, D_{calcd} = 1.408 g cm^{-3}; R_1 = 0.0973 ($I > 2s(I)$), wR_2 = 0.2359 (all data), GOF = 1.183.

X-ray crystallographic analysis of 3a. Single crystals of **3a** suitable for X-ray crystallographic analysis were obtained by vapor diffusion of octane into a toluene solution. The measurement was performed at 123 K. Total 36775 reflections were collected, among which 7299 reflections were independent (R_{int} = 0.0256). The crystal data are as follows: Formula $C_{56}H_{51}BO_2S_2$; FW = 830.90, crystal size 0.30 × 0.10 × 0.02 mm, monoclinic, $P2_1/n$, (#14), a = 8.5696(14), b = 13.162(2), c = 38.189(6) Å, β = 95.0096(7)°, V = 4291.1(12) Å^3, Z = 4, D_{calcd} = 1.286 g cm^{-3}; R_1 = 0.0411 ($I > 2s(I)$), wR_2 = 0.1063 (all data), GOF = 1.053. CCDC number: 873940.

X-ray crystallographic analysis of [K(cryptand)]$^+$·3aF$^-$. Single crystals of **[K(cryptand)]$^+$·3aF$^-$** suitable for X-ray crystallographic analysis were obtained by vapor

diffusion of hexane into a benzene solution of **3a** with potassium fluoride and [2.2.2]cryptand. The measurement was performed at 123 K. Total 63997 reflections were collected, among which 22284 reflections were independent (R_{int} = 0.0660). The crystal data are as follows: Formula $C_{142.64}H_{154.28}B_2F_2K_2N_4O_{16}S_4$; FW = 2446.72, crystal size 0.30 × 0.15 × 0.03 mm, triclinic, *P*-1, (#2), a = 18.9618(4), b = 19.21270(10), c = 20.76030(10) Å, α = 74.793(12)°, b = 73.353(12)°, g = 62.6114(10)°, V = 6357.72(41) Å^3, Z = 2, D_{calcd} = 1.278 g cm^{-3}; R_1 = 0.1107 ($I > 2s(I)$), wR_2 = 0.3887 (all data), GOF = 1.141. CCDC number: 873941.

Theoretical calculations

The geometry optimizations for all compounds were performed using Gaussian 09 program[21] at the B3LYP/6-31G* level of theory. The time-dependent density functional theory (TD-DFT) calculations at the optimized geometry were conducted at the same level of theory.

References

(1) (a) Entwistle, C. D.; Marder, T. B. *Chem. Mater.* **2004**, *16*, 4574. (b) Yamaguchi, S.; Wakamiya, A. *Pure Appl. Chem.* **2006**, *78*, 1413. (c) Bosdet, M. J. D.; Piers, W. E. *Can. J. Chem.* **2008**, *86*, 8. (d) Jäkle, F. *Chem. Rev.* **2010**, *110*, 3985. (e) Wade, C. R.; Broomsgrove, A. E. J.; Aldridge, S.; Gabbäi, F. P. *Chem. Rev.* **2010**, *110*, 3958. (f) Hudson, Z. M.; Wang, S. *Dalton Trans.* **2011**, *40*, 7805.

(2) (a) Bosdet, M. J. D.; Piers, W. E.; Sorensen, T. S.; Parves, M. *Angew. Chem. Int. Ed.* **2007**, *46*, 4940. (b) Brothers, P. J. *Chem. Commun.* **2008**, 2090. (c) Marwitz, A. J. V.; Matus, M. H.; Zakharov, L. N.; Dixon, D. A.; Liu, S.-Y. *Angew. Chem., Int. Ed.* **2009**, *48*, 973. (d) Hatakeyama, T.; Hashimoto, S.; Seki, S.; Nakamura, M. *J. Am. Chem. Soc.* **2011**, *133*, 18614.

(3) (a) Yamaguchi, S.; Shirasaka, T.; Akiyama, S.; Tamao, K. *J. Am. Chem. Soc.* **2002**, *124*, 8816. (b) Yuan, Z.; Entwistle, C. D.; Collings, J. C.; Albesa-Jové, D.; Batsanov, A. S.; Howard, J. A. K.; Taylor, N. J.; Kaiser, H. M.; Kaufmann, D. E.; Poon, S.-Y.; Wong, W.-Y.; Jardin, C.; Fathallah, S.; Boucekkine, A.; Halet, J.-F.; Marder, T. B. *Chem. Eur. J.* **2006**, *12*, 2758. (c) Wakamiya, A.; Mishima, K.; Ekawa, K.; Yamaguchi, S. *Chem. Commun.* **2008**, 579. (d) Mercier, L. G.; Piers, W. E.; Parvez, M. *Angew. Chem. Int. Ed.* **2009**, *48*, 6108. (e) Caruso, A. Jr., Siegler, M. A.; Tovar, J. D. *Angew. Chem. Int. Ed.* **2010**, *49*, 4213.

(4) Hertz, V. M.; Bolte, M.; Lerner, H.-W.; Wagner, M. *Angew. Chem. Int. Ed.* **2015**, *54*, 8800.

(5) (a) Zhou, Z.; Wakamiya, A.; Kushida, T.; Yamaguchi, S. *J. Am. Chem. Soc.* **2012**, *134*, 4529. (b) Kushida, T.; Zhou, Z.; Wakamiya, A.; Yamaguchi, S. *Chem. Commun.* **2012**, *48*, 10715. (c) Kushida, T.; Yamaguchi, S. *Organometallics* **2013**, *32*, 6654. (d) Shuto, A.; Kushida, T.; Fukushima, T.; Kaji, H.; Yamaguchi, S. *Org. Lett.* **2013**, *15*, 6234. (e) Kushida, T.; Camacho, C.; Shuto, A.; Irle, S.; Muramatsu, M.; Katayama, T.; Ito, S.; Nagasawa, Y.; Miyasaka, H.; Sakuda, E.; Kitamura, N.; Zhou, Z.; Wakamiya, A.; Yamaguchi, S. *Chem. Sci.* **2014**, *5*, 1296.

(6) (a) Reisch, H. A.; Bratcher, M. S.; Scott, L. T. *Org. Lett.* **2000**, *2*, 1427. (b) Alberico, D.; Scott, M. E.; Lautens, M. *Chem. Rev.* **2007**, *107*, 174. (c) Pascual, S.; Mendoza, P.; Echavarren, A. M. *Org. Biomol. Chem.*, **2007**, *5*, 2727.

(7) (a) Harrowven, D. C.; Guy, I. L.; Nanson L. *Angew. Chem., Int. Ed.* **2006**, *45*, 2242. (b) Rajca, A.; Miyasaka, M.; Xiao, S.; Boratyński, P. J.; Pink, M.; Rajca S. *J. Org. Chem.* **2009**, *74*, 9105. (c) Castillo, R. R.; Burgos, C.; Vaquero, J. J.; Alvarez-Builla J. *Eur. J. Org. Chem.* **2011**, 619.

(8) a) Watson, M.; Fechtenkötter, A.; Müllen, K. *Chem. Rev.* **2001**, *101*, 1267. (b) Wu, J.; Pisula, W.; Müllen, K. *Chem. Rev.* **2007**, *107*, 718.

(9) King, B. T.; Kroulík, J.; Robertson, C. R.; Rempala, P.; Hilton, C. L.; Korinek, J. D.; Gortari, L. M. *J. Org. Chem.* **2007**, *72*, 2279.

(10) (a) Davis, N. K. S.; Pawlicki, M.; Anderson H. L. *Org. Lett.* **2008**, *10*, 3945. (b) Davis, N. K. S.; Thompson, A. L.; Anderson H. L. *Org. Lett.* **2010**, *12*, 2124. (c) Davis, N. K. S.; Thompson, A. L.; Anderson H. L. *J. Am. Chem. Soc.* **2011**, *133*, 30. (d) Zeng, L.; Jiao, C.; Huang, X.; Huang, K.-W.; Chin, W.-S.; Wu, J. *Org. Lett.* **2011**, *13*, 6026.

(11) Zettler, F.; Hausen, H. D.; Hess, H. *J. Organomet. Chem.* **1974**, *72*, 157.

(12) a) Blount, J. F.; Finocchiaro, P.; Gust, D.; Mislow, K. *J. Am. Chem. Soc.* **1973**, *95*, 7019. (b) Olmstead, M. M.; Power, P. P. *J. Am. Chem. Soc.* **1986**, *108*, 4235.

(13) (a) Agou, T.; Kobayashi, J.; Kawashima, T. *Chem. Eur. J.* **2007**, *13*, 8051. (b) Wakamiya, A.; Mori, K.; Yamaguchi, S. *Angew. Chem. Int. Ed.* **2007**, *46*, 4273. (c) Kano, N.; Furuta, A.; Kanbe, T.; Yoshino, J.; Shibata, Y.; Kawashima, T.; Mizorogi, N.; Nagase, S. *Eur. J. Inorg. Chem.* **2012**, 1584.

(14) (a) Dai, J.; Yuan, J.; Giannozzi, P. *Appl. Phys. Lett.* **2009**, *95*, 232105. (b) Zhou, Y. G.; Zu, X. T.; Gao, F.; Nie, J. L.; Xiao, H. Y. *J. Appl. Phys.* **2009**, *105*, 014309. (c) Kong, X.; Chen, Q. *J. Mater. Chem.* **2012**, *22*, 15336. (d) Muhich, C. L.; Westcott IV, J. Y.; Morris, T. C.; Weimer, A. W.; Musgrave, C. B. *J. Phys. Chem. C,* **2013**, *117*, 10523. (e) Sharma, S.; Verma, A. S. *Phys. B,* **2013**, *427*, 12. (f) Seyed-Talebi, S. M.; Beheshtian, J.; Neek-amal, M. *J. Appl. Phys.* **2013**, *114*, 124307.

(15) (a) Solé, S.; Gabbaï, F. P. *Chem. Commun.* **2004**, 1284. (b) Sundararaman, A.; Venkatasubbaiah, K.; Victor, M.; Zakharov, L. N.; Rheingold, A. L.; Jäkle, F. *J. Am. Chem. Soc.* **2006**, *128*, 16554. (c) Pakkirisamy, T.; Venkatasubbaiah, K.; Kassel, W. S.; Rheingold, A. L.; Jäkle, F. *Organometallics,* **2008**, *27*, 3056.

(16) Nöth, H.; Wrackmeyer, B. *NMR Basic Principles and Progress, Vol. 14, Nuclear magnetic Resonance Spectroscopy of Boron Compounds,* Springer-Verlag, Berlin, New York, 1978.

(17) All the crystal structures of triarylborane fluoride complexes registered in the CCDC database are examined for reference.

(18) Sheldrick, G. M. SHELX-97, *Program for the Refinement of Crystal Structures*; University of Göttingen: Göttingen, Germany, 1997.

(19) Bradshaw, J. D.; Guo, L.; Tessier, C. A.; Youngs, W. J. *Organometallics* **1996**, *15*, 2582.

(20) Filthaus, M.; Oppel, I. M.; Bettinger H. F. *Org. Biomol. Chem.* **2008**, *6*, 1201.

(21) Gaussian 09 (Revision A.02), Frisch, M. J.; Trucks, G. W.; Schlegel, H. B.; Scuseria, G.E.; Robb, M. A.; Cheeseman, J. R.; Scalmani, G.; Barone, V.; Mennucci, B.; Petersson, G. A.; Nakatsuji, H.; Caricato, M.; Li, X.; Hratchian, H. P.; Izmaylov, A. F.; Bloino, J.; Zheng, G.; Sonnenberg, J. L.; Hada, M.; Ehara, M.; Toyota, K.; Fukuda, R.; Hasegawa, J.; Ishida, M.; Nakajima, T.; Honda, Y.; Kitao, O.; Nakai, H.; Vreven, T.; Montgomery, Jr., J. A.; Peralta, J. E.; Ogliaro, F.; Bearpark, M.; Heyd, J. J.; Brothers, E.; Kudin, K. N.;Staroverov, V. N.; Kobayashi, R.; Normand, J.; Raghavachari, K.; Rendell, A.; Burant, J. C.; Iyengar, S. S.; Tomasi, J.; Cossi, M.; Rega, N.; Millam, J. M.; Klene, M.; Knox, J. E.; Cross, J. B.; Bakken, V.; Adamo, C.; Jaramillo, J.; Gomperts, R.; Stratmann, R. E.; Yazyev, O.; Austin, A. J.; Cammi, R.; Pomelli, C.; Ochterski, J. W.; Martin, R. L.; Morokuma, K.; Zakrzewski, V. G.; Voth, G. A.; Salvador, P.; Dannenberg, J. J.; Dapprich,S.; Daniels, A. D.; Farkas, O.; Foresman, J. B.; Ortiz, J. V.; Cioslowski, J.; Fox, D. J. Gaussian, Inc., Wallingford CT, 2009.

(22) Saito, S.; Matsuo, K.; Yamaguchi, S. *J. Am. Chem. Soc.* **2012**, *134*, 9130.

Chapter 2

Photodissociation of B–N Lewis Adducts with a Partially Fused Trinaphthylborane

Abstract: The synthesis of a planarized trinaphthylborane with partially fused structure is presented. This compound shows not only high chemical and thermal stability but also sufficient Lewis acidity to form Lewis acid–base adducts with pyridine derivatives in solution. The B–N Lewis acid–base adducts exhibit unprecedented photodissociation behavior in the excited state, reminiscent of the photogeneration of carbenium ions from triarylmethane leuco dyes. Consequently, these B–N Lewis acid–base adducts exhibit dual fluorescence emission arising from the initial tetracoordinate B–N Lewis acid–base adducts and the photodissociated tricoordinate boranes.

2-1. Introduction

Incorporation of a tricoordinate, trivalent boron atom, which is isoelectronic to a carbenium ion, into π-conjugated skeletons enables the construction of charge-neutral electron-deficient molecules.[1] Boron-containing π-systems readily react with Lewis bases to form the corresponding tetracoordinate species. This fundamental reactivity can be used to induce fascinating electronic properties and functions. In this context, a primary strategy is the generation of rigid π-conjugated skeletons with intense fluorescence by the intramolecular coordination with a *N*-heteroaryl group, such as in BODIPY and related dyes.[2] Recently, Wang *et al*. found an intriguing photorearrangement of intramolecularly *N*-heteroaryl-coordinated boron compounds, in which a boracyclopropane is formed, while the B–N bond remains intact (Figure 2-1a).[3] Their intensive investigations on the scope of this reaction demonstrated a potential use for these compounds in new photochromic systems. In comparison, the reactivity of intermolecular complexes between boranes and neutral Lewis bases has not received much attention from a design perspective regarding functional materials. For this type of complex, Braunschweig and Engels *et al*. recently reported an intriguing type of photoreactivity: a photomigration of an intermolecular complex between an electron-accepting borole and 2,6-lutidine (Figure 2-1b).[4]

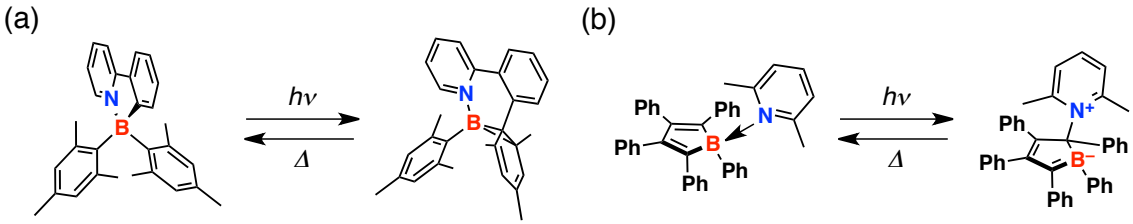

Figure 2-1. Examples of photochromic systems based on the B–N Lewis acid–base adducts.

In association with them, the author has found yet another, unprecedented type of photoreactivity for intermolecularly coordinated triarylborane-pyridine complexes, which photodissociate in the excited state (Figure 2-2a) and exhibit dual fluorescence. While a laser photolysis of borane carbonyl (BH_3CO) is known as a similar type of reaction,[5] the present B–N photodissociation is reminiscent of the photogeneration of carbenium ions from triarylmethane leuco dyes (Figure 2-2b).[6] In this chapter, the author disclosed the synthesis of a partially fused trinaphthylborane **1**, which shows higher Lewis acidity than those of other planarized triarylboranes **2**[7] and **3**[8] previously reported (Figure 2-2c). In addition, the author discusses the photodissociation of its Lewis acid–base adducts with various pyridine derivatives.

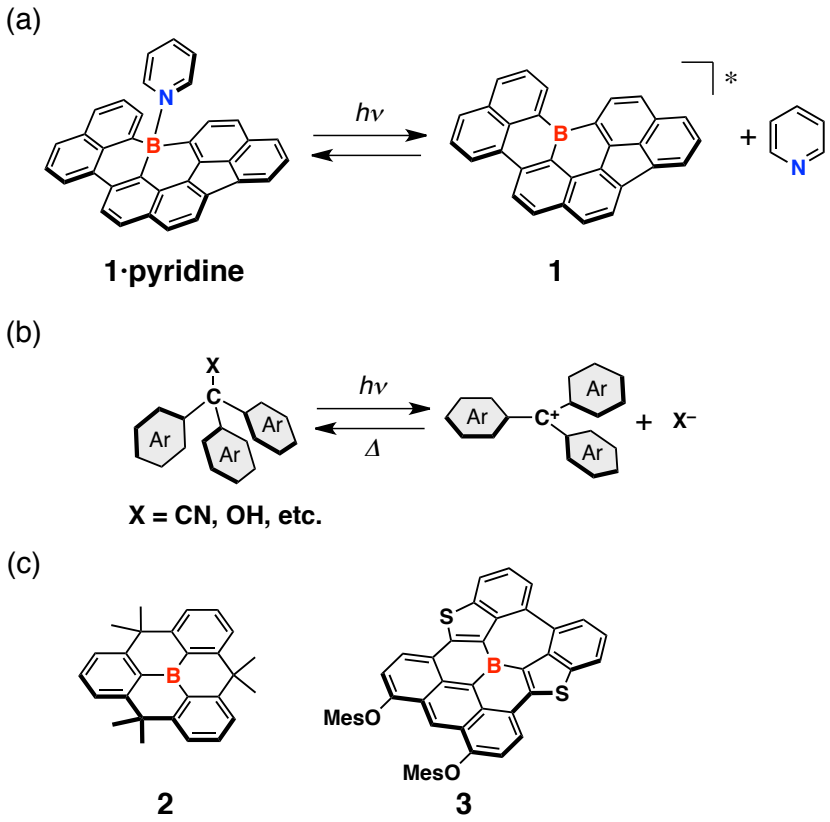

Figure 2-2. (a) Photodissociation of a partially fused trinaphthylborane **1**·pyridine adduct, (b) photogeneration of carbenium ions from triarylmethane leuco dyes, and (c) the structure of some relevant planarized triarylboranes. Reprinted with permission from [19]. Copyright © 2014, American Chemical Society.

2-2. Results and discussion

Synthesis

In chapter 1, the author have succeeded in the synthesis of boron-embedded polycyclic π-conjugated molecule **3**.[8] In order to develop a more convenient synthetic pathway to structurally simpler boron-embedded π-skeletons, the author attempted a three-fold cyclization of tris(8-bromonaphthalen-1-yl)borane **4** (Scheme 2-1). The author envisioned that 8-bromonaphthalene units are likely to construct the six-membered ring rather than seven-membered ring previously observed and to give C_3 symmetric product **5**. Thus, precursor **4** was treated with $(TMS)_3SiH$ in the presence of 1,1′-azobis(cyclohexanecarbonitrile) (ABCN) as a radical initiator in toluene at 120 °C,[8] which resulted in the formation of the partially fused trinaphthylborane **1** with an unexpected connectivity pattern with respect to the three naphthyl groups as the major product. Compound **1** was isolated as a red solid in 26% yield. Conversely, the expected fused product **5** with C_3 symmetry was not observed and any other by-products were not able to be isolated. Although the detailed reaction mechanism still remains unclear, **1** is likely generated from successive intramolecular radical cyclizations including not only 6-*endo-trig* cyclization but also 5-*exo-trig* cyclization,[9] followed by a skeletal rearrangement (Scheme 2-2).

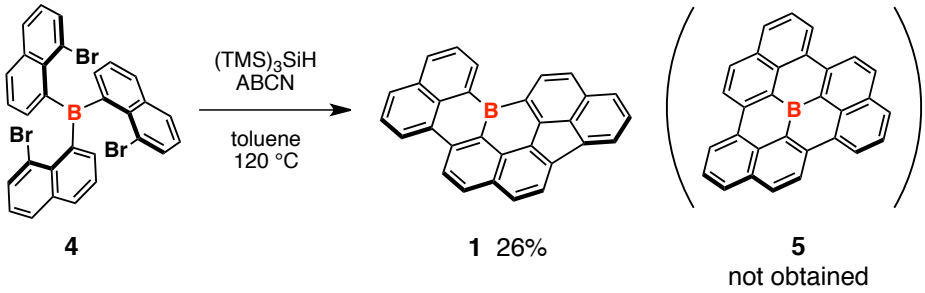

Scheme 2-1. Synthesis of a partially fused trinaphthylborane **1**. Reprinted with permission from [19]. Copyright © 2014, American Chemical Society.

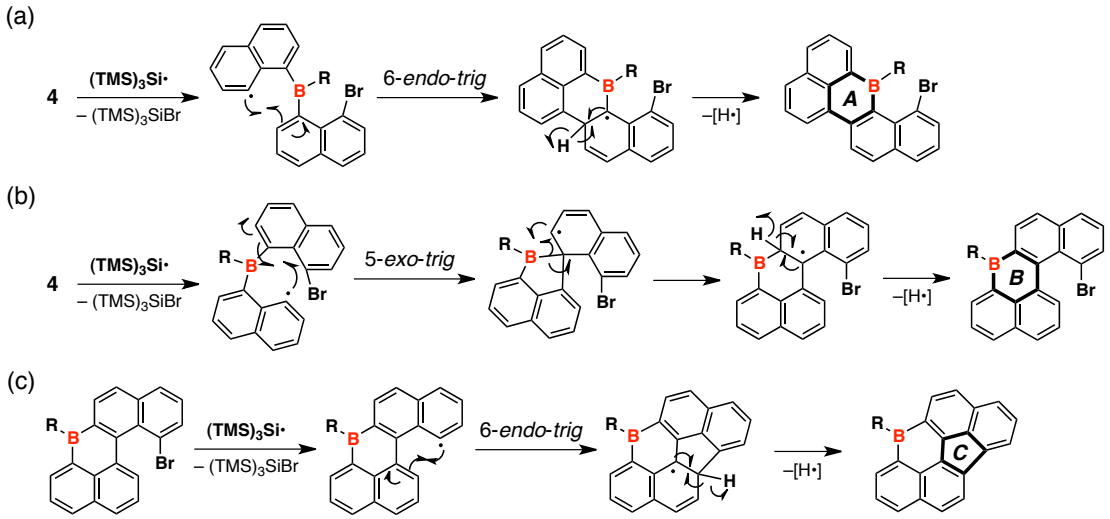

Scheme 2-2. Plausible mechanism for the formation of **1**. Reprinted with permission from [19]. Copyright © 2014, American Chemical Society.

Trinaphthylborane **1** showed notably high chemical stability. For example, even after more than one month in water-containing CH_2Cl_2, no degradation was observed for **1**, as evident from UV-Vis absorption measurements (Figure 2-3a). The high stability is in contrast to the chemical sensitivity of the parent tri(naphthalene-1-yl)borane, which rapidly ($t_{1/2}$ = 2.8 h) decomposes in a CH_2Cl_2 solution in the air (Figure 2-3b).

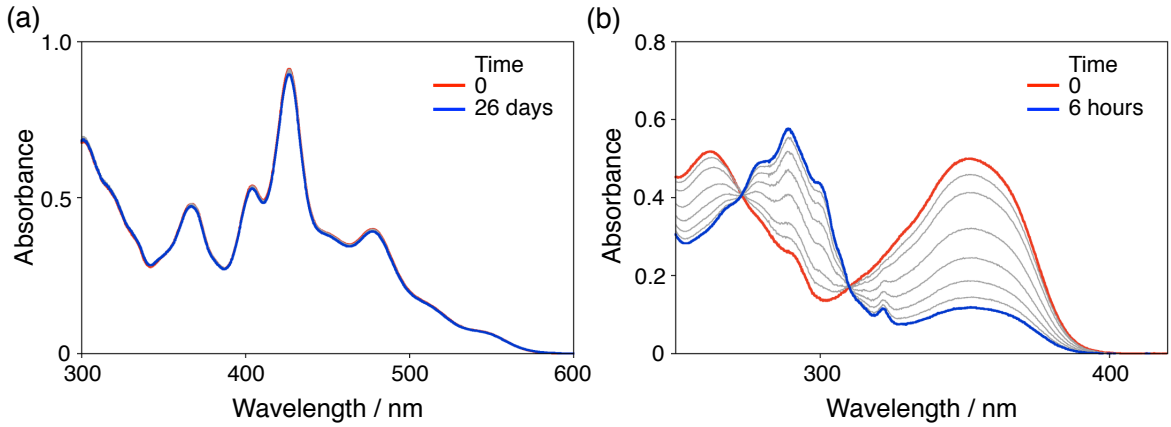

Figure 2-3. UV-Vis absorption spectral change in the air of a CH_2Cl_2 solution of **1** (3.3×10^{-5} M) and (b) tri(naphthalen-1-yl)borane (3.0×10^{-5} M). Reprinted with permission from [19]. Copyright © 2014, American Chemical Society.

Importantly, the boron moiety of **1** remained intact during further functionalization reactions (Scheme 2-3). For example, the electrophilic bromination of **1** with *N*-bromosuccinimide (NBS) successfully afforded brominated derivative **6** in 80% yield. A subsequent Suzuki-Miyaura cross-coupling reaction between **6** and phenylboronic acid under

basic aqueous condition produced phenylated derivative **7** in 59% yield. The B–C bonds at the central borane are not cleaved in this reaction probably due to the chelating effect of the surrounding polycyclic framework. The observed chemical tolerance suggests the possibility to straightforwardly obtain a variety of derivatives of this trinaphthylborane core skeleton via well-established synthetic techniques. Furthermore, the high thermal stability of **1** was demonstrated by thermogravimetric analysis (TGA). The decomposition temperature of 5% weight loss (T_{d5}) under a nitrogen atmosphere was determined to be 384 °C. Accordingly, it was possible to sublimate **1** at 250 °C under the vacuum pressure of 10^{-5} Torr.

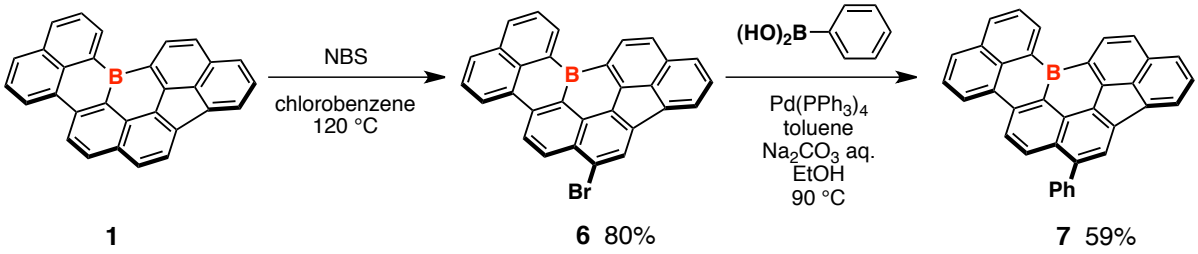

Scheme 2-3. Functionalization of **1**. Reprinted with permission from [19]. Copyright © 2014, American Chemical Society.

X-ray crystallographic analysis

The bond connectivity in the fused trinaphthylborane skeleton was unequivocally confirmed by X-ray crystallographic analysis of **6** and **7**. Unfortunately, single crystals of the parent compound **1** could not be obtained because of low crystallinity. The crystallographic analysis of **6** confirmed that one of the three naphthyl groups is connected to the boron center in its 2-position (Figure 2-4). The three naphthyl groups are connected to each other via three $C(sp^2)$–$C(sp^2)$ bonds. Consequently, the compound forms a nine ring-fused $C_{30}B$ skeleton with a benzofluoranthene substructure. The central boron atom adopts a trigonal planar geometry with sum of the C–B–C bond angles of 360.0°, while C1–B–C3 bond angle between the non-connected naphthyl groups is larger (126.9(6)°) than the others (115.2(6)° and 117.9(6)°), resulting in decreased steric repulsion between the hydrogen atoms at the bay positions. Therefore, the fused trinaphthylborane skeleton adopts a highly planar geometry. Another notable structural feature of **6** is the slight elongation of the B–C bonds, which amount to 1.548(11), 1.567(10), and 1.603(10) Å for B–C1, B–C2, and B–C3 bonds, respectively. These bond lengths are bigger than those in planarized triarylboranes **2** (1.52 Å)[7] and **3** (1.51–1.54 Å)[8] comparable to typical B–C bond lengths in unconstrained triarylboranes (1.57–1.59 Å).[10] The crystal packing of **6** is best described by a columnar π-stacked structure, where the average distance between the mean planes of the polycyclic geometry is 3.45 Å (Figure 2-5).

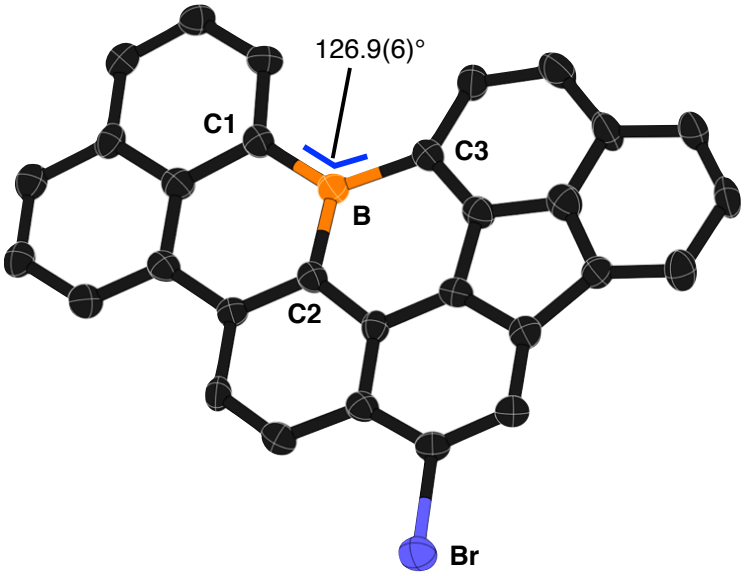

Figure 2-4. Crystal structure of **6** (50% probability of thermal ellipsoids, hydrogen atoms and disordered Br atom are omitted for clarity). Reprinted with permission from [19]. Copyright © 2014, American Chemical Society.

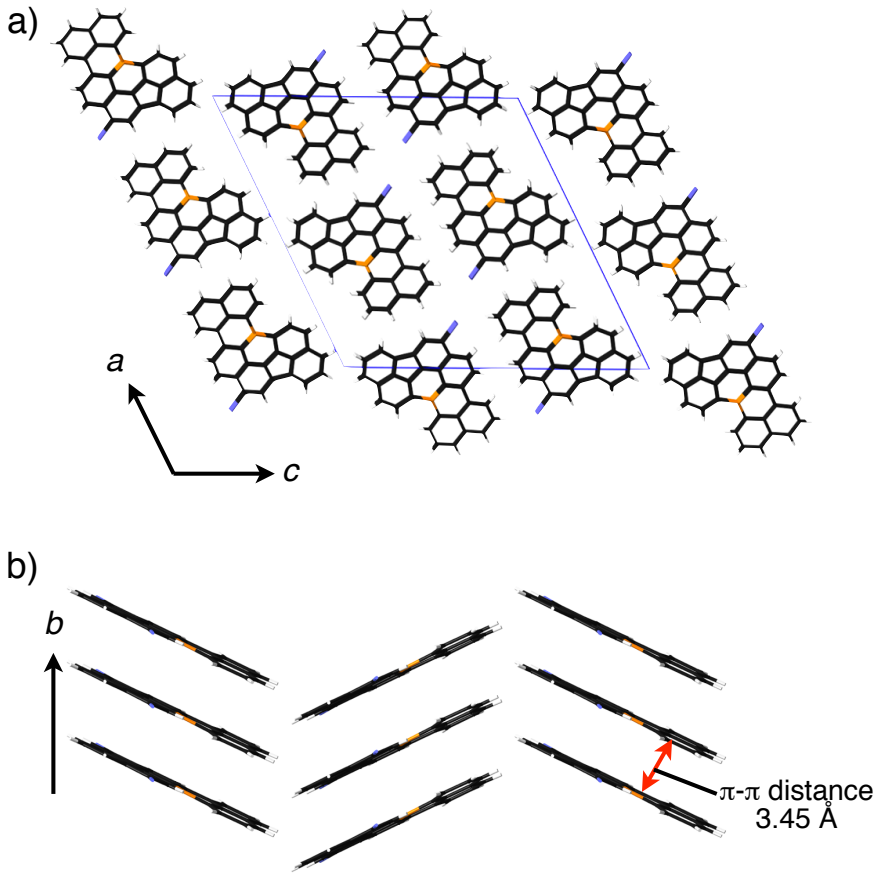

Figure 2-5. (a) Crystal packing of **6** along b-axis of crystal lattice and (b) side view of columnar π-stacked structures. Reprinted with permission from [19]. Copyright © 2014, American Chemical Society.

The X-ray crystallographic analysis of **7** displayed a similar planar geometry of the π-skeleton (Figure 2-6), including the large C1'–B'–C3' bond angles (127.84(17)°) and long B–C bond lengths (1.540(3), 1.571(3), and 1.590(3) Å for B'–C1', B'–C2', and B'–C3' bonds, respectively). The substituted phenyl ring is tilted 57.2 degrees away from the plane of the connected naphthalene ring. In the crystal packing of **7**, the flat polycyclic moieties construct the face-to-face π-stacked structure, in which two types of π-stacking modes are observed alternately (Figure 2-7). One shows a large π-orbital overlap with a shorter distance between π-planes of 3.42 Å, while the other shows a small π-orbital overlap with a relatively longer distance between π-planes of 3.51 Å. This structural features is unprecedented for air-stable triarylboranes. The ability to form tight π-stacked structures would be beneficial not only for the construction of supramolecules or discotic liquid crystals but also for effective carrier transport in the solid state.

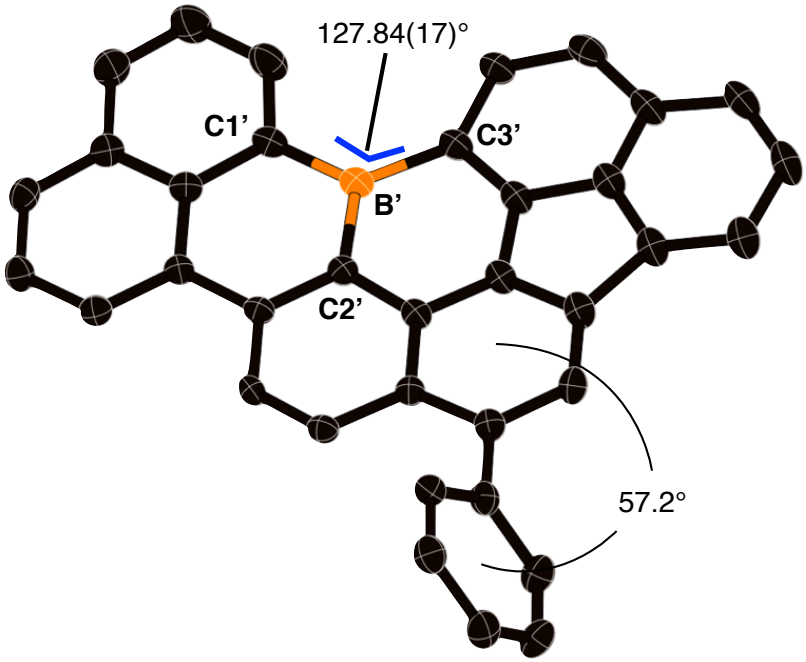

Figure 2-6. Crystal structure of **7** (50% probability of thermal ellipsoids, hydrogen atoms are omitted for clarity).

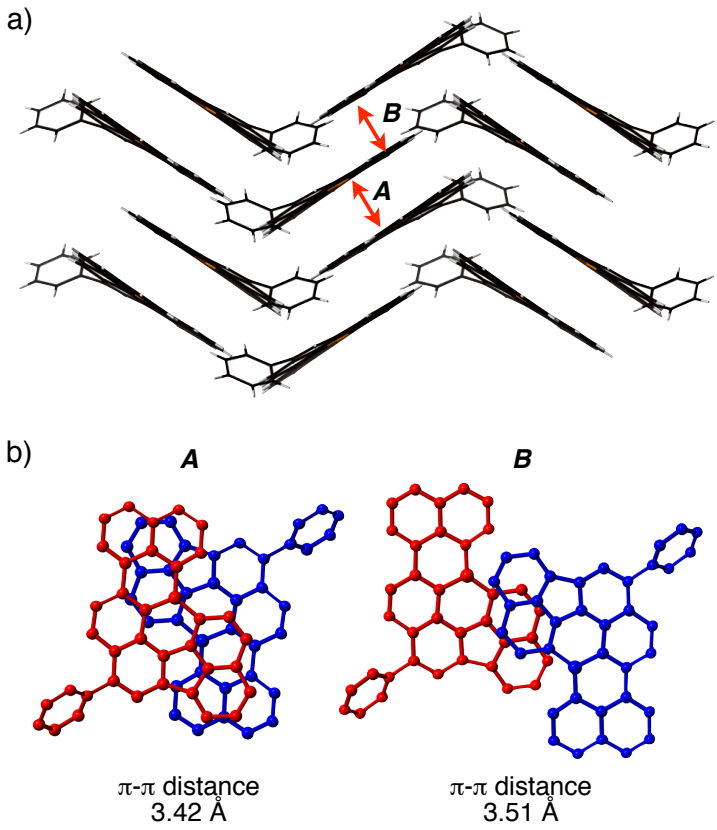

Figure 2-7. (a) Crystal packing of **7** and (b) two different π-stacking modes in the packing structure.

Carrier transporting properties

In this context, the carrier transporting property has been evaluated. A bottom-gate top-contact OFET device was fabricated using a heavily *n*-doped Si substrate with 100-nm thermally grown SiO_2 film as a gate insulator. A thin film (50 nm thickness) of **1** as the active layer was vacuum-deposited on the Si/SiO_2 substrate. Then, gold electrodes (40 nm thickness) were vacuum-deposited as the source and drain on top of the organic films through a shadow mask. The drain-source channel length (L) and width (W) were 40 μm and 200 μm, respectively. The OFET properties were measured with an Agilent Technologies B1500A semiconducting parameter analyzer at room temperature under the pressure of 1.0×10^{-3} Pa. The field-effect mobility (μ_{FET}) was calculated in the saturation regime (V_d = –40 V and 40 V for the hole mobility μ_h and electron mobility μ_e, respectively) of the I_d using the following equation, where I_d is the drain–source current, C_i is the capacitance of the SiO_2 insulator, and V_d, V_g, and V_{th} are the drain–source, gate, and threshold voltages, respectively.

$$I_d = (WC_i / 2L)\, \mu_{FET}\, (V_g - V_{th})^2$$

The obtained OFET device of **1** showed ambipolar carrier transporting abilities with a hole mobility of $\mu_h = 9.3 \times 10^{-6}$ cm^2 V^{-1} s^{-1} with a V_{th} of –14.2 V and an electron mobility of $\mu_e = 1.7 \times 10^{-5}$ cm^2 V^{-1} s^{-1} with a V_{th} of 15.6 V (Figures 2-8). Although the performance is poor, this is the first OFET device of an air-stable triarylborane.

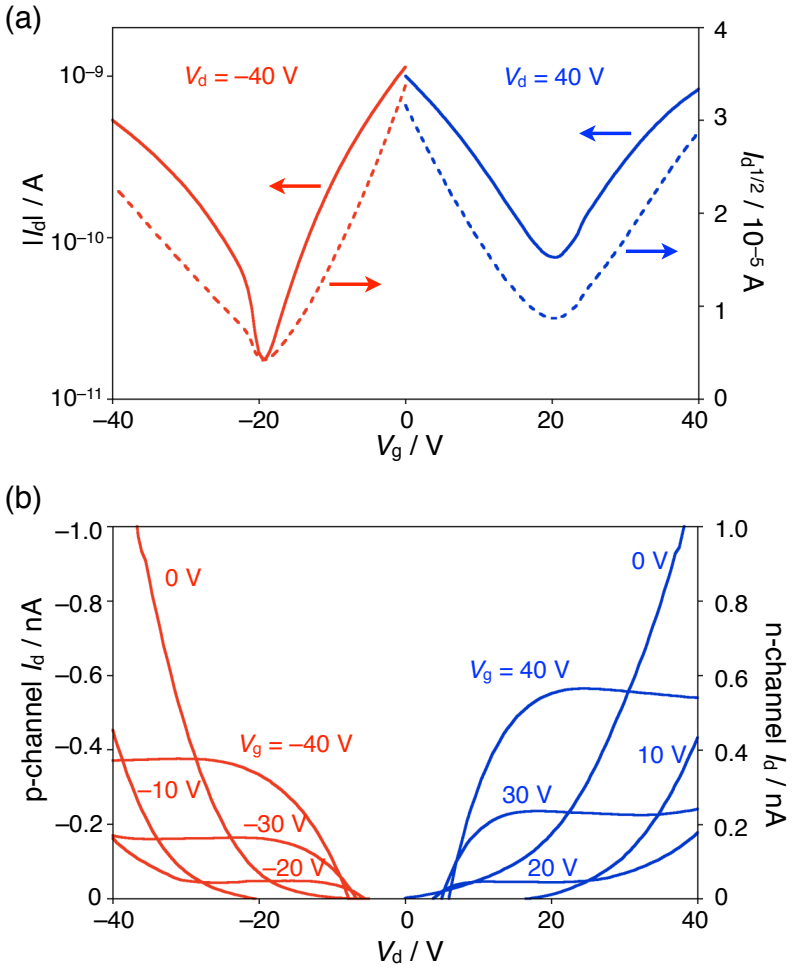

Figure 2-8. OFET characteristics of **1**: (a) Transfer curves in the saturation regime and (b) output curves at different V_g for p-channel (red) and n-channel (blue). Reprinted with permission from [19]. Copyright © 2014, American Chemical Society.

Photophysical properties

The photophysical property measurements were conducted for the partially fused trinaphthylborane **1**. The toluene solutions of **1** exhibited orange color and an orange luminescence was observed under a UV lamp. In the UV-Vis absorption spectroscopy, **1** showed its longest absorption maximum at 546 nm and another intense absorption at 429 nm (Figure 2-9). These absorption wavelengths are significantly longer than that of non-fused trinaphthylborane (352 nm in CH_2Cl_2, Figure 2-3b), demonstrating the effective π expansion due to the ring fusion between the naphthyl groups through C(sp^2)–C(sp^2) bonds. Moreover,

this compound showed orange fluorescence at the maximum wavelength of 573 nm with a fluorescence quantum yield (Φ_F) of 0.15. Fluorescence lifetime (τ) of **1** in toluene was determined by time-resolved fluorescence spectroscopy to be 10.7 ns (Figure 2-10). According to the Φ_F and τ values, the radiative (k_r) and non-radiative (k_{nr}) decay rate constants from the excited singlet states were calculated to be 1.4×10^7 s^{-1} and 7.9×10^7 s^{-1}, respectively. These absorption and fluorescence bands showed only slight solvent polarity effects (Figure 2-11 and Table 2-1), indicating the small contribution of intramolecular charge transfer character similar to completely fused triarylborane **3**.[8]

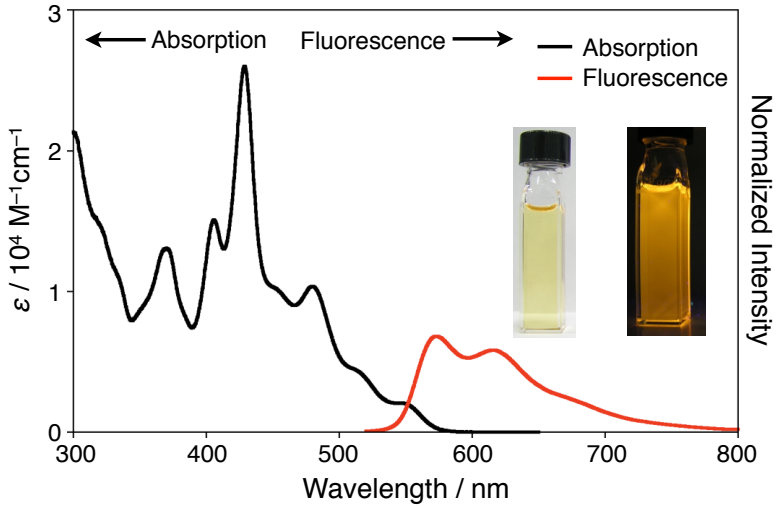

Figure 2-9. Absorption (black) and fluorescence spectra (red) of **1** in toluene. Reprinted with permission from [19]. Copyright © 2014, American Chemical Society.

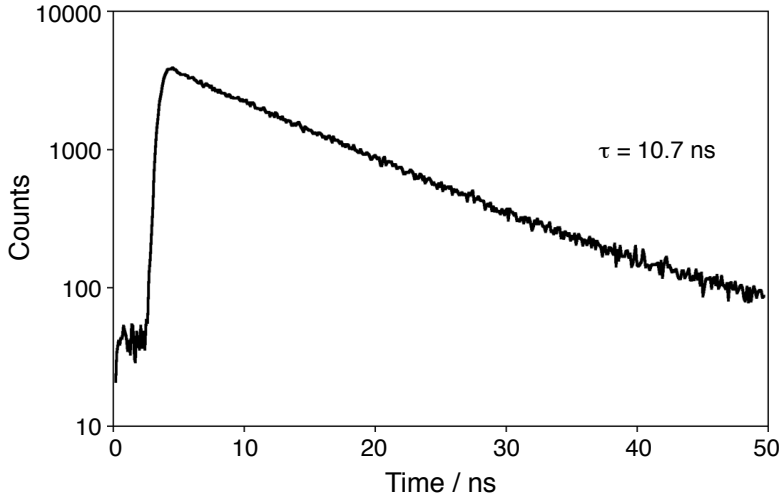

Figure 2-10. Fluorescence decay profile and lifetime of **1** in toluene with the excitation at 377 nm ($[\mathbf{1}]_0 = 1.0 \times 10^{-5}$ M). Reprinted with permission from [19]. Copyright © 2014, American Chemical Society.

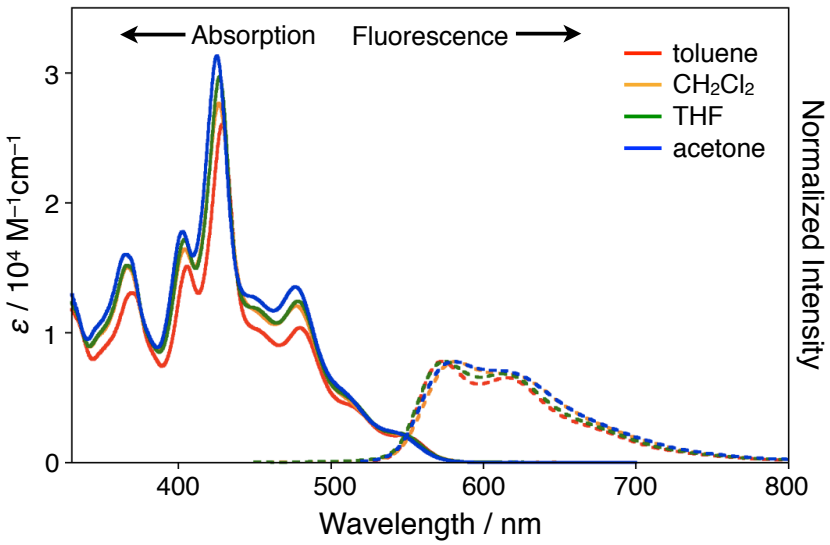

Figure 2-11. Absorption (solid line) and fluorescence spectra (dashed line) of **1** in various solvents. Reprinted with permission from [19]. Copyright © 2014, American Chemical Society.

Table 2-1. The Longest Absorption Wavelengths and Maximum Fluorescence Wavelengths of **1** in Various Solvents

solvent	toluene	CH_2Cl_2	THF	acetone
λ_{abs} / nm	480	477	477	477
λ_{em} / nm	573	582	575	581

Reprinted with permission from [19]. Copyright © 2014, American Chemical Society.

Electrochemical property

Cyclic voltammetry of **1** was conducted in *o*-dichlorobenzene and THF using *n*-Bu_4NPF_6 as supporting electrolyte in order to investigate the electrochemical properties. Compound **1** showed two reversible redox waves for reduction process at $E_{1/2}$ = –1.53 V and –2.13 V (vs Fc/Fc^+) in *o*-dichlorobenzene (Figure 2-12a), demonstrating that the generated radical anion and dianion are stable under the measurement conditions. On the other hand, one quasi-reversible redox wave was observed for reduction process at $E_{1/2}$ = –1.48 in THF (Figure 2-12b). Its reduction potential in THF was slightly lower than that of **3** (–1.37 V vs Fc/Fc^+),[8] indicating similar electron-accepting abilities.

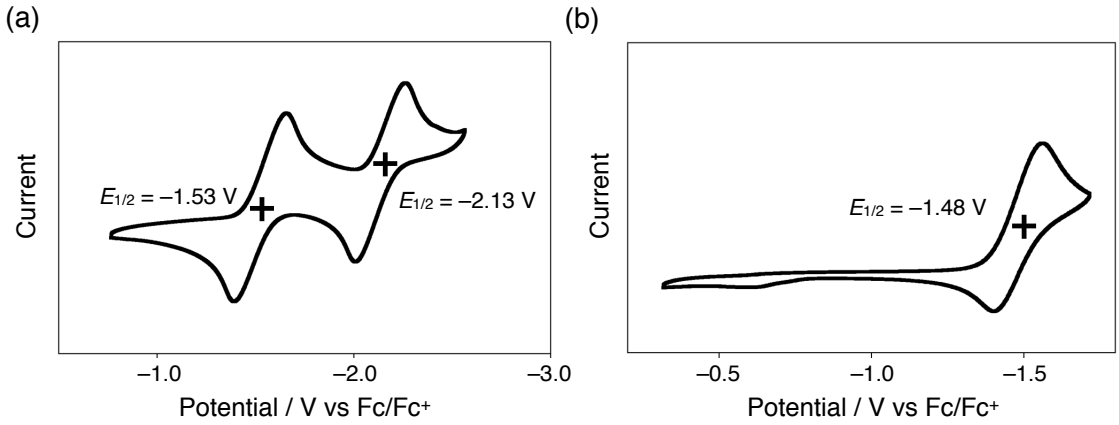

Figure 2-12. Cyclic voltammogram of **1** (a) in *o*-dichlorobenzene and (b) in THF (1 mM), measured with *n*-Bu_4NPF_6 as supporting electrolyte at a scan rate of 100 mV s^{-1}. Reprinted with permission from [19]. Copyright © 2014, American Chemical Society.

Theoretical calculations

To elucidate the electronic structure of **1**, DFT (B3LYP/6-31G*) calculation was conducted (Figure 2-13). The optimized geometry of π-skeleton showed good agreement with the crystal structures of **7** and **8**. The larger C1''–B''–C3'' bond angle of 128.0° and elongated B–C bond lengths of 1.552, 1.570, and 1.587 Å for B''–C1'', B''–C2'', and B''–C3'' bonds, respectively. Since the molecule consists of only carbon and boron atoms, the dipole moment was estimated to be small (1.3 D). The HOMO is mainly localized on the benzofluoranthene moiety, while the LUMO is delocalized over the entire molecule with a large contribution from the p orbital of the boron atom. The LUMO level of **1** (–2.63 eV) is comparable to that of **3** (–2.56 eV).[8] This result is consistent with the CV measurement. The TD-DFT calculation at the same level of theory suggested that the longest absorption band was assignable to the HOMO→LUMO transition. Its calculated transition energy of 2.26 eV (548 nm) and small oscillator strength of 0.0310 showed good agreement with the experimental absorption spectra of **1**. According to this result, moderate fluorescence quantum yield of **1** despite the rigid structure is probably due to the small radiative decay rate constant, which results from the small oscillator strength.

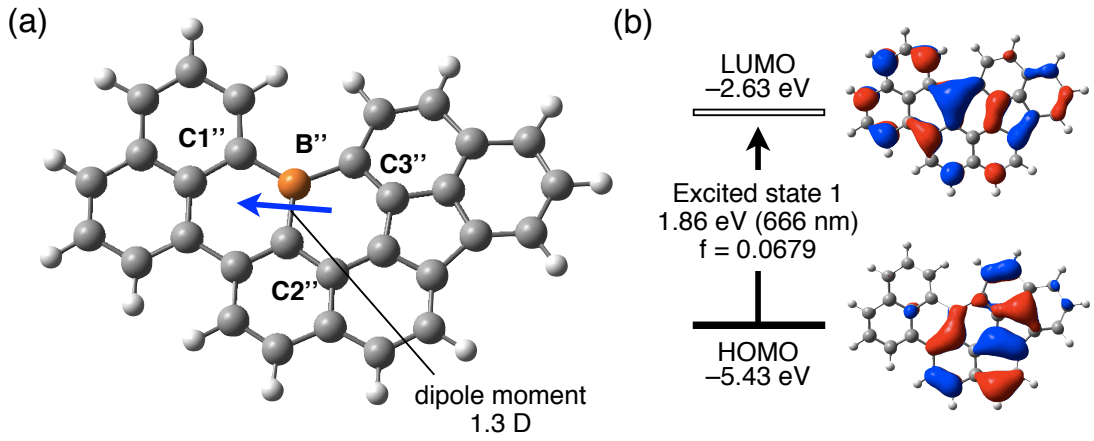

Figure 2-13. (a) The optimized structure of **1** and (b) Kohn-Sham molecular orbitals and lowest energy electronic transition of **1** at the B3LYP/6-31G* level of theory. Reprinted with permission from [19]. Copyright © 2014, American Chemical Society.

Lewis acidity

The author confirmed whether the elongated B–C bond lengths are relevant to the degree of its Lewis acidity. Upon addition of an excess of pyridine, the broad ^{11}B NMR signal of **1** at δ = 46.8 ppm in chlorobenzene-d_5 completely disappeared. Concomitantly, a sharp signal emerged at δ = –3.2 ppm, which was assigned to the **1**·pyridine adduct.[11] The single crystals of the adduct suitable for X-ray diffraction analysis were obtained from vapor diffusion of heptane into a toluene/pyridine solution of **1** (Figure 2-14). The asymmetric unit of these crystals contains two crystallographically independent molecules, both of which adopt a shallow bowl-shaped structure. The sum of the three C–B–C bond angles are 340.5° and 342.2°. The most notable feature in these molecules is the long B–N distance of 1.6927(17), and 1.6939(16) Å. These values are significantly higher than those in a sterically hindered dibenzoborole·pyridine adduct [1.638(4) Å],[12] a pentaphenylborole·2,6-lutidine adduct [1.6567(3) Å],[4] and a frustrated Lewis pair between $B(C_6F_5)_3$ and 2,6-lutidine [1.661(2) Å],[13] all of which dissociate in solution at room temperature. This comparison suggests a rather weak B–N coordinate bond in **1**·pyridine.

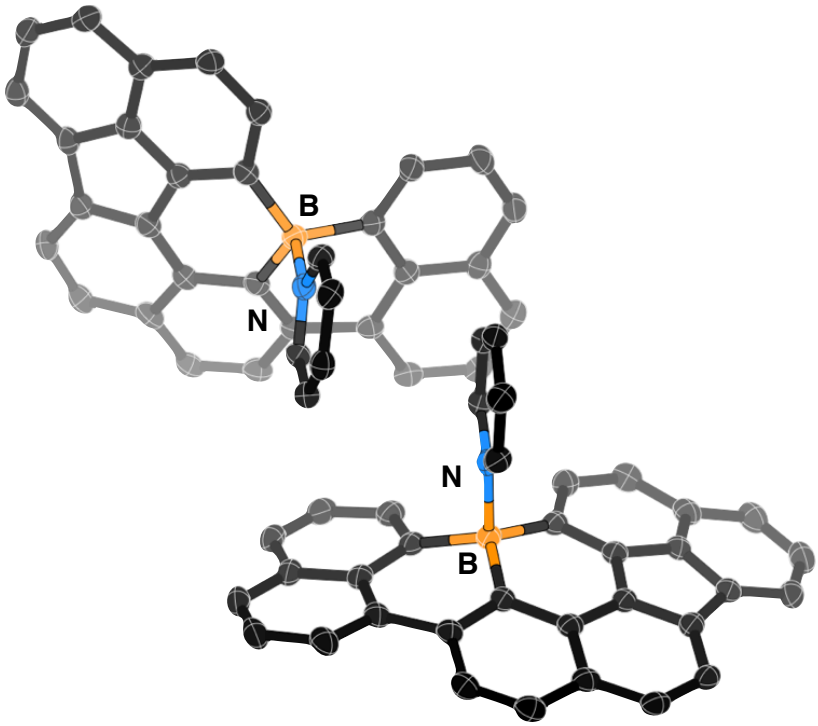

Figure 2-14. Crystal structure of **1**·pyridine (50% probability of thermal ellipsoids, hydrogen atoms are omitted for clarity). Reprinted with permission from [19]. Copyright © 2014, American Chemical Society.

Despite the weak B–N coordination, the Lewis acidity of **1** is still higher than those of the previously reported structurally constrained triarylboranes. This fact was demonstrated by a titration experiment of **1** with pyridine monitored by UV-Vis absorption spectroscopy (Figure 2-15a). Upon addition of pyridine, absorption bands of **1** at 546 nm and 429 nm gradually decreased, and new bands emerged at 346 and 374 nm, with a broad tail up to 490 nm. Isosbestic points were found at 390 and 309 nm. The significant hypsochromic shifts of the absorption maxima are due to the disruption of the π-conjugation through the p orbital at the boron atom by the coordination of pyridine. Notably, the absorption bands of **1** ($[\mathbf{1}]_0 = 3.4 \times 10^{-5}$ M) beyond 500 nm completely disappeared after the addition of pyridine up to $[\text{pyridine}]_0 = 4.2 \times 10^{-2}$ M. This is, in contrast to fully constrained **2**[7] and **3**[8], indicative of a quantitative formation of the **1**·pyridine adduct under the applied conditions. The binding constant (K) of **1** towards pyridine in toluene at 25 °C was established to be 5.09 (± 0.03) × 10^3 M^{-1} (Figure 2-15b), which is much higher than that of **3** (0.35 M^{-1} in THF).[7] The higher Lewis acidity of **1** relative to **3** should be attributed to the structural difference arising from the smaller constraint in **1**, because the electron-accepting character of **1** is comparable to that of **3** according to the CV measurement and DFT calculation. As partially fused compound **1** can be regarded as a model of the boron site at the edge position of boron-doped graphene,

while completely fused compound **3** is a model of internal boron site, this result demonstrated the potential relationship between the chemical adsorption properties and the geometry around Lewis acidic sites in boron-doped graphene.

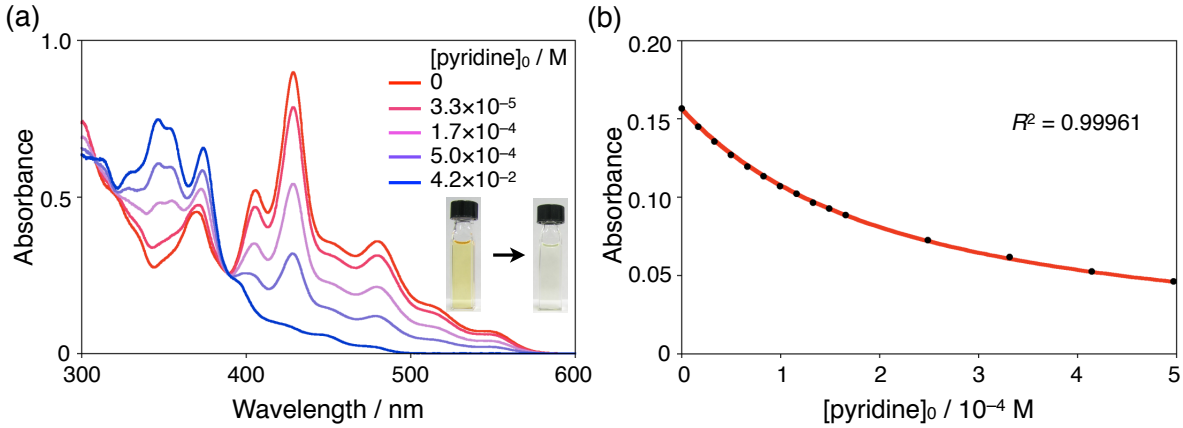

Figure 2-15. (a) UV-Vis absorption spectral change upon addition of pyridine to a toluene solution of **1** ($[\mathbf{1}]_0 = 3.4 \times 10^{-5}$ M) and (b) UV-Vis absorption titration plot of the absorbance at 510 nm (black dots) and the fitting curve for the binding constant of **1** toward pyridine (red line). Reprinted with permission from [19]. Copyright © 2014, American Chemical Society.

The titration experiments of a toluene solution of **1** with pyridine were also performed by fluorescence spectroscopy, which displayed an unexpected phenomenon (Figure 2-16a). Upon the addition of pyridine, a new band for **1**·pyridine appeared at 500 nm, while the original emission band gradually decreased. This is consistent with the corresponding spectral change in the UV-Vis absorption. However, the longer-wavelength emission band essentially remained present and only slightly decreased in intensity even after an excess of pyridine was added, which resulted in a complete disappearance of the absorption band associated with **1**. The excitation spectra monitored for the shorter- (λ_{em} = 490 nm) and longer-wavelength (λ_{em} = 570 nm) emission bands were identical to each other, as well as to the absorption spectrum of **1**·pyridine (Figure 2-16b). Consequently, both the fluorescence bands should arise from the photoexcitation of **1**·pyridine. In other words, the Lewis acid–base adduct **1**·pyridine exhibits dual fluorescence.

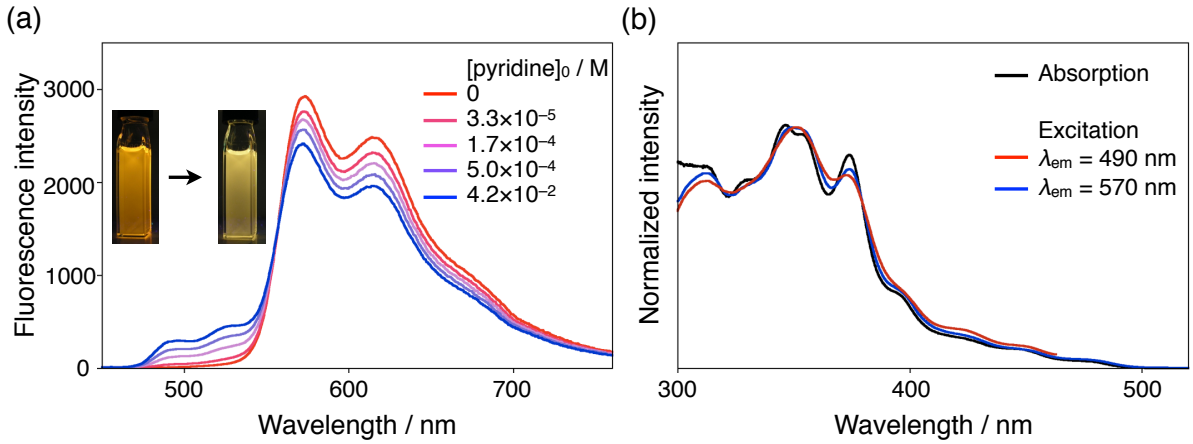

Figure 2-16. (a) Fluorescence spectral change upon addition of pyridine to a toluene solution of **1** ($[\mathbf{1}]_0 = 3.4 \times 10^{-5}$ M, $\lambda_{ex} = 390$ nm) and (b) absorption spectrum (black) and excitation spectrum with the fluorescence detection at 490 nm (red) and 570 nm (blue) of a toluene solution of **1**·pyridine ($[\mathbf{1}]_0 = 3.4 \times 10^{-5}$ M, $[\text{pyridine}]_0 = 4.2 \times 10^{-2}$ M). Reprinted with permission from [19]. Copyright © 2014, American Chemical Society.

Therefore, time-resolved fluorescence spectra of a toluene solution of **1**·pyridine were measured with excitation at 377 nm (Figure 2-17a). Immediately after the excitation, the first emission band appeared around 500 nm and subsequently the longer-wavelength emission emerged. The fluorescence lifetime values for the two emission bands in the region of 470–510 and 560–660 nm were determined to be 2.3 and 11.0 ns (Figure 2-17b), respectively, the latter of which is comparable to that of uncoordinated **1**. These results can be rationalized by considering the photodissociation of **1**·pyridine in the lowest singlet excited state (S_1; Figure 2-18). While the shorter-wavelength fluorescence arises from the locally excited state of **1**·pyridine, the photodissociation occurring in S_1 generates uncoordinated borane **1**, which is responsible for the longer-wavelength fluorescence emission. In the ground state, **1** immediately reproduces the Lewis acid–base adduct in the presence of an excess of pyridine. Similar fluorescence properties have been reported for 9-phenylxanthen-9-ol, which undergoes photodehydroxylation under concomitant emission of dual fluorescence from the excited alcohol and the photodissociated carbenium ion (Figure 2-19).[14] Thus, it is the isoelectronic relationship between the carbenium ion and the tricoordinate borane, which determines the similar behavior in the excited state.

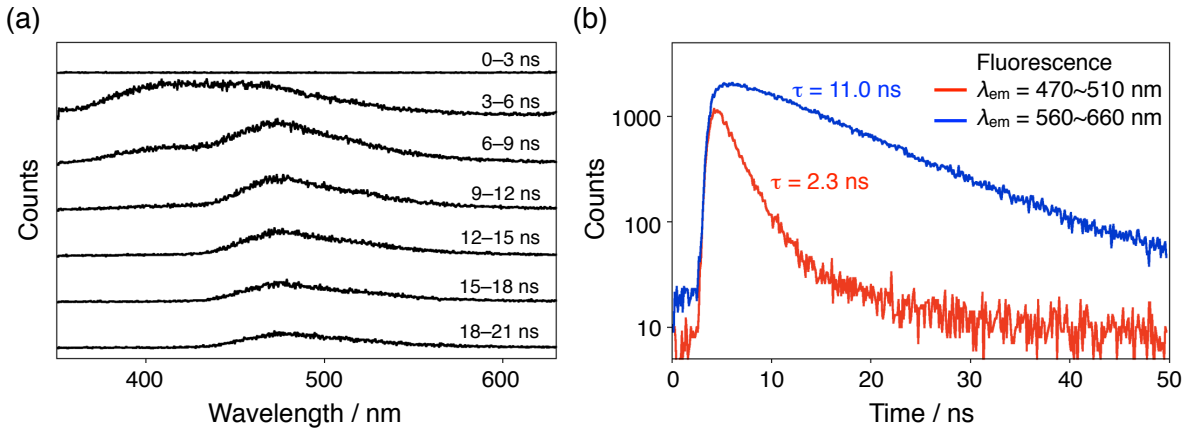

Figure 2-17. (a) Time-resolved fluorescence spectra and (b) fluorescence decay profiles and lifetimes at the different ranges of fluorescence wavelengths of **1**·pyridine in toluene with the excitation at 377 nm ($[\mathbf{1}]_0$ = 1.0 × 10^{-5} M, $[\text{pyridine}]_0$ = 8.3 × 10^{-2} M). Reprinted with permission from [19]. Copyright © 2014, American Chemical Society.

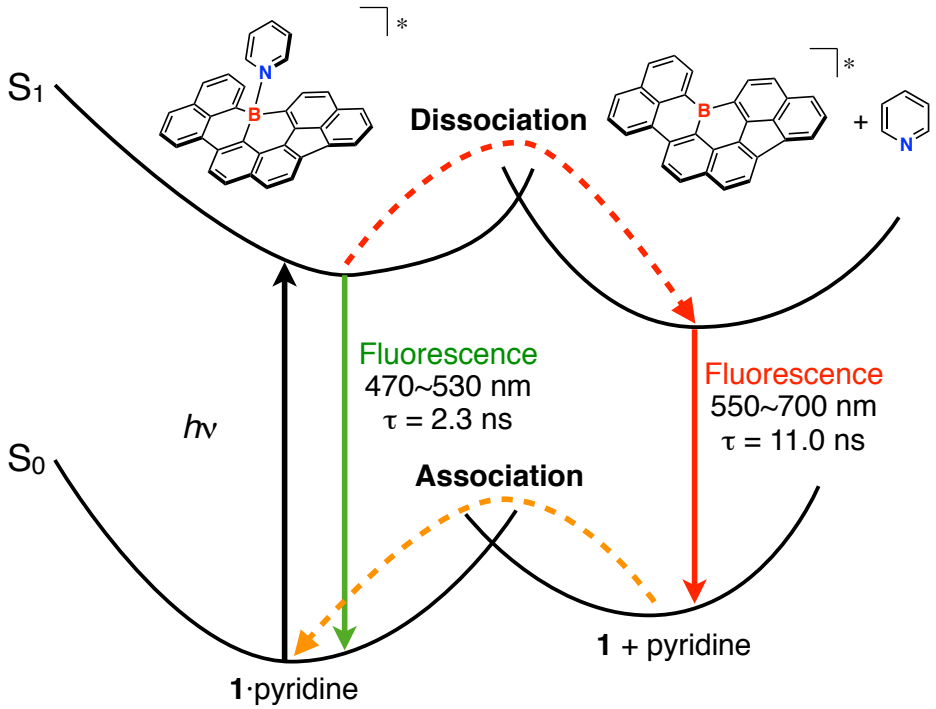

Figure 2-18. A plausible energy diagram for the photodissociation of **1**·pyridine. Reprinted with permission from [19]. Copyright © 2014, American Chemical Society.

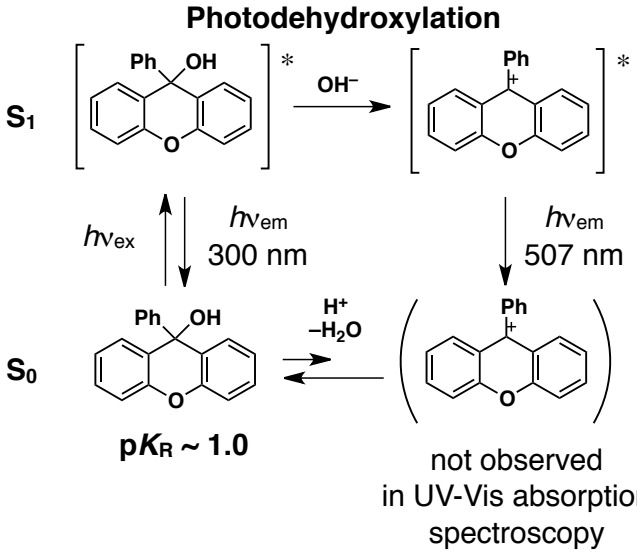

Figure 2-19. Photodehydroxylation of 9-phenylxanthen-9-ol in neutral aqueous solution.

To gain a deeper understanding of the excited-state behavior of **1**·pyridine, temperature- and solvent-dependent fluorescence spectra were measured under the conditions that uncoordinated **1** was not observed in absorption spectra. As the temperature decreased from 292 to 193 K, the shorter-wavelength emission band increased, while the one at longer wavelength decreased (Figure 2-20). The photodissociation is hence suppressed at low temperature, indicative of the presence of an activation barrier in S_1 for the photodissociation process. On the other hand, with increasing solvent polarity, the relative intensity of the shorter-wavelength emission band increased, whereas the absorption spectra showed only a subtle solvent dependence (Figure 2-21). These results demonstrate that the solvent polarity significantly affects the excited state, and that the photodissociation becomes more unfavorable in polar solvents.

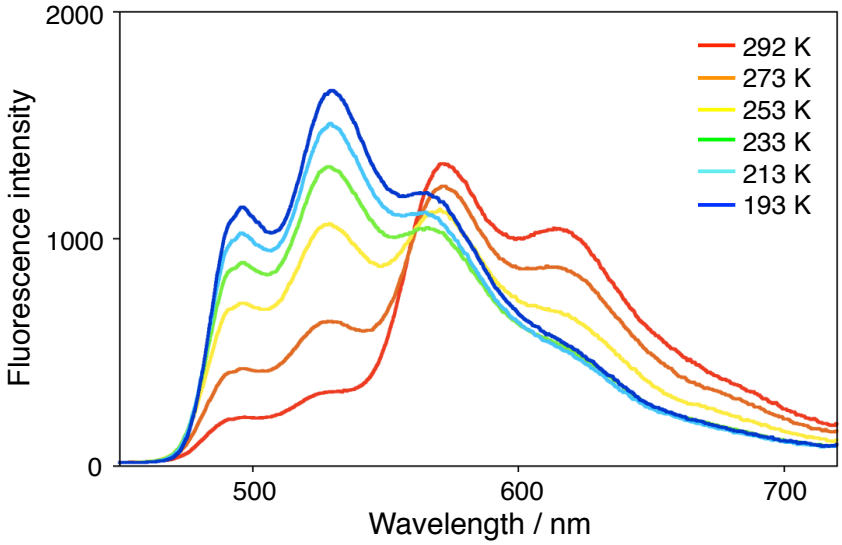

Figure 2-20. Fluorescence spectra of **1**·pyridine with the excitation at 370 nm in toluene at varied temperature ($[\mathbf{1}]_0$ = 3.0 × 10^{-6} M, $[\text{pyridine}]_0$ = 3.0 × 10^{-2} M). Reprinted with permission from [19]. Copyright © 2014, American Chemical Society.

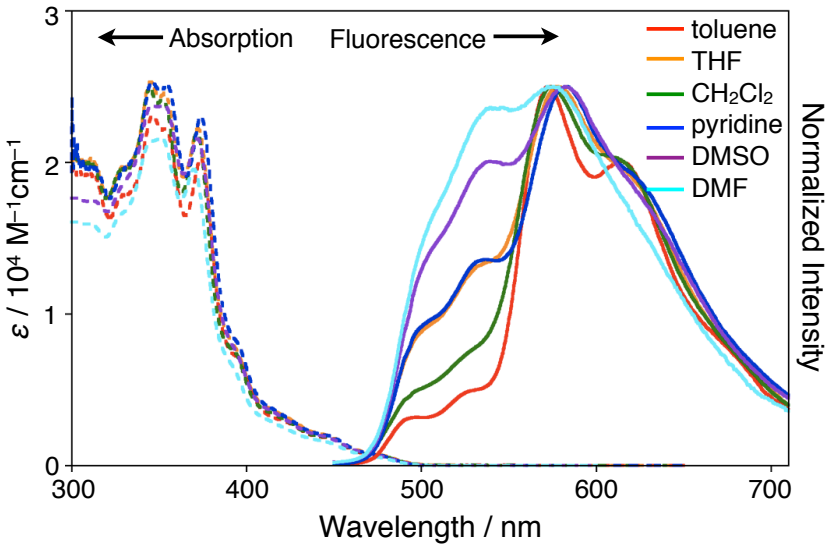

Figure 2-21. UV-Vis absorption (dashed line, $[\mathbf{1}]_0$ = 3.0 × 10^{-5} M, $[\text{pyridine}]_0$ = 4 × 10^{-2} M except for the pyridine solution) and fluorescence (solid line, $[\mathbf{1}]_0$ = 3.0 × 10^{-5} M, $[\text{pyridine}]_0$ = 3 × 10^{-2} M except for the pyridine solution) spectra with the excitation at 370 nm of **1**·pyridine in various solvents. Reprinted with permission from [19]. Copyright © 2014, American Chemical Society.

DFT calculations of **1**·pyridine were conducted at the B3LYP/6-31G* level to investigate its electronic feature. In the optimized structure, the B–N bond length was 1.737 Å and **1**·pyridine has a larger dipole moment of 6.6 D almost along the B–N bond than

non-coordinated **1** (Figure 2-22). The HOMO of **1**·pyridine is mainly localized on the benzofluoranthene moiety similar to non-coordinated **1**. On the other hand, LUMO is localized on the pyridine moieties, while LUMO+1 is delocalized over three naphthalene moieties. According to the TD-DFT calculations at the same level of theory, the lowest energy transition was mainly assigned to the HOMO→LUMO transition with very small oscillator strength of 0.0028, indicating the intramolecular charge transfer character from the benzofluoranthene moiety into the pyridine moiety in S_1. In addition, structural optimizations in the S_1 state were carried out based on the TD-DFT calculations (B3LYP/6-31G*) of **1** and **1**·pyridine (Figure 2-23). The dipole moments in the optimized structures in S_1 were 1.5 D and 7.8 D for **1** and **1**·pyridine, respectively. Therefore, during the photodissociation process, nondissociated Lewis acid–base adduct is stabilized to a greater extent in polar solvents in S_1, relative to the dissociated borane species, resulting in a suppression of the dissociation. Interestingly, the optimized structure of **1**·pyridine in S_1 displayed a much shorter B–N bond (1.592 Å) compared to the ground state. This structural feature should imply that obtained optimized structure is local minimum, where the shorter-wavelength fluorescence arises, and that the presence of an activation barrier in S_1 for the photodissociation process as indicated in plausible energy diagram. How the borane–pyridine Lewis acid–base adducts actually undergo the photodissociation still remains to be determined.

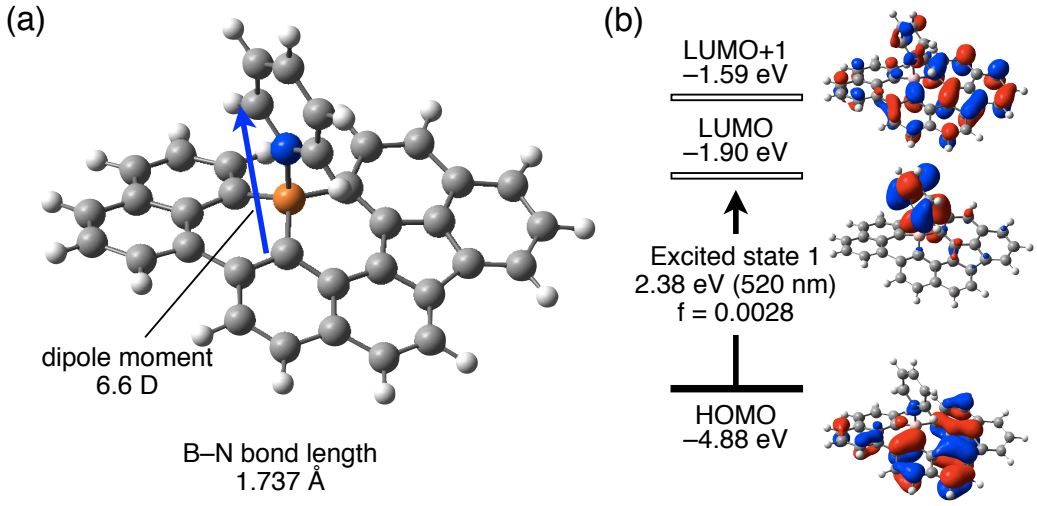

Figure 2-22. (a) The optimized structure of **1**·pyridine and (b) Kohn-Sham molecular orbitals and lowest energy electronic transition of **1**·pyridine at the B3LYP/6-31G* level of theory. Reprinted with permission from [19]. Copyright © 2014, American Chemical Society.

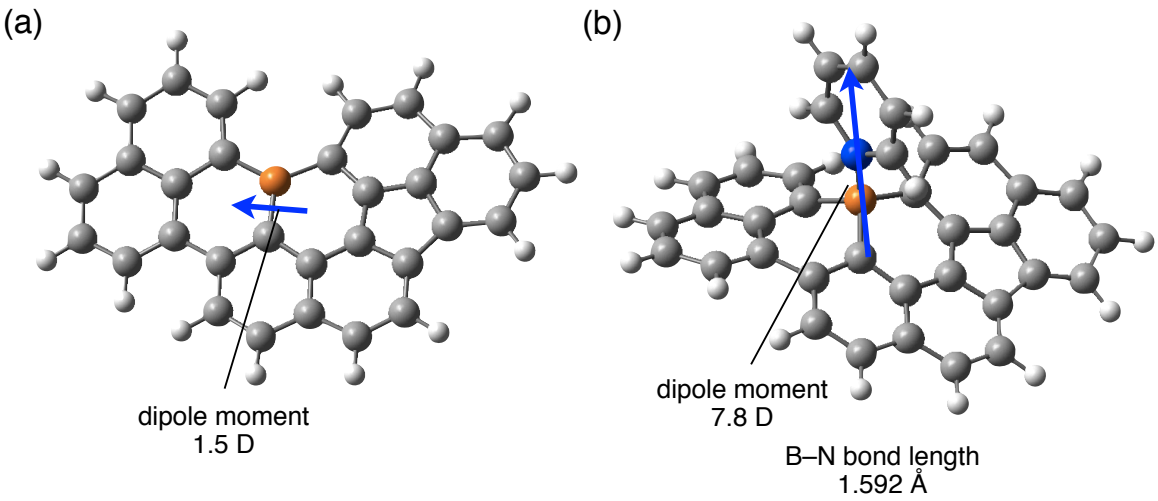

Figure 2-23. The optimized structures of (a) **1** and (b) **1**·pyridine in the S_1 excited state at the B3LYP/6-31G* level of theory. Reprinted with permission from [19]. Copyright © 2014, American Chemical Society.

Moreover, titration experiments of toluene solutions of **1** were conducted with various other Lewis bases. Initially, more Lewis basic *N,N*-dimethyl-4-aminopyridine (DMAP) was employed. On the basis of UV-Vis spectroscopic titrations, the binding constant (*K*) of **1** with DMAP was estimated to be 6.6 (± 1.3) × 10^6 M^{-1} (Figure 2-24). More importantly, any photodissociation was not observed in the fluorescence spectra (Figure 2-25). Upon addition of DMAP to a toluene solution of **1**, both the absorption and fluorescence spectra were found to change proportionally to the amount of DMAP added. Ultimately, only one green emission band was observed at 527 nm, which was attributed to **1**·DMAP. Then, 3-fluoropyridine (FPy) was used as weaker Lewis base. The binding constant of **1** towards FPy was determined to be 1.61 (± 0.02) × 10^2 M^{-1} (Figure 2-26). In sharp contrast, the use of the weaker Lewis basic FPy resulted in an almost unchanged fluorescence spectrum of **1**, even when an excess of FPy was added after the absorption band of **1** had completely changed into a new band of the **1**·FPy adduct (Figure 2-27). These results demonstrate that the photodissociation behavior of these systems strongly depends on the Lewis basicity of the additive. The observed dual emission of **1**·pyridine is based on the delicate balance between the Lewis acidity of **1** and the Lewis basicity of the pyridine derivatives.

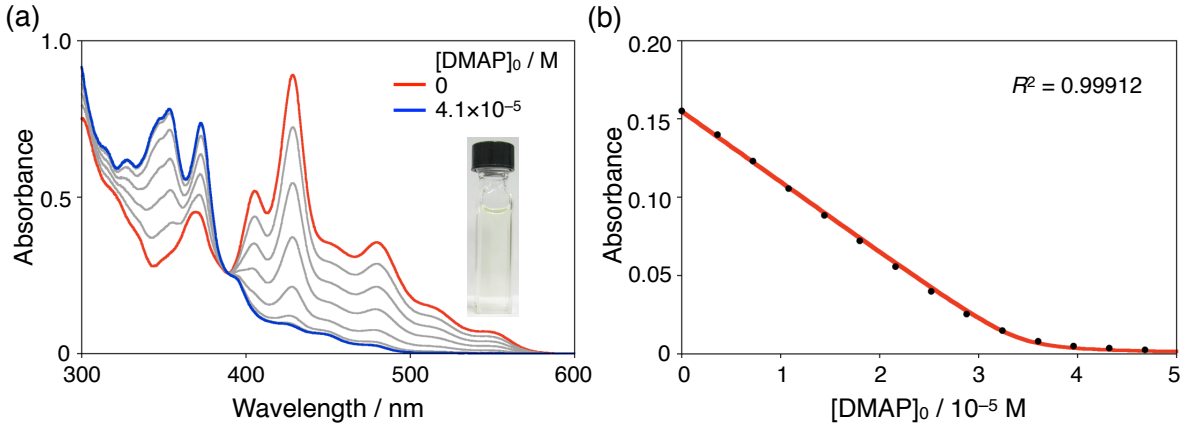

Figure 2-24. (a) UV-Vis absorption spectral change upon addition of DMAP to a toluene solution of **1** ($[\mathbf{1}]_0 = 3.4 \times 10^{-5}$ M) and (b) UV-Vis absorption titration plot of the absorbance at 510 nm (black dots) and the fitting curve for the binding constant of **1** toward DMAP (red line). Reprinted with permission from [19]. Copyright © 2014, American Chemical Society.

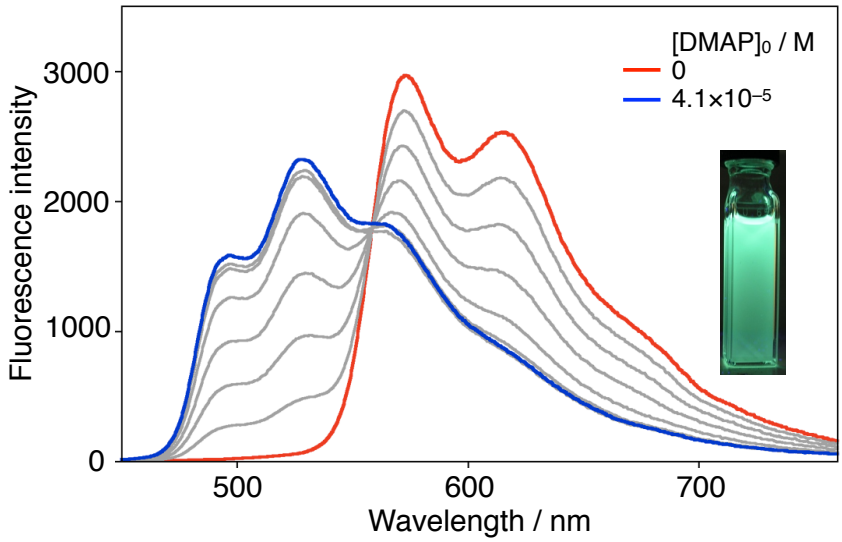

Figure 2-25. Fluorescence spectral change upon addition of DMAP to a toluene solution of **1** ($[\mathbf{1}]_0 = 3.4 \times 10^{-5}$ M, $\lambda_{ex} = 390$ nm). Reprinted with permission from [19]. Copyright © 2014, American Chemical Society.

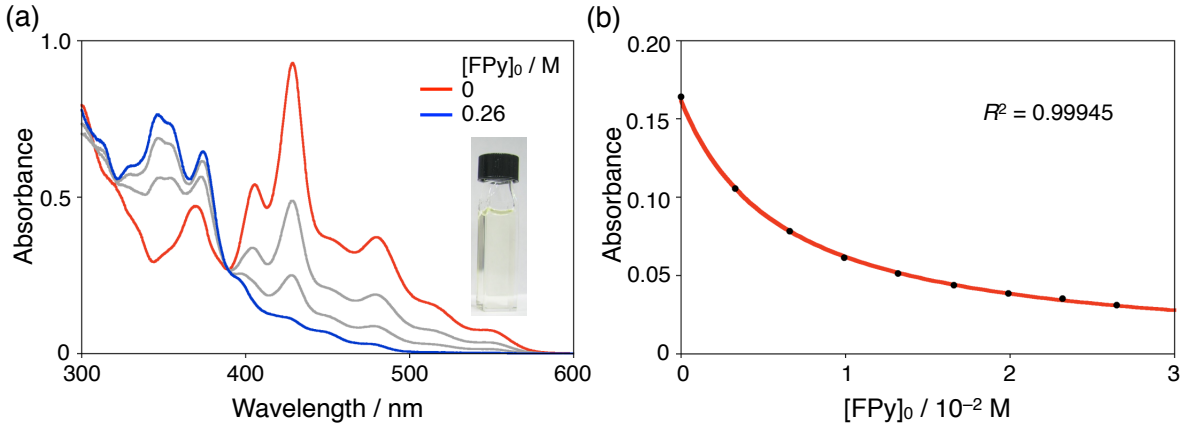

Figure 2-26. (a) UV-Vis absorption spectral change upon addition of 3-fluoropyridine to a toluene solution of **1** ($[\mathbf{1}]_0$ = 3.5 × 10^{-5} M) and (b) UV-Vis absorption titration plot of the absorbance at 510 nm (black dots) and the fitting curve for the binding constant of **1** toward 3-fluoropyridine (red line). Reprinted with permission from [19]. Copyright © 2014, American Chemical Society.

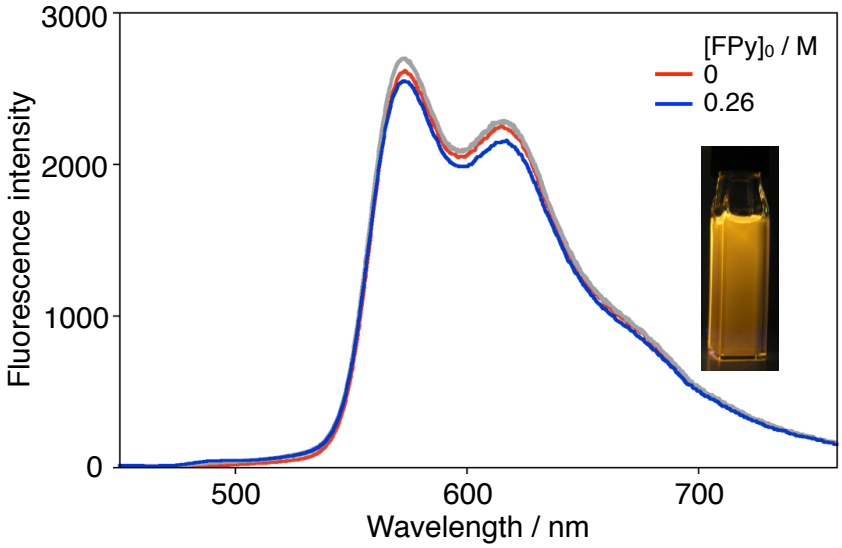

Figure 2-27. Fluorescence spectral change upon addition of 3-fluoropyridine to a toluene solution of **1** ($[\mathbf{1}]_0$ = 3.5 × 10^{-5} M, λ_{ex} = 390 nm). Reprinted with permission from [19]. Copyright © 2014, American Chemical Society.

2-3. Conclusion

The author has synthesized a partially fused trinaphthylborane **1**. The small structural constraint imparts high Lewis acidity to the planarized triarylborane skeleton, while the remarkable stability toward water and oxygen is maintained. Consequently, the molecule can easily form Lewis acid–base adducts in solution, even with weakly Lewis basic pyridine derivatives. Importantly, these B–N Lewis acid–base adducts undergo unprecedented photodissociation in the excited state, resulting in a dual emission that covers a broad range of the visible light (480–700 nm). The photoinduced B–N bond cleavage and the regeneration of the highly stable boron-embedded π systems should have great potential as a basis for various functions, such as photochromism, organocatalysis, and photoresponsive supramolecular assembly.[15]

2-4. Experimental section

General

Melting points (mp) were determined with a Yanaco MP-S3 instrument. ^{1}H, ^{13}C, and ^{11}B NMR spectra were measured with a JEOL AL-400, A-400 (400 MHz for ^{1}H, 100 MHz for ^{13}C, and 128 MHz for ^{11}B), or A-600 (600 MHz for ^{1}H, and 192 MHz for ^{11}B) spectrometer. Chemical shifts are reported in δ ppm with reference to residual protons of $CDCl_3$ (7.26 ppm in ^{1}H NMR), C_6D_6 (7.16 ppm in ^{1}H NMR), chlorobenzene-d_5 (7.14 ppm in ^{1}H NMR), and pyridine-d_5 (7.58 ppm in ^{1}H NMR and 135.91 ppm in ^{13}C NMR). $BF_3{\cdot}OEt_2$ was used as an external standard in ^{11}B NMR spectra. Mass spectra were measured with a Bruker micrOTOF Focus using the APCI-TOF method in the positive ion mode in toluene. Single crystal X-ray diffraction measurements were performed with a Rigaku X-ray diffractometer equipped with a copper MicroMax-007 microfocus generator, VariMax-Cu optics, and a RAPID IP detector. The structures were solved by the direct method (SHELXL-97[16]) and refined by the full-matrix least-squares on F^2 (SHELXL-97[16]). All non-hydrogen atoms were refined anisotropically. Thin layer chromatography (TLC) was performed on the plates coated with 0.25 mm thickness of Silica Gel 60 F-254 (Merck). Column chromatography was performed using neutral silica gel PSQ 60B (Fuji Silysia Chemical). Thermogravimetric analysis (TGA) was performed using Seiko TGA6200 at a heating rate of 5 °C min^{-1} under a nitrogen atmosphere. UV-vis absorption spectra were measured with a Shimadzu UV-3150, or UV-3600 spectrometer. Fluorescence spectra were measured with a Hitachi F-4500 spectrometer. Absolute fluorescence quantum yields (F) were determined with a Hamamatsu C9920-02 calibrated integrating sphere. Time-resolved fluorescence spectra were measured with a Hamamatsu picosecond fluorescence measurement system C4780. Cyclic voltammetry (CV) was performed on an Als/chi-617A electrochemical analyzer. The CV cell consisted of a glassy carbon electrode, a Pt wire counter electrode, and a $Ag/AgNO_3$ reference electrode. The measurements were carried out with a scan rate of 100 mV s^{-1} under an argon atmosphere using an *o*-dichlorobenzene or a THF solution of sample with a concentration of 1 mM. Tetrabutylammonium hexafluorophosphate (n-Bu_4NPF_6) was used as a supporting electrolyte. The redox potentials were calibrated with ferrocene as an internal standard. All reactions were performed under a nitrogen atmosphere, unless otherwise stated. Commercially available solvents and reagents were used without further purification unless otherwise mentioned. Dry ether and toluene were purchased from Kanto Chemical. $BF_3{\cdot}OEt_2$ was distilled in the presence of CaH_2 before use. $(TMS)_3SiH$ (stabilized with TBBP) was purchased from Tokyo Chemical Industry. 1,8-Diiodonaphthalene **8** was prepared according to the literature.[17]

Synthesis

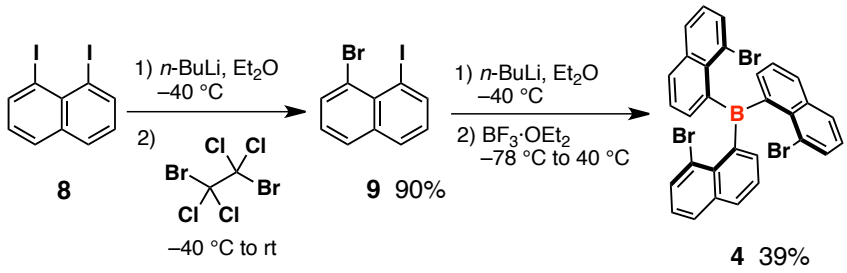

8-Bromo-1-iodonaphthalene (9). To a solution of **8** (22.1 g, 58.1 mmol) in dry ether (500 mL) cooled at –40 °C was added *n*-BuLi (1.65 M in hexane, 35.3 mL, 58.1 mmol) dropwise. After the reaction mixture was stirred at the same temperature for 1 h, a solution of tetrachlorodibromoethane (19.5 g, 58.1 mmol) in dry ether (60 mL) was added to the mixture dropwise. The reaction mixture was gradually warmed to room temperature. After addition of an aqueous Na_2SO_3 solution, the organic layer was separated. The aqueous layer was extracted with ether. The combined organic layer was washed with water and brine, dried over anhydrous Na_2SO_4, and concentrated under reduced pressure. The resulting mixture was passed through a short silica gel column (PSQ 60B, toluene) and recrystallized from a hexane/AcOEt solution to afford 17.4 g (52.4 mmol, 90% yield) of **9** as a brownish yellow solid. Mp: 98–99 °C (Lit.[3] 98–100 °C). ^{1}H NMR (400 MHz, C_6D_6) δ 6.46 (dd, J = 8.0 Hz, 7.6 Hz, 1H), 6.64 (dd, J = 8.0 Hz, 7.6 Hz, 1H), 7.20–7.25 (m, 2H), 7.64 (ddd, J = 7.5 Hz, 2.5 Hz, 1.3 Hz, 1H), 8.16 (ddd, J = 7.3 Hz, 4.5 Hz, 1.4 Hz, 1H). HRMS (APCI, positive): calcd for $C_{10}H_6BrI$: 331.8692 (M^+), found 331.8699.

Tris(8-bromo1-naphthyl)borane (4). To a solution of **9** (2.73 g, 8.21 mmol) in dry ether (82 mL) cooled at –78 °C was added *n*-BuLi (1.61 M, 5.10 mL, 8.21 mmol) dropwise. After the mixture was stirred at the same temperature for 30 min, BF_3·OEt_2 (335 mL, 2.71 mmol) was added. The reaction mixture was warmed to 40 °C and stirred for 2 h. After cooling to the room temperature, dry hexane (60 mL) was added. Inorganic salts were removed by filtration and the filtrate was concentrated under reduced pressure. The resulting mixture was passed through a short silica gel column (PSQ 60B, toluene). After removal of the solvents by evaporation, the resulting solid was washed with hexane and AcOEt to afford 659 mg (1.05 mmol, 39% yield) of pure **4** as a pale yellow solid. Mp: 277–282 °C. ^{1}H NMR (400 MHz, $CDCl_3$, 25 °C): δ 6.58 (d, J = 7.2 Hz, 3H), 7.07 (dd, J = 8.0 Hz, 7.2 Hz, 3H), 7.31 (dd, J = 8.0 Hz, 7.2 Hz, 3H), 7.78 (d, J = 7.2 Hz, 3H), 7.82, (d, J = 8.0 Hz, 3H), 7.87 (d, J = 8.0 Hz, 3H). Variable temperature ^{1}H NMR analysis of **4** demonstrated that the spectrum was largely

dependent on the measurement temperature due to the hindered rotation of the naphthyl groups. A clear ^{13}C NMR spectrum was not obtained due to this reason. ^{11}B NMR (128 MHz, $CDCl_3$): δ 61.3. HRMS (APCI, positive): calcd for $C_{30}H_{18}BBr_3$: 625.9046 (M^+), found 625.9047.

A partially fused trinaphthylborane 1. To a solution of **4** (1.01 g, 1.60 mmol) and 1,1′-azobis(cyclohexanecarbonitrile) (ABCN, 977 mg, 4.00 mmol) in dry toluene was added tris(trimethylsilyl)silane (2.73 mL, 8.00 mmol). The mixture was heated at 120 °C for 17 h. After cooling to room temperature, red precipitates were collected by filtration and washed with toluene and hexane. The insoluble mixture was recrystallized from hot chlorobenzene to afford 161 mg (0.418 mmol, 26% yield) of **1** as a red solid. Mp: 298–299 °C (decomposed). ^1H NMR (400 MHz, chlorobenzene-d_5, 120 °C): δ 7.52 (d, J = 8.0 Hz, 1H), 7.59 (m, 2H), 7.69 (m, 2H), 7.76 (m, 2H), 7.93 (m, 2H), 8.12 (d, J = 8.0 Hz, 1H), 8.34 (d, J = 8.0 Hz, 1H), 8.67 (d, J = 8.0 Hz, 2H), 9.47 (d, J = 6.8 Hz, 1H). ^{13}C NMR was not obtained due to its poor solubility. ^{11}B NMR (128 MHz, chlorobenzene-d_5, 120 °C): δ 46.8. HRMS (APCI, positive): calcd for $C_{30}H_{15}B$: 386.1261 (M^+), found 386.1265.

Brominated fused trinaphthylborane 6. A solution of **1** (31.2 mg, 80.8 mmol) and *N*-bromosuccinimide (15.0 mg, 82.6 mmol) in chlorobenzene (8 mL) was heated at 120 °C for 16 h. After cooling to room temperature, hexane was added to the reaction mixture. The precipitates were collected by filtration and washed with hexane. The mixture was recrystallized from hot *o*-dichlorobenzene to afford 30.0 mg (64.5 mmol, 80% yield) of **6** as a brownish red solid. Mp: >300 °C. ^1H NMR (400 MHz, chlorobenzene-d_5, 120 °C): δ 7.31 (dd, J = 8.0 Hz, 6.8 Hz , 1H), 7.55 (m, 2H), 7.63 (dd, J = 8.4 Hz, 6.8 Hz, 2H), 7.75 (m, 2H), 7.98 (d, J = 8.4 Hz 1H), 8.08 (s, 1H), 8.16 (d, J = 7.6 Hz, 1H), 8.34 (d, J = 8.0 Hz, 1H), 8.44 (d, J = 8.8 Hz, 1H), 8.71 (dd, J = 8.8 Hz, 7.6 Hz, 2H), 9.52 (d, J = 6.4 Hz, 1H). ^{13}C NMR and ^{11}B NMR were not obtained due to its poor solubility. HRMS (APCI, positive): calcd for $C_{30}H_{15}BBr$: 465.0445 [$(M+H)^+$], found 465.0445.

Phenylated fused trinaphthylborane 7. Compound **6** (29.7 mg, 63.9 mmol), phenylboronic acid (11.9 mg, 97.6 mmol), and $Pd(PPh_3)_4$ (3.7 mg, 3.2 mmol) were dissolved into a degassed aqueous Na_2CO_3 solution (2M, 1.5 mL), degassed toluene (3 mL) and degassed EtOH (0.5 mL). The mixture was heated at 90 °C for 8 h. After addition of water at room temperature, the organic layer was separated and the aqueous layer was extracted with toluene. The combined organic layer was washed with brine, dried over anhydrous Na_2SO_4, and

concentrated under reduced pressure. The resulting mixture was passed through a short silica gel column (PSQ 60B, $CHCl_3$) and recrystallized from a $CHCl_3$/hexane solution to afford 17.3 mg (37.4 mmol, 59% yield) of **6** as a brownish red solid. Mp: 285–289 °C (decomposed). ^{1}H NMR (400 MHz, $CDCl_3$): δ 7.50 (m, 2H), 7.59 (dd, J = 7.6 Hz, 6.8 Hz, 2H), 7.68 (m, 3H), 7.76–7.82 (m, 3H), 7.92 (m, 2H), 8.15 (m, 2H), 8.35 (d, J = 7.2 Hz, 1H), 8.48 (d, J = 9.6 Hz, 1H), 8.75 (d, J = 8.4 Hz, 1H), 8.86 (d, J = 7.6 Hz, 1H), 9.57 (d, J = 5.6 Hz, 1H). ^{13}C NMR was not obtained due to its poor solubility. ^{11}B NMR (128 MHz, $CDCl_3$): δ 47.0. HRMS (APCI, positive): calcd for $C_{36}H_{20}B$: 463.1653 [$(M+H)^+$], found 463.1658.

Lewis adduct of 1 with pyridine (1·pyridine). ^{1}H NMR (400 MHz, pyridine-d_5, 25 °C): δ 7.65 (m, 2H), 7.90 (m, 2H), 7.97–8.08 (m, 5H), 8.11 (d, J = 7.2 Hz, 1H), 8.19 (d, J = 8.4 Hz, 1H), 8.48 (d, J = 9.2 Hz, 1H), 8.53 (d, J = 7.2 Hz, 1H), 8.67 (d, J = 8.0 Hz, 1H), 9.18 (d, J = 7.2 Hz, 1H). ^{13}C NMR (100 MHz, pyridine-d_5, 25 °C): δ 122.1, 122.7, 122.9, 124.4, 125.5, 126.2, 126.4, 126.8, 127.0, 127.1, 127.3, 128.9, 128.9, 129.8, 130.7, 131.1, 131.7, 132.3, 132.6, 133.5, 133.7, 133.9, 134.9, 135.8, 139.1, 140.2, 141.0. Three signals for the carbon atoms bonding to the boron atom were not observed due to the quadrupolar relaxation of the boron atom. ^{11}B NMR (128 MHz, $CDCl_3$, 25 °C): δ –3.2, (128 MHz, pyridine-d_5, 25 °C): δ –2.8.

Lewis adduct of 1 with *N*,*N*-dimethyl-4-aminopyridine (1·DMAP). ^{1}H NMR (600 MHz, $CDCl_3$, 25 °C): δ 2.73 (broad, 6H), 5.95 (broad, 2H), 7.37 (broad, 2H), 7.56 (m, 2H), 7.69 (dd, J = 7.8 Hz, 6.6 Hz, 1H), 7.76 (d, J = 8.4 Hz, 1H), 7.79 (d, J = 8.4 Hz, 1H), 7.81 (d, J = 8.4 Hz, 1H), 7.87 (m, 3H), 7.96 (m, 2H), 8.20 (d, J = 9.0 Hz, 1H), 8.30 (d, J = 7.8 Hz, 1H), 8.36 (d, J = 7.8 Hz, 1H), 8.79 (d, J = 7.2 Hz, 1H). ^{11}B NMR (192 MHz, $CDCl_3$, 25 °C): δ –5.7.

Lewis adduct of 1 with 3-fluoropyridine (1·PyF). ^{11}B NMR (128 MHz, in 3-fluoropyridine, 25 °C): δ –2.9. Since the association constrant of 1 towards 3-fluoropyridine is small, we measured the NMR spectroscopy using 3-fluoropyridine as a solvent. Therefore, we were not able to measure the ^{1}H and ^{13}C NMR spectra.

X-ray crystallographic analysis

X-ray crystallographic analysis of 6. Red needle crystals of **6** were obtained by the recrystallization from *o*-dichlorobenzene and EtOH using a vapor diffusion method. The measurement was performed at 123 K. Total 20066 reflections were collected, among which

3509 reflections were independent (R_{int} = 0.0716). The crystal data are as follows: Formula $C_{30}H_{13.44}BBr_{1.56}$; FW = 509.59, crystal size 0.15 × 0.01 × 0.01 mm, monoclinic, *P*2/*a*, (#13), *a* = 23.4202(10), *b* = 3.8518(2), *c* = 23.7888(12) Å, β = 116.409(4)°, *V* = 1922.03(16) Å^3, *Z* = 4, D_{calcd} = 1.761 g cm^{-3}; R_1 = 0.0816 ($I > 2s(I)$), wR_2 = 0.2093 (all data), GOF = 1.091. The crystal structure was solved as a disordered crystal which consisted of monobrominated form **6** and dibrominated form because the sample solution contained a trace amount of dibrominated impurity. The ratio between **6** and dibromide in this crystal was calculated to be 56:44. Unfortunately, we have not succeeded in obtaining single crystals from pure samples, whereas the recrystallization from crude mixtures afforded the single crystals. The yield of **6** was carefully determined based on the isolated pure powder sample, whose purity was confirmed by 1H NMR spectroscopy. We used the pure sample of **5** for the next cross-coupling reaction, and were not able to detect any disubstituted product. The crystal data are deposited in The Cambridge Crystallographic Data Centre (CCDC 1010921).

X-ray crystallographic analysis of 7. Red block crystals of **7** were obtained by the recrystallization from AcOEt and EtOH using a vapor diffusion method. The measurement was performed at 123 K. Total 19537 reflections were collected, among which 4361 reflections were independent (R_{int} = 0.0584). The crystal data are as follows: Formula $C_{36}H_{19}B$; FW = 462.35, crystal size 0.17 × 0.10 × 0.03 mm, monoclinic, $P2_1/a$, (#14), *a* = 8.2116(7), *b* = 19.7752(15), *c* = 13.7250(17) Å, β = 90.723(4)°, *V* = 2228.6(4) Å^3, *Z* = 4, D_{calcd} = 1.378 g cm^{-3}; R_1 = 0.0499 ($I > 2s(I)$), wR_2 = 0.1205 (all data), GOF = 1.042.

X-ray crystallographic analysis of 1·pyridine. Yellow block crystals of **1**·pyridine were obtained by the recrystallization from toluene, pyridine and heptane using vapor diffusion method. The measurement was performed at 123 K. Total 42069 reflections were collected, among which 8025 reflections were independent (*R*int = 0.0229). The crystal data are as follows: Formula $C_{35}H_{20}BN$; FW = 465.33, crystal size 0.30 × 0.16 × 0.12 mm, triclinic, *P*–1, (#2), *a* = 13.2491(2), *b* = 13.6484(3), *c* = 13.7598(3) Å, *a* = 75.4215(7)°, β = 70.2656(7)°, *g* = 75.5401(7)°, *V* = 2229.27(8) Å^3, *Z* = 4, D_{calcd} = 1.386 g cm^{-3}; R_1 = 0.0373 ($I > 2s(I)$), wR_2 = 0.0987 (all data), GOF = 1.074. Two crystallographically independent molecules are contained in the unit cell, both of which adopt a shallow bowl-shaped structure. The depth of the bowl, which is defined as the distance between the boron atom and the mean plane consisting of the peripheral carbon atoms of the naphthyl groups, were measured to be 1.1 Å and 1.4 Å. The crystal data are deposited in The Cambridge Crystallographic Data Centre (CCDC 1010997).

Device fabrication and evaluation of FET performance

Organic field effect transistor (OFET) in a top-contact configuration was fabricated on a heavily doped n^+-Si (100) wafer with a 100 nm thermally grown SiO_2 (C_i = 34.5 nF cm^{-2}). The substrate surface was treated with hexamethyldisilazane (HMDS). A thin film (50 nm thick) of **1** as the active layer was vacuum-deposited on the Si/SiO_2 substrates maintained at room temperature at a rate of 0.5 Å s^{-1} under the pressure of 10^{-3} Pa. On top of the organic thin film, gold films (40 nm) were deposited as drain and source electrodes through a shadow mask. The drain-source channel length (L) and width (W) were 40 μm and 0.2 μm, respectively. Characteristics of the OFET devices were measured at room temperature under the pressure of 1.0×10^{-3} Pa with an Agilent Technologies B1500A semiconducting parameter analyzer. Field-effect mobility (μ_{FET}) was calculated in the saturation (V_d = –40 V and 40 V for the hole mobility m_h and the electron mobility m_e, respectively) regime of the I_d using the following equation,

$$I_d = (WC_i / 2L)\, \mu_{FET}\, (V_g - V_{th})^2$$

where C_i is the capacitance of the SiO_2 insulator, and V_g and V_{th} are the gate and threshold voltages, respectively.

Theoretical calculations

The geometry optimizations for **1** and **1**·pyridine in the ground state and the lowest singlet excited state (S_1) were performed using Gaussian 09 program[18] at the B3LYP/6-31G* level of theory. The optimized structure in the ground state was used as an initial structure for the geometry optimization in S_1. The time-dependent density functional theory (TD-DFT) calculations at the optimized geometry were conducted at the same level of theory.

References

(1) (a) Entwistle, C. D.; Marder, T. B. *Angew. Chem., Int. Ed.* **2002**, *41*, 2927. (b) Entwistle, C. D.; Marder, T. B. *Chem. Mater.* **2004**, *16*, 4574. (c) Yamaguchi, S.; Wakamiya, A. *Pure Appl. Chem.* **2006**, *78*, 1413. (d) Bosdet, M. J. D.; Piers, W. E. *Can. J. Chem.* **2008**, *86*, 8. (e) Jäkle, F. *Chem. Rev.* **2010**, *110*, 3985. (f) Hudson, Z. M.; Wang, S. *Dalton Trans.* **2011**, *40*, 7805.

(2) (a) Loudet, A.; Burgess, K. *Chem. Rev.* **2007**, *107*, 4891. (b) Ulrich, G.; Ziessel, R.; Harriman, A. *Angew. Chem. Int. Ed.* **2008**, *47*, 1184. (c) Rao, Y.-L.; Wang, S. *Inorg. Chem.* **2011**, *50*, 12263. (d) Frath, D.; Massue, J.; Ulrich, G.; Ziessel, R. *Angew. Chem. Int. Ed.* **2014**, *53*, 2290.

(3) (a) Rao, Y.-L.; Amarne, H.; Zhao, S.-B.; McCormick, T. M.; Martić, S.; Sun, Y.; Wang, R.-Y.; Wang, S. *J. Am. Chem. Soc.* **2008**, *130*, 12898. (b) Baik, C.; Hudson, Z. M.; Amarne, H.; Wang, S. *J. Am. Chem. Soc.* **2009**, *131*, 14549. (c) Rao, Y.-L.: Amarne, H.; Wang, S. *Coord. Chem. Rev.* **2012**, *256*, 759. (d) Rao, Y.-L.; Chen, L. D.; Mosey, N. J.; Wang, S. *J. Am. Chem. Soc.* **2012**, *134*, 11026. (e) Nagura, K.; Saito, S.; Fröhlich, R.; Glorius, F.; Yamaguchi, S. *Angew. Chem. Int. Ed.* **2012**, *51*, 7762. (f) Kropp, M.; Bhamidapaty, K.; Schuster, G. B. *J. Am. Chem. Soc.* **1988**, *110*, 6252.

(4) Ansorg, K.; Braunschweig, H.; Chiu, C.-W.; Engels, D.; Gamon, D.; Hügel, M.; Kupfer, T.; Radacki, K. *Angew. Chem. Int. Ed.* **2011**, *50*, 2833.

(5) Weiner, B. R.; Pasternack, L.; Nelson, H. H.; Prather, K. A.; Rosenfeld, R. N. *J. Phys. Chem.* **1990**, *94*, 4138.

(6) (a) Bertelson, R. C. In Photochromism; Brown, G. H., Ed.; Techniques of chemistry; Wiley-Interscience: New York, 1971; Vol. 3. (b) Das, P. K. *Chem. Rev.* **1993**, *93*, 119. (c) Duxbury, D. F. *Chem. Rev.* **1993**, *93*, 381.

(7) (a) Zhou, Z.; Wakamiya, A.; Kushida, T.; Yamaguchi, S. *J. Am. Chem. Soc.* **2012**, *134*, 4529. (b) Kushida, T.; Camacho, C.; Shuto, A.; Irle, S.; Muramatsu, M.; Katayama, T.; Ito, S.; Nagasawa, Y.; Miyasaka, H., Sakuda, E.; Kitamura, N.; Zhou, Z.; Wakamiya, A.; Yamaguchi, S. *Chem. Sci.* **2014**, *5*, 1296.

(8) Saito, S.; Matsuo, K.; Yamaguchi, S. *J. Am. Chem. Soc.* **2012**, *134*, 9130.

(9) (a) Baldwin, J. E. *J. Chem. Soc. Chem. Commun.* **1976**, *18*, 734. (b) Bowman, W. R.; Heaney, H.; Jordan, B. M. *Tetrahedron* **1991**, *47*, 10119. (c) Harrowven, D. C.; Sutton, B. J.; Coulton, S. *Tetrahedron* **2002**, *58*, 3387. (d) Majumdar, K. C.; Basu, P. K.; Chattopadhyay, S. K. *Tetrahedron* **2007**, *63*, 793.

(10) (a) Zettler, F.; Hausen, H. D.; Hess, H. *J. Organomet. Chem.* **1974**, *72*, 157. (b) Blount, J. F.; Finocchiaro, P.; Gust, D.; Mislow, K. *J. Am. Chem. Soc.* **1973**, *95*, 7019. (c)

Olmstead, M. M.; Power, P. P. *J. Am. Chem. Soc.* **1986**, *108*, 4235.

(11) Nöth, H.; Wrackmeyer, B. *NMR Basic Principles and Progress, Vol. 14, Nuclear magnetic Resonance Spectroscopy of Boron Compounds,* Springer-Verlag, Berlin, New York, 1978.

(12) Wehmschulte, R. J.; Khan, M. A.; Twamley, B.; Schiemenz, B. *Organometallics* **2001**, *20*, 844.

(13) Geier, S. J.; Gille, A. L.; Gilbert, T. M.; Stephan, D. W. *Inorg. Chem.* **2009**, *48*, 10466.

(14) Wan, P.; Yates, K.; Boyd, M. K. *J. Org. Chem.* **1985**, *50*, 2881.

(15) (a) Irie, M. *J. Am. Chem. Soc.* **1983**, *105*, 2078. (b) Kimura, K.; Mizutani, R.; Yokoyama, M.; Arakawa, R.; Sakurai, Y. *J. Am. Chem. Soc.* **2000**, *122*, 5448. (c) Liu, H.; Xu, Y.; Li, F.; Yang, Y.; Wang, W.; Song, Y.; Liu, D. *Angew. Chem. Int. Ed.* **2007**, *46*, 2515. (d) Wang, B. C.; Chen, Q.; Xu, H.; Wang, Z.; Zhang, X. *Adv. Mater.* **2010**, *22*, 2553.

(16) Sheldrick, G. M. SHELX-97, *Program for the Refinement of Crystal Structures*; University of Göttingen: Göttingen, Germany, 1997.

(17) Weimar, M.; Dürner, G.; Bats, J. W.; Göbel, M. W. *J. Org. Chem.* **2010**, *75*, 2718.

(18) Gaussian 09 (Revision A.02), Frisch, M. J.; Trucks, G. W.; Schlegel, H. B.; Scuseria, G.E.; Robb, M. A.; Cheeseman, J. R.; Scalmani, G.; Barone, V.; Mennucci, B.; Petersson, G. A.; Nakatsuji, H.; Caricato, M.; Li, X.; Hratchian, H. P.; Izmaylov, A. F.; Bloino, J.; Zheng, G.; Sonnenberg, J. L.; Hada, M.; Ehara, M.; Toyota, K.; Fukuda, R.; Hasegawa, J.; Ishida, M.; Nakajima, T.; Honda, Y.; Kitao, O.; Nakai, H.; Vreven, T.; Montgomery, Jr., J. A.; Peralta, J. E.; Ogliaro, F.; Bearpark, M.; Heyd, J. J.; Brothers, E.; Kudin, K. N.;Staroverov, V. N.; Kobayashi, R.; Normand, J.; Raghavachari, K.; Rendell, A.; Burant, J. C.; Iyengar, S. S.; Tomasi, J.; Cossi, M.; Rega, N.; Millam, J. M.; Klene, M.; Knox, J. E.; Cross, J. B.; Bakken, V.; Adamo, C.; Jaramillo, J.; Gomperts, R.; Stratmann, R. E.; Yazyev, O.; Austin, A. J.; Cammi, R.; Pomelli, C.; Ochterski, J. W.; Martin, R. L.; Morokuma, K.; Zakrzewski, V. G.; Voth, G. A.; Salvador, P.; Dannenberg, J. J.; Dapprich,S.; Daniels, A. D.; Farkas, O.; Foresman, J. B.; Ortiz, J. V.; Cioslowski, J.; Fox, D. J. Gaussian, Inc., Wallingford CT, 2009.

(19) Matsuo, K.; Saito, S.; Yamaguchi, S. *J. Am. Chem. Soc.* **2014**, *136*, 12580.

Chapter 3

Solution-Processed Organic Thin-Film Transistor Fabrication of a Boron-Embedded Polycyclic Aromatic Hydrocarbon

Abstract: Boron-embedded polycyclic aromatic hydrocarbon (PAH) showed an increased solubility in a pyridine-containing solution. The spin coating of the solution gave thin films of thus formed Lewis acid–base complex and further thermal annealing gave a polycrystalline film of the boron-embedded PAH through a thermal dissociation of pyridine. Organic thin-film transistors prepared by this solution process displayed typical p-type characteristics.

3-1. Introduction

Solution-processable organic semiconductors are a crucial class of materials for achieving large-area, low-temperature, and low-cost fabrication of flexible devices in organic field-effect transistors (OFETs) and photovoltaics (OPVs).[1] Extended π-conjugated semiconductors, however, generally suffer from poor solubility in common organic solvents, which hampers the solution-processed device fabrication. One solution is to introduce solubilizing groups, such as long or branched alkyl chains[2] and bulky trialkylsilyl groups[3] to the π-skeletons. Connection of π-skeletons in a nonplanar fashion is also employed to improve the solubility.[4] The other promising strategy is to use soluble precursors of organic semiconductors, which furnish thermally or photochemically removable solubilizing groups.[5] Various types of soluble precursors are reported not only for small molecules, such as acenes,[6,7] benzoporphyrins,[8] and oligothiophenes,[9] but also for semiconducting polymers.[10] Conversions of these materials to the corresponding pristine semiconductors rely on several covalent-bond cleavage reactions, such as retro-Diels-Alder reaction,[6,8,10d] thermolysis of esters, amide or carbamate groups,[9,10a-c] and photoelimination of α-diketone[7] (Figure 3-1). The gradual generation of the pristine semiconductors in this method is also beneficial to gaining high crystallinity of the resulting thin film. Although this soluble precursor method is useful for the solution-processed device fabrication, a drawback is that such precursors often need more steps for the synthesis compared to the pristine π-conjugated materials.

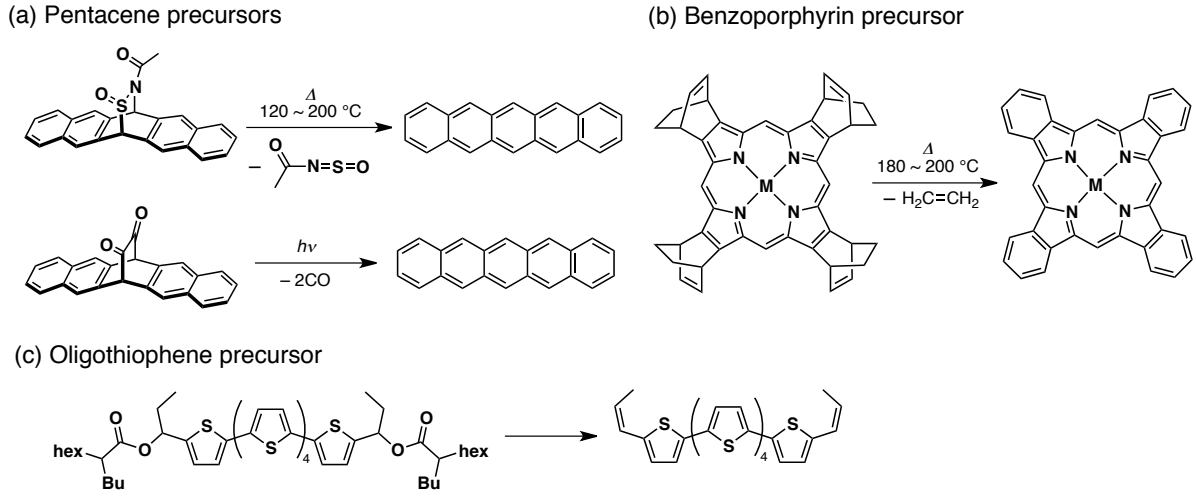

Figure 3-1. Examples of soluble precursors for (a) pentacene, (b) benzoporphyrin and (c) oligothiophene.

In chapter **1** and **2**, the author has synthesized boron-embedded PAHs **1**[11] and **2**[12] (Figure 3-2a). Despite the structural constraint of the boron atoms, these compounds maintain sufficient Lewis acidity and spontaneously form Lewis acid–base complexes even with

weakly basic pyridines. The B–N coordinate bonds, however, are labile and undergo dissociation in solution upon heating or photoirradiation, resulting in showing thermochromism[11] and dual fluorescence.[12] The author envisioned that this dynamic behavior of the Lewis acid–base complexes can be a mechanism to interconvert between semiconducting PAH materials and their soluble forms even in the solid state and thereby enables the solution-processed fabrication of organic thin-film transistors. In this chapter, the author describes a new concept for solution-processable organic semiconductors as an alternative to the soluble precursor method, namely a soluble dynamic complex strategy, which relies on a dynamic Lewis acid–base complex formation/dissociation behavior of boron-embedded PAH (Figure 3-2b). Notably, this strategy does not require any elaborate synthesis of the soluble precursors. Moreover, thermal annealing conditions to remove Lewis bases can be modulated by selecting pyridine derivatives with varied Lewis basicity.

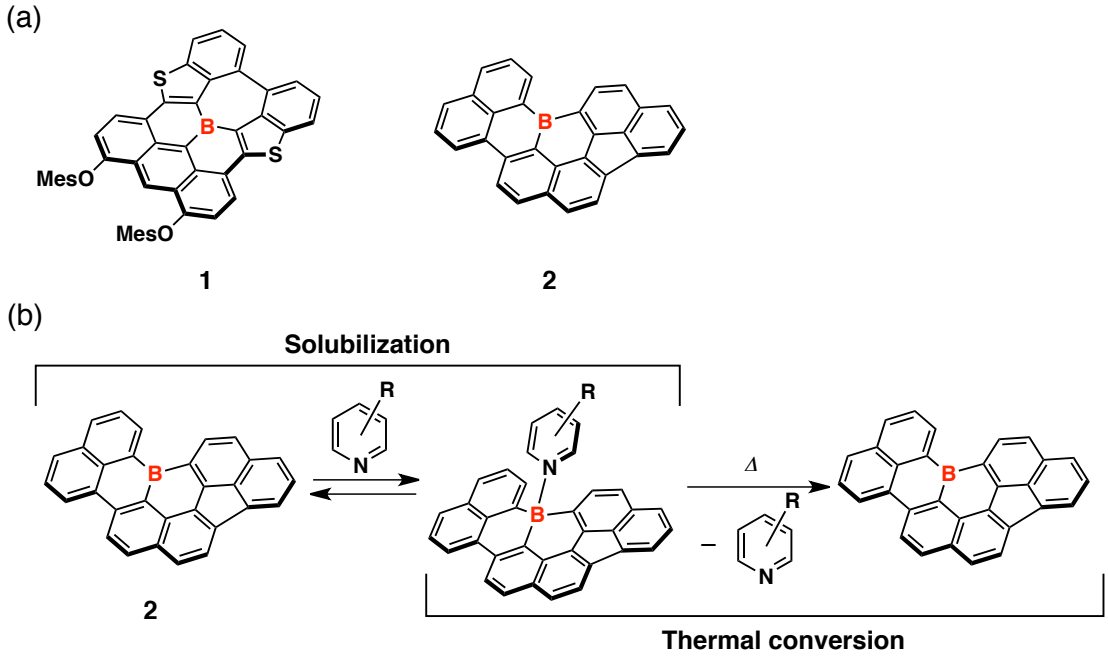

Figure 3-2. (a) Structures of boron-embedded PAHs and (b) dynamic behavior of soluble Lewis acid–base complex of boron-embedded PAH **2** and pyridine derivatives.

3-2. Results and discussion

Solubility

The author chose the partially fused trinaphthylborane **2** as a model compound to prove this concept. Despite the partially fused structure, this compound has a completely planar geometry and thereby forms a π-stacked columnar packing structure in the crystalline state. In chapter 2, the author has already confirmed that the vapor deposition of **2** enable the fabrication of OFET devices, in which compound **2** indeed acted as an active layer with a moderate hole mobility (9.3×10^{-6} cm^2 V^{-1} s^{-1}).[12] On the other hand, the partially fused structure also imparts relatively high Lewis acidity among the boron-embedded PAHs so far synthesized.[11,12,13] The association constant of **2** with pyridine is 5.1×10^3 M^{-1} in toluene at 25 °C. The coordination of pyridine to **2** converts the planar geometry to a bowl-shaped one and thereby prevents the formation of the π-stacked columnar structure.[12] This structural modification significantly improves the solubilities of **2** in various solvents (Table 3-1). The tricoordinate **2** has poor solubilities (< 1.0 gL^{-1}) in common organic solvents, such as chloroform, toluene and chlorobenzene, at room temperature, and its saturated concentrations in these solvents are lower than 0.1 wt%. In sharp contrast, **2** has a much higher solubility (14.8 gL^{-1}) in pyridine. The Saturated concentration in pyridine was significantly high of 1.5 wt%, which is much higher than 1 wt% concentration required for a spin-coating method in preparation.

Table 3-1. Solubilities of **2** in Various Solvents at Room Temperature

solvents	solubility / gL^{-1}	saturated concentration / wt%
$CHCl_3$	0.38	0.026
toluene	0.25	0.029
chlorobenzene	0.78	0.070
pyridine	14.8	1.5

Thermal analysis

The Lewis acid–base complex **2·Py** indeed showed the thermal dissociation even in the solid state. The powdery sample of the Lewis acid–base complex was obtained by reprecipitation from a toluene solution of **2** in the presence of an excess pyridine by the addition of hexane. Thus obtained orange powder did not change in color even after drying in vacuo at room temperature for several hours. The thermal stability of the solid material was investigated by the thermogravimetric analysis (TGA) (Figure 3-3). Upon increasing the

temperature, the first weight loss of 18% was observed at 133 °C, which should correspond to the complete release of pyridine from **2·Py** (theoretically 17%). The second weight loss was observed around 380 °C, which likely results from the decomposition of **2** (5% weight loss temperature T_{d5} = 384 °C).[12] This result indicated that pyridine could be completely removed from the Lewis acid–base complex **2·Py** in the solid state by simple heating without decomposition.

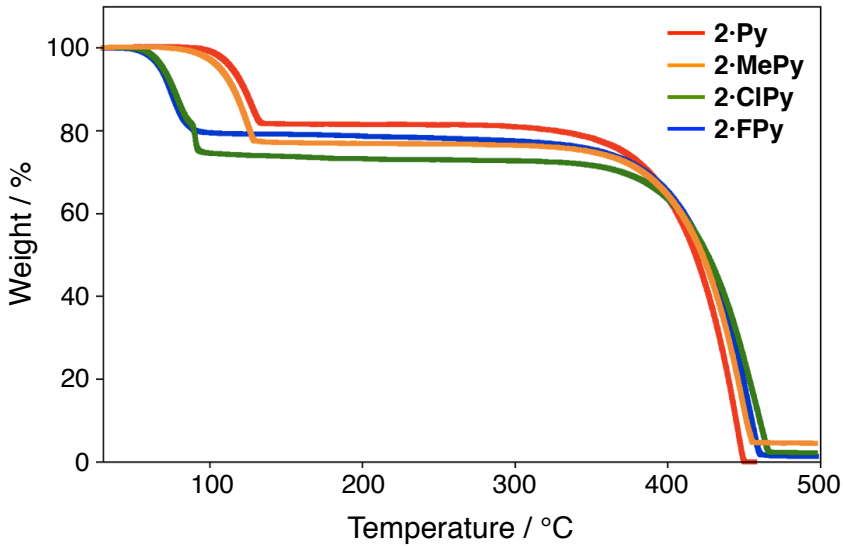

Figure 3-3. TGA profiles of Lewis acid–base complexes of **2** with various pyridine derivatives. The analysis were performed under nitrogen atmosphere with a heating rate of 5 °C min^{-1}.

It should be noted that the Lewis base-releasing temperature is dependent on the Lewis basicity of the coordinating bases. The Lewis acid–base complexes of **2** with various other pyridine derivatives, including 4-methylpyridine (MePy), 3-chloropyridine (ClPy), and 3-fluoropyridine (FPy), were obtained in a similar manner to that with pyridine and their thermal behavior was monitored by the TGA (Figure 3-3). The first-step weight losses of 23%, 25% and 21% were observed for the Lewis acid–base complexes of **2** with MePy, ClPy and FPy, respectively, which were in good agreement with the release of the corresponding Lewis bases. The weight loss temperatures varied in the order of 133 °C, 129 °C, 92 °C and 86 °C for Py, MePy, ClPy and FPy, respectively. The weaker Lewis bases, ClPy and FPy, are more easily released than Py and MePy, despite the higher boiling point of ClPy (155 °C) compared to Py (115 °C). This result indicated the weight loss temperature is correlated with their Lewis basicity rather than their boiling point. It is also noteworthy that the weight loss temperature of 86 °C for **2·FPy** is much lower than those of typical soluble pentacene precursors that undergo retro-Diels- Alder reaction (120–200 °C).[5b]

Photophysical properties of thin film

The thin film of **2·Py** was prepared on the glass substrate by the spin-coating method using a chloroform solution of **2** (1 wt%) containing 1 wt% of pyridine as an additive at 2000 rpm for 30 sec in air. UV-Vis absorption spectrum of the spin-coated film of **2·Py** on the glass substrate showed a strong absorption band at 360 nm and a weak absorption band at 450 nm, similar to that obtained in toluene (Figure 3-4). Upon annealing of the film at 180 °C, the absorbance in the visible region gradually increased and the absorption onset reached 615 nm (Figure 3-5). After annealing for 5 min, the absorption spectrum of the film eventually became similar to that of the vapor-deposited film of **2**, indicative of the successful thermal conversion of Lewis acid–base complex **2·Py** into pristine **2** even in the thin film on the substrate.

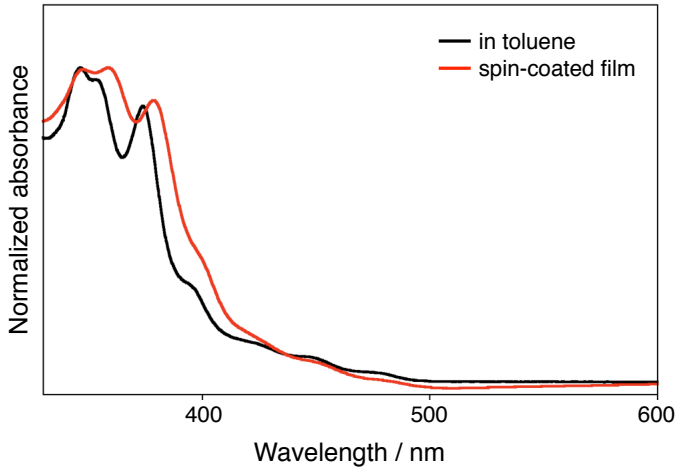

Figure 3-4. UV-Vis absorption spectra of a toluene solution of **2** in the presence of pyridine ($[\mathbf{2}]_0$ = 3.4 × 10^{-5} M, $[Py]_0$ = 4.2 × 10^{-2} M, black line) and a spin-coated film on the glass substrate (red line) of **2·Py**.

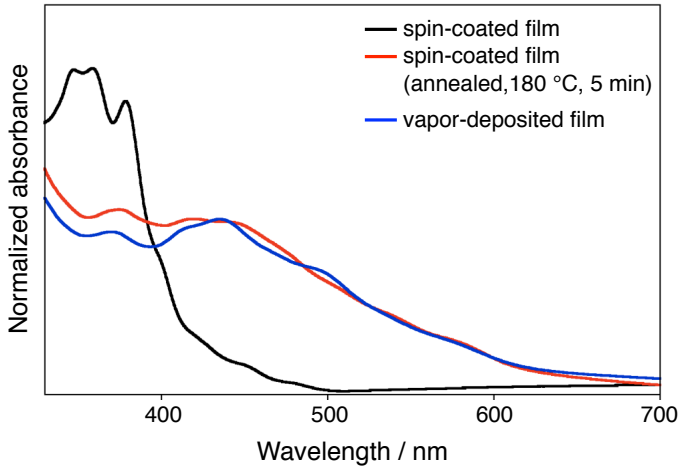

Figure 3-5. UV-Vis absorption spectra of a spin-coated film of **2·Py** before (black line) and after annealing at 180 °C for 5 min (red line), and of a vapor-deposited film of **2** (blue line).

The optical band gap (E_g) of thus prepared film of **2** was estimated to be 2.02 eV from the absorption onset. The ionization potential (I_p) of **2** in the thin film was also determined to be 5.61 eV by photoelectron spectroscopy of the vapor-deposited film in air (Figure 3-6). The electron affinity (E_a) was estimated from the I_p and E_g values to be 3.59 eV, which is comparable to that of 3.62 eV estimated from its reduction potential (–1.48 V vs. Fc/Fc^+ in THF)[12] determined by cyclic voltammetry.[14] This electronic structure, particularly its high I_p value, suggests the suitability of **2** for the use as an air-stable p-type OFET material.

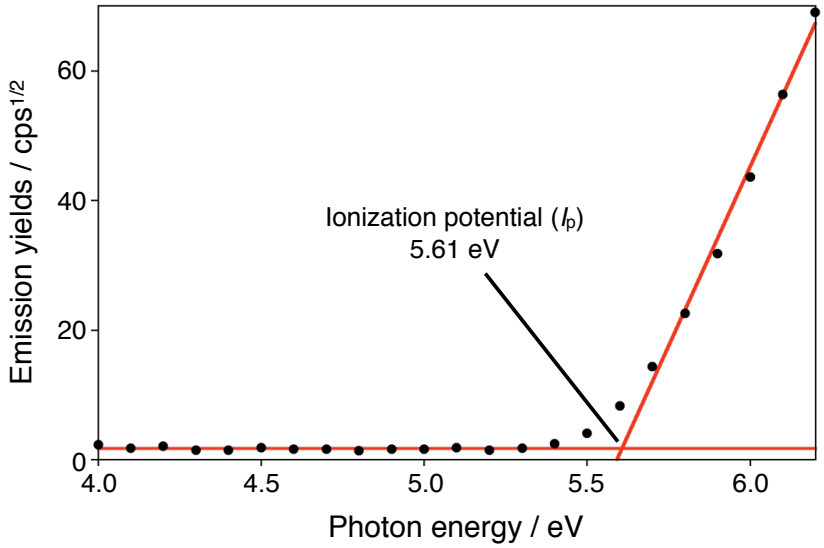

Figure 3-6. Photoelectron spectrum of a vapor-deposited film of **2** on the ITO glass substrate.

Film morphology

The surface morphology of the spin-coated film on the Si/SiO_2 substrate was studied by out-of-plane X-ray diffraction analysis. The thin film of **2·Py** on the Si/SiO_2 was prepared substrate by spin-coating method using a chloroform solution of **2** (0.5 wt%) containing 1 wt% of pyridine as an additive at 2000 rpm for 30 sec in air. The as-coated film of **2·Py** was amorphous in light of the fact that it did not show any diffraction peaks (Figure 3-7). Upon gradual heating, several diffraction peaks appeared at 180 °C, indicative of the formation of crystalline phase. After further heating at 200 °C for 5 min, diffraction intensity did not change. These results indicated that the annealing temperature at 180 °C was required for the crystallization despite the lower Lewis base-releasing temperature of 133 °C observed by TGA of **2·Py**. The observed diffraction pattern, however, was not identical to that of a crystalline powdery sample of **2** prepared by sublimation, indicating the formation of a thin-film phase with different crystal lattice parameters. Moreover, the almost same diffraction pattern was observed in the spin-coated film of **2** prepared through **2·Py** by direct

increase in temperature at 180 °C although the relative peak intensity was different (Figure 3-8).

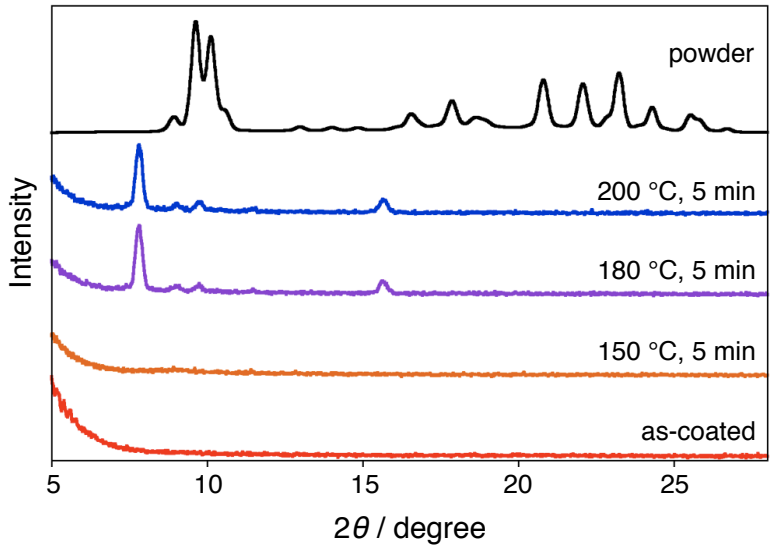

Figure 3-7. Out-of-plane XRD spectral change of a spin-coated film of **2·Py** on the Si/SiO_2 substrate upon gradual heating in air and XRD diffraction pattern of sublimated powder of **2**.

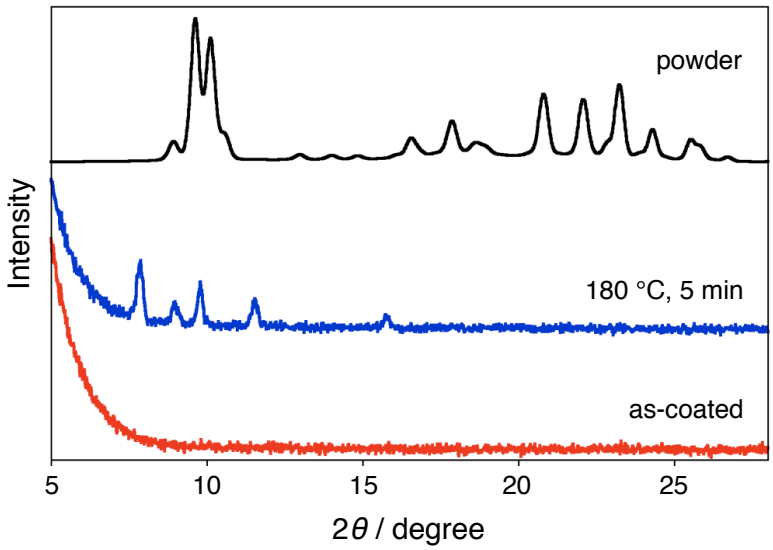

Figure 3-8. Out-of-plane XRD spectral change of a spin-coated film of **2·Py** on the Si/SiO_2 substrate before (red line) and after annealing at 180 °C for 5 min (blue line) and XRD diffraction pattern of sublimated powder of **2** (black line).

Crystallization upon thermal annealing was also confirmed by optical microscope images (Figure 3-9). While the as-coated film on the Si/SiO_2 substrate using a **2·Py** solution showed uniform and smooth surface, the annealed film showed small crystal domains with birefringence through the polarized filter. The roughness of the film morphology was

assessed by atomic force microscope (AFM) (Figure 3-10). The annealed film exhibited a polycrystalline rough surface with significant boundaries among rod-like crystallites. The root mean square roughness was 15.1 nm and the crystallites were randomly oriented. The formation of the crystalline thin-film by annealing of the spin-coated film of **2·Py** is in contrast to the fact that the direct vapor deposition of **2** gave an amorphous film without showing any diffraction peaks (Figure 3-11).

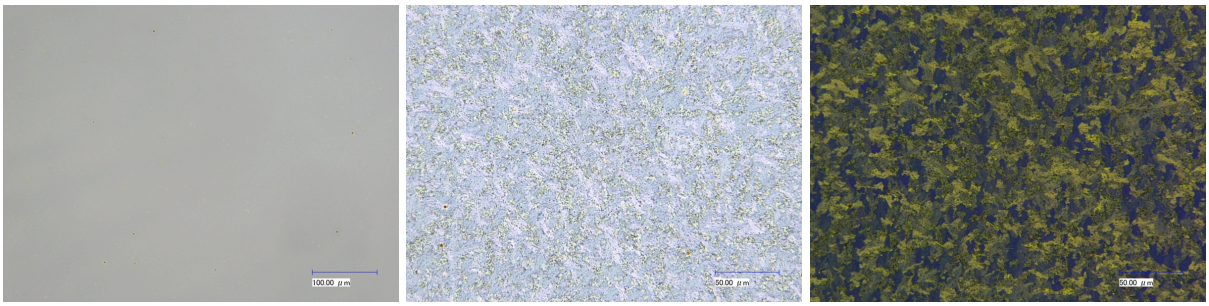

Figure 3-9. Optical microscope images of surface morphology of the spin-coated film of **2·Py** on the Si/SiO_2 substrate.

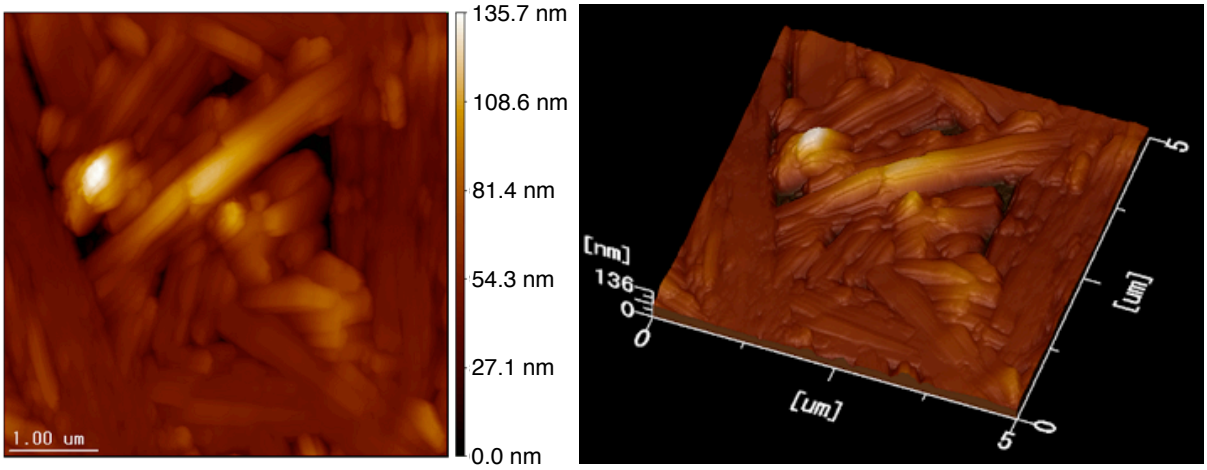

Figure 3-10. AFM images of a spin-coated film of **2** converted from **2·Py** on the Si/SiO_2 substrate after annealing at 180 °C for 5 min. The root mean square roughness was evaluated to be 15.1 nm.

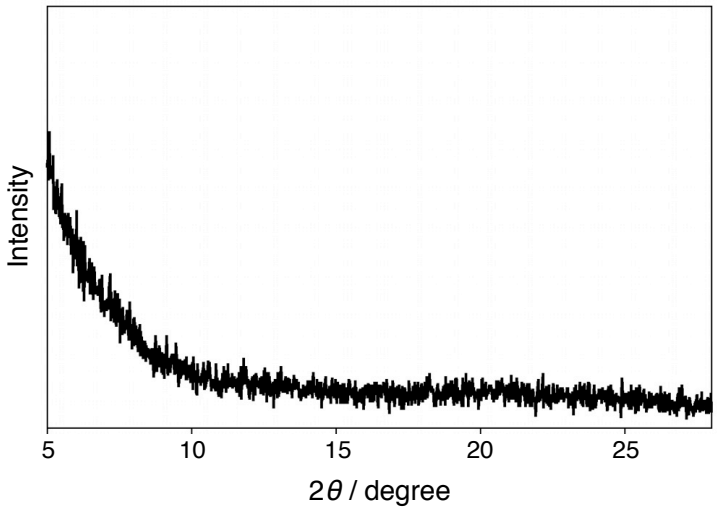

Figure 3-11. Out-of-plane XRD spectrum of a vapor-deposited film of **2** on the Si/SiO_2 substrate.

OFET characteristics

The bottom-gate top-contact OFET devices were fabricated using a heavily n-doped Si substrate with 100-nm thermally grown SiO_2 film as a gate insulator. The SiO_2 surface was treated with hexamethyldisilazanw (HMDS). A chloroform solution of **2** (0.5 wt%) containing 1 wt% of pyridine was spin-coated on the substrate for 30 sec at 2000 rpm in air. Thus obtained spin-coated films were annealed at 180 °C for 5min in air to remove pyridine. Then, gold electrodes (50 nm thickness) were vacuum-deposited as the source and drain on top of the organic thin films through a shadow mask. The drain-source channel length (L) and width (W) were 20 μm and 200 μm, respectively. FET properties were measured with an Agilent Technologies B1500A semiconducting parameter analyzer in air. The solution-processed OFETs of **2** prepared through **2·Py** exhibited typical p-type FET characteristics (Figure 3-12). The field-effect mobility (μ_{FET}) was calculated in the saturation regime (V_d = –60 V) of the I_d using the following equation,

$$I_d = (WC_i / 2L)\, \mu_{FET}\, (V_g - V_{th})^2$$

where I_d is the drain–source current, C_i is the capacitance of the SiO_2 insulator, and V_d, V_g and V_{th} are the drain–source, gate and threshold voltages, respectively. The best μ_{FET} was 2.5×10^{-4} cm^2 V^{-1} s^{-1} (average μ_{FET} was 1.7×10^{-4} cm^2 V^{-1} s^{-1}) with an on/off current ratio (I_{on}/I_{off}) of 9×10^3 and a V_{th} of –12.3 V. The hole mobility is superior to that of the vapor-deposited film previously reported (9.3×10^{-6} cm^2 V^{-1} s^{-1} for hole)[12] probably due to the higher crystallinity according to the X-ray diffraction analysis.

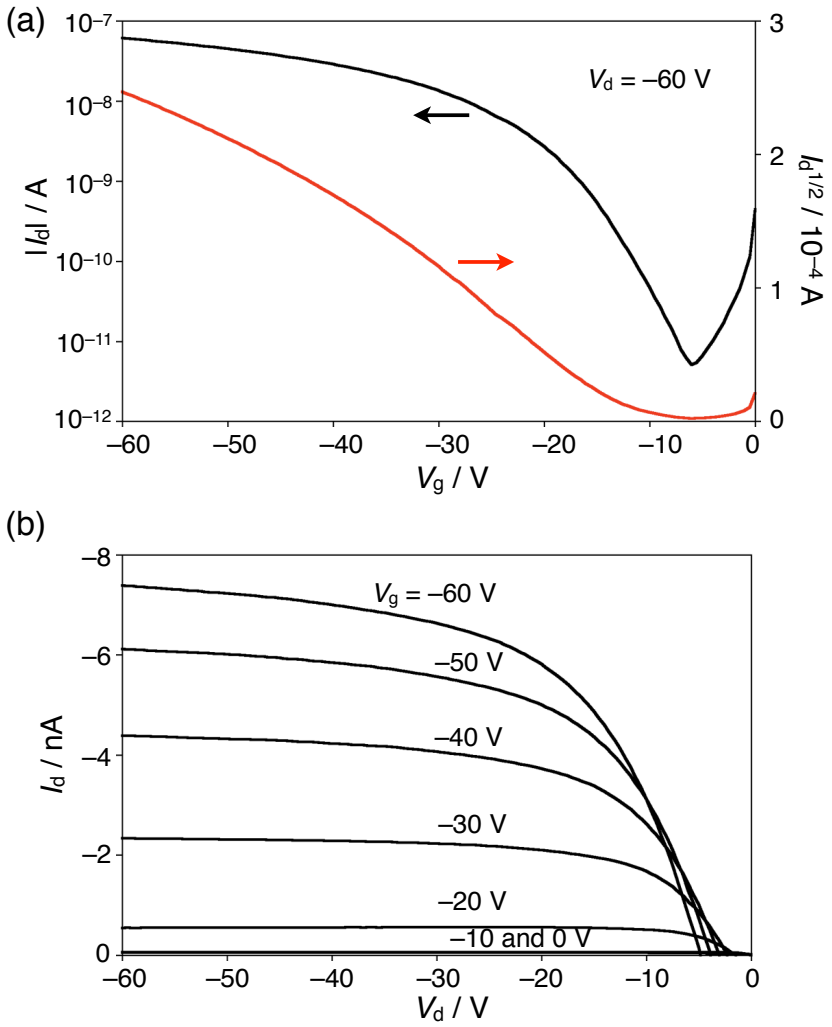

Figure 3-12. OFET characteristics of **2** prepared through **2·Py**: (a) Transfer curves in the saturation regime and (b) output curves at a different V_g for p-channel.

Finally, the influence of Lewis bases for thin-film fabrication was investigated. Thin films of **2·MePy** were prepared in the same manner as that for **2·Py**. A chloroform containing 1 wt% of MePy was used as solvent in stead of that containing pyridine. UV-Vis absorption spectrum of the spin-coated film of **2·MePy** on the glass substrate showed similar spectral change upon annealing of the film at 180 °C (Figure 3-13). Absorption spectrum after annealing was almost identical to that of **2** prepared from **2·Py**, indicative of the similar thermal conversion of Lewis acid–base complex **2·MePy** into pristine **2** in the thin film on the substrate. Moreover, the conversion into the polycrystalline film upon thermal annealing was also confirmed by XRD analysis, optical microscope and AFM. The as-coated film of **2·MePy** was also amorphous, which did not show any diffraction peak (Figure 3-14). After annealing of the substrate at 180 °C for 5 min, one diffraction peak appeared. This result suggested the formation of the crystalline film. The microscope images of **2·MePy** exhibited

similar surface morphology change to that of **2·Py** (Figure 3-15). The AFM image showed the rough polycrystalline surface with rod-like crystallites (Figure 3-16). The root mean square roughness was 25.6 nm and the crystallites were randomly oriented. In addition, The OFETs prepared from **2·MePy** Lewis acid–base complex displayed comparable p-type FET performance to those prepared from **2·Py** (Figure 3-17). The best μ_{FET} was 3.0×10^{-4} cm^2 V^{-1} s^{-1} (average μ_{FET} was 1.7×10^{-4} cm^2 V^{-1} s^{-1}) with an on/off current ratio (I_{on}/I_{off}) of 1.4×10^3 and a V_{th} of –11.9 V. On the other hand, the thin films of **2·ClPy** and **2·FPy** were unsuccessfully obtained.

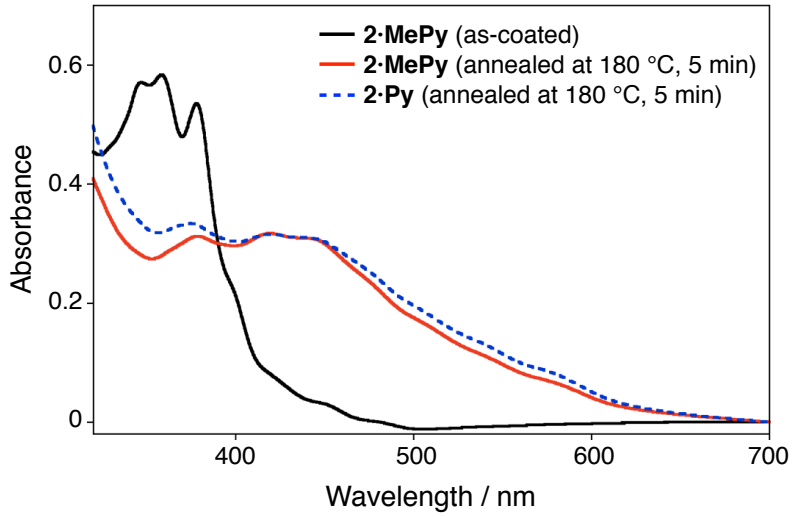

Figure 3-13. UV-Vis absorption spectra of the spin-coated film of **2·MePy** on the glass substrate before (black solid line) and after annealing at 180 °C for 5 min (red solid line), and the spin-coated film of **2·Py** after annealing at 180 °C at 5 min (blue dashed line).

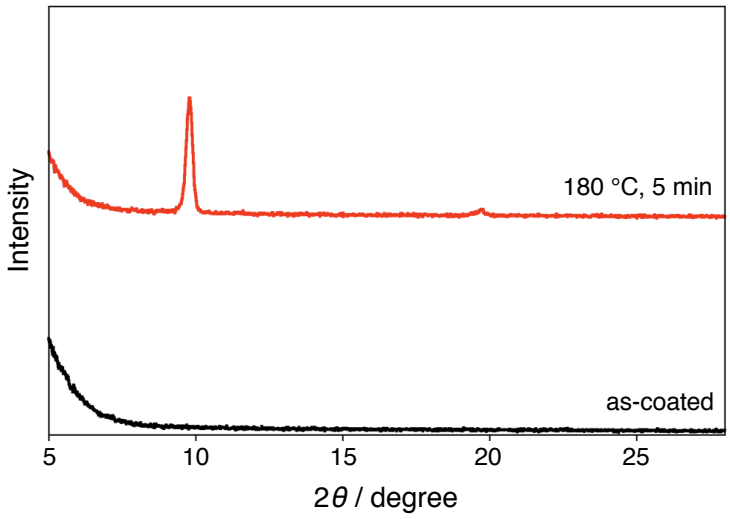

Figure 3-14. Out-of-plane XRD spectral change of a spin-coated film of **2·MePy** on the Si/SiO_2 substrate before (black line) and after annealing at 180 °C for 5 min (red line).

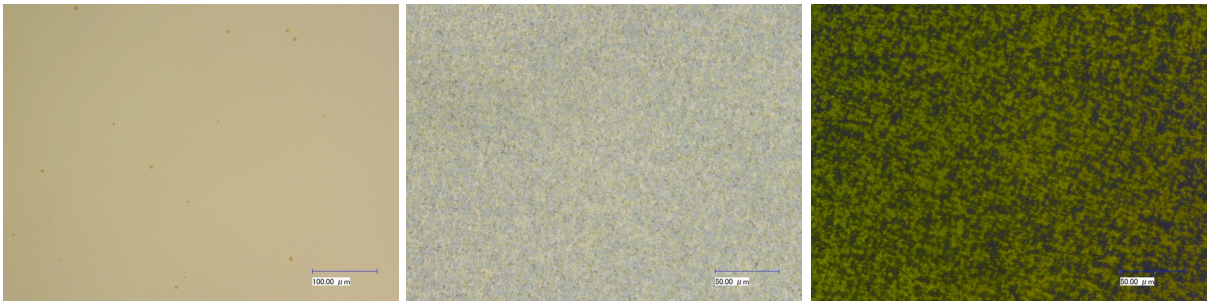

as-coated | after annealing at 180 °C for 5 min | after annealing at 180 °C for 5 min (polarized filter)

Figure 3-15. Optical microscope images of surface morphology of the spin-coated film of **2·MePy** on the Si/SiO_2 substrate.

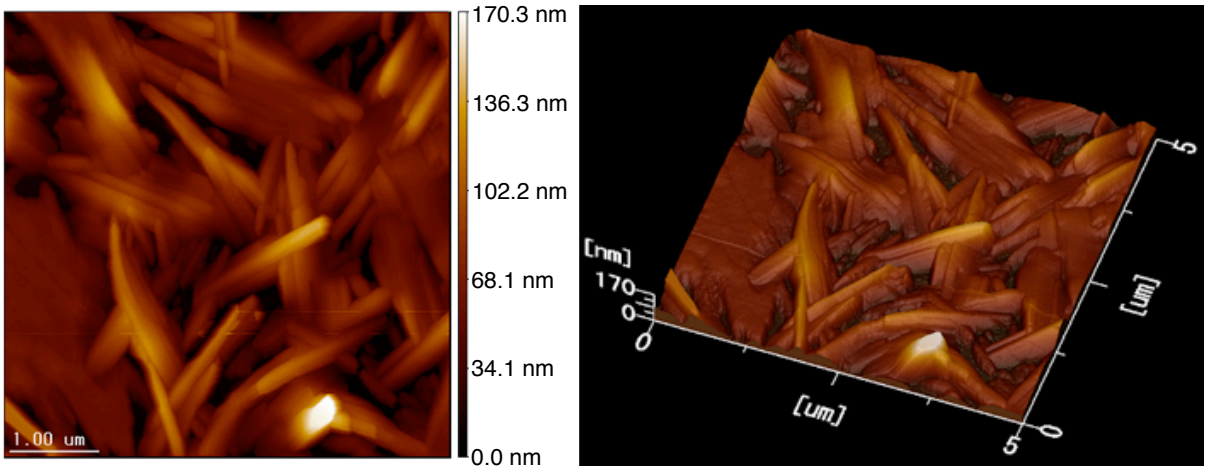

Figure 3-16. AFM images of a spin-coated film of **2** converted from **2·MePy** on the Si/SiO_2 substrate after annealing at 180 °C for 5 min. The root mean square roughness was evaluated to be 25.6 nm.

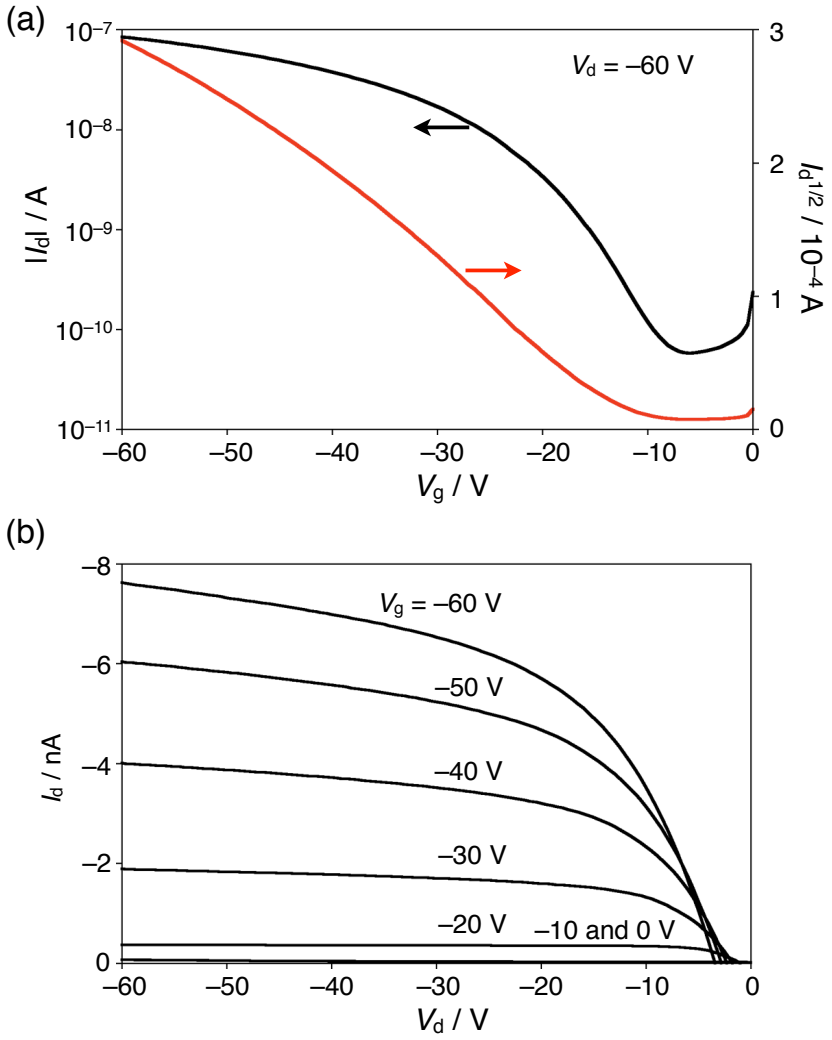

Figure 3-17. OFET characteristics of **2** prepared through **2·MePy**: (a) Transfer curves in the saturation regime and (b) output curves at different V_g for p-channel.

3-3. Conclusion

The author demonstrated a new concept of solution-processable OFET fabrication based on the dynamic Lewis acid–base complex formation/dissociation processes of a boron-embedded PAH. The solubility of the planar π-electron compound was drastically enhanced by addition of Lewis basic pyridines. Thin films of the Lewis acid–base complexes were prepared by the spin-coating method, which were converted to polycrystalline films of the pristine boron-embedded PAH by simple annealing with the release of the Lewis bases. Top-contact FET of **2** fabricated in this method displayed a typical p-type characteristic with a better hole mobility of 2.5×10^{-4} cm^2 V^{-1} s^{-1} than that of vapor-deposited FET. Although the device performance still needs further optimization, this proof-of-concept study clearly demonstrate the unique utilization of the boron-doped PAHs and would stimulate further study of the boron-embedded PAH from an application point of view to organic electronics.[15]

3-4. Experimental section

General

Thermogravimetric analysis (TGA) was performed using Seiko TGA6200 at a heating rate of 5 °C min^{-1} under a nitrogen atmosphere. UV-visible absorption spectra were recorded on a Shimadzu UV-3150 or UV-3600plus spectrometer. Photoelectron spectrum of thin film was recorded on a Model AC-2 photoelectron spectrometer (RIKEN KEIKI Co., Ltd.) in air. Ionization potential I_p was determined from the onset potential of the photoelectron spectrum. X-ray diffraction measurements of thin films were performed with a Rigaku Smartlab X-ray diffractometer with a CuKα source (λ = 1.5418 Å). Powder X-ray diffraction measurement was performed with a Rigaku R-AXIS VII X-ray diffractometer with a CuKα source (λ = 1.5418 Å). Optical microscope images were obtained with KEYENCE VHX-600. Dynamic mode atomic force microscopic images were obtained with JEOL JSPM-5200 by using a canti-lever, NSC35 (μ-mash). Commercially available solvents and reagents were used without further purification. Compound **2** was prepared according to the literature.[12]

Preparation of thin films of 2 using various pyridine derivatives.

To the precisely weighted compound **2** (ca. 2 mg), corresponding amount of chloroform containing 1 wt% of pyridine (ca. 270 μL) was added to afford 0.5 wt% solution of **2·Py**. On the Si/SiO_2 substrate (ca. 10 mm × 10 mm of size), this solution (50 μL) was casted and the substrate was immediately spun at 2000 rpm for 30 sec to afford the thin film of **2·Py**.

Thin films of **2·MePy** were prepared in the same manner as described for **2·Py**. A chloroform containing 1 wt% of MePy was used as solvent in stead of that containing pyridine.

Preparations of the thin films of **2·ClPy** and **2·FPy** were failed because a large amount of less Lewis basic ClPy and FPy (> 10 wt%) were required to solubilize 1 wt% of **1** in chloroform. Thin films were not obtained using those solutions in any concentrations (0.5, 1.0 or 1.3 wt%) of 1 and or any spin rate of the substrates.

Preparation of thin films by vapor-deposition method

The vapor-deposited films (50 nm thickness) of **2** on the glass, ITO glass and Si/SiO_2 substrates were prepared at a rate of 1 Å s^{-1} under the pressure of ~1×10^{-3} Pa for UV-Vis absorption spectroscopy, photoelectron spectroscopy and XRD analysis, respectively.

Device fabrication and evaluation of FET performance

Organic field effect transistors (OFET) in a bottom-gate top-contact configuration were fabricated on a heavily doped n^+-Si (100) wafer with a 100-nm thermally grown SiO_2 film (C_i = 34.5 nF cm^{-2}). The SiO_2 surface was treated with hexamethyldisilazane (HMDS). The thin films of **2·Py** and **2·MePy** were prepared by spin-coating method using a chloroform solution of **2** (0.5 wt%) containing 1 wt% of pyridine or 4-methylpyridine at 2000 rpm for 30 sec in air. The spin-coated films were annealed at 180 °C for 5 min in air to remove Lewis bases. On top of the organic thin film, gold films (50 nm) were deposited as drain and source electrodes through a shadow mask at a rate of 0.5 Å s^{-1} under the pressure of ~1×10^{-3} Pa. The drain-source channel length (L) and width (W) were 20 μm and 200 μm, respectively. Characteristics of the OFET devices were measured at room temperature in air using an Agilent Technologies B1500A semiconducting parameter analyzer. The field-effect mobility (μ_{FET}) was calculated in the saturation regime (V_d = –60 V) of the I_d using the following equation,

$$I_d = (WC_i / 2L)\, \mu_{FET}\, (V_g - V_{th})^2$$

where I_d is the drain–source current, C_i is the capacitance of the SiO_2 insulator, and V_d, V_g, and V_{th} are the drain–source, gate and threshold voltages, respectively. Current on/off ratio (I_{on}/I_{off}) was determined from the I_d at V_g = –5 V (I_{on}) and V_g = –60 V (I_{off}).

References

(1) (a) Anthony, J. E. *Chem. Rev.* **2006**, *106*, 5028. (b) Allard, S.; Forster, M.; Souharce, B.; Thiem, H.; Scherf, U. *Angew. Chem. Int. Ed.* **2008**, *47*, 4070. (c) Mas-Torrent, M.; Rovira, C. *Chem. Soc. Rev.* **2008**, *37*, 827. (d) Facchetti, A. *Chem. Mater.* **2011**, *23*, 733. (e) Beaujuge, P. M.; Fréchet, J. M. J. *J. Am. Chem. Soc.* **2011**, *133*, 20009. (f) Mishra, A.; Bäuerle, P. *Angew. Chem. Int. Ed.* **2012**, *51*, 2020. (g) Wang, C.; Dong, H.; Hu, W.; Liu, Y.; Zhu, D. *Chem. Rev.* **2012**, *112*, 2208. (h) Lin, Y.; Li, Y.; Zhan, X. *Chem. Soc. Rev.* **2012**, *41*, 4245. (i) Mei, J.; Diao, Y.; Appleton, A. L.; Fang, L.; Bao, Z. *J. Am. Chem. Soc.* **2013**, *135*, 6724.

(2) (a) Ebata, H.; Izawa, T.; Miyazaki, E.; Takimiya, K.; Ikeda, M.; Kuwabara, H.; Yui, T. *J. Am. Chem. Soc.* **2007**, *129*, 15732. (b) Gao, P.; Beckmann, D.; Tsao, H. N.; Feng, X. Enkelmann, V.; Baumgarten, M.; Pisula, W.; Müllen, K. *Adv. Mater.* **2009**, *21*, 213. (c) Mitsui, C.; Soeda, J.; Miwa, K.; Tsuji, H.; Takeya, J.: Nakamura, E. *J. Am. Chem. Soc.* **2012**, *134*, 5448. (d) Mitsui, C.; Okamoto, T.; Yamagishi, M.; Tsurumi, J.; Yoshitomi, K.; Nakahara, K.; Soeda, J.; Hirose, Y.; Sato, H.; Yamano, A.; Uemura, T. Takeya, J. *Adv. Mater.* **2014**, *26*, 4546. (e) Jones, B. A.; Ahrens, M. J.; Yoon, M.-H.; Facchetti, A.; Marks, T. J.; Wasielewski, M. R. *Angew. Chem. Int. Ed.* **2004**, *43*, 6363. (f) Handa, S.; Miyazaki, E.; Takimiya, K.; Kunugi, Y. *J. Am. Chem. Soc.* **2007**, *129*, 11684.

(3) (a) Anthony, J. E.; Brooks, J. S.; Eaton, D. L.; Parkin, S. R. *J. Am. Chem. Soc.* **2001**, *123*, 9482. (b) Anthony, J. E.; Eaton, D. L.; Parkin, S. R. *Org. Lett.* **2002**, *4*, 15. (c) Sheraw, C. D.; Jackson, T. N.; Eaton, D. L.; Anthony, J. E. *Adv. Mater.* **2003**, *15*, 2009. (d) Payne, M. M.; Parkin, S. R.; Anthony, J. E.; Kuo, C.-C.; Jackson, T. N. *J. Am. Chem. Soc.* **2005**, *127*, 4986.

(4) (a) Zen, A.; Bilge, A.; Galbrecht, F.; Alle, R.; Meerholz, K.; Grenzer, J.; Neher, D.; Scherf, U.; Farrell, T. *J. Am. Chem. Soc.* **2006**, *128*, 3914. (b) Bilge, A.; Zen, A.; Forster, M.; Li, H.; Galbrecht, F.; Nehls, B. S.; Farrell, T.; Neher, D.; Scherf, U. *J. Mater. Chem.* **2006**, *16*, 3177. (c) Ponomarenko, S. A.; Tatarinova, E. A.; Muzafarov, A. M.; Kirchmeyer, S.; Brassat, L.; Mourran, A.; Moeller, M.; Setayesh, S.; de Leeuw, D. *Chem. Mater.* **2006**, *18*, 4101. (d) Roquet, S.; de Bettignies, R.; Leriche, P.; Cravino, A.; Roncali, J. *J. Mater. Chem.* **2006**, *16*, 3040.

(5) (a) Yamada, H.; Okujima, T.; Ono, N. *Chem. Commun.* **2008**, 2957. (b) Watanabe, M.; Chen, K.-Y.; Chang, Y. J.; Chow, T. J. *Acc. Chem. Res.* **2013**, *46*, 1606. (c) Suzuki, M.; Aotake, T.; Yamaguchi, Y.; Noguchi, N.; Nakano, H.; Nakayama, K.; Yamada, H. *J. Photochem. Photobiol. C* **2014**, *18*, 50.

(6) (a) Brown, A. R.; Pomp, A.; de Leeuw, A. M.; Klaassen, D. B. M.; Havinga, E. E.; Herwig, P.; Müllen, K. *J. Appl. Phys.* **1996**, *79*, 2136. (b) Herwig, P. T.; Müllen, K. *Adv. Mater.* **1999**, *11*, 480. (c) Afzali, A.; Dimitrakopoulos, C. D.; Breen, T. L. *J. Am. Chem. Soc.* **2002**, *124*, 8812. (d) Chen, K.-Y.; Hsieh, H.-H.; Wu, C.-C.; Hwang, J.-J.; Chow, T. J. *Chem. Commun.* **2007**, 1065. (e) Chao, T.-H.; Chang, M.-J.; Watanabe, M.; Luo, M.-H.; Chang, Y. J.; Fang, T.-C.; Chen, K.-Y.; Chow, T. J. *Chem. Commun.* **2012**, *48*, 6148. (f) Kimura, Y.; Nagase, T.; Kobayashi, T.; Hamaguchi, A.; Ikeda, Y.; Shiro, T.; Takimiya, K.; Naito, H. *Adv. Mater.* **2015**, *27*, 727.

(7) (a) Uno, H.; Yamashita, Y.; Kikuchi, M.; Watanabe, H.; Yamada, H.; Okujima, T.; Ogawa, T.; Ono, N. *Tetrahedron Lett.* **2005**, *46*, 1981. (b) Yamada, H.; Yamashita, Y.; Kikuchi, M.; Watanabe, H.; Okujima, T.; Uno, H.; Ogawa, T.; Ohara, K.; Ono, N. *Chem. Eur. J.* **2005**, *11*, 6212. (c) Chuang, T.-H.; Hsieh, H.-H.; Chen, C.-K.; Wu, C.-C.; Lin, C.-C.; Chou, P.-T.; Chao, T.-H.; Chow, T. J. *Org. Lett.* **2008**, *10*, 2869. (d) Yamada, H.; Ohashi, C.; Aotake, T.; Katsuta, S.; Honsho, Y.; Kawano, H.; Okujima, T.; Uno, H.; Ono, N., Seki, S.; Nakayama, K. *Chem. Commun.* **2012**, *48*, 11136. (e) Yamada, H.; Yamaguchi, Y.; Katoh, R.; Motoyama, T.; Aotake, T.; Kuzuhara, D.; Suzuki, M.; Okujima, T.; Uno, H.; Aratani, N.; Nakayama, K. *Chem. Commun.* **2013**, *49*, 11638. (f) Nakayama, K.; Ohashi, C.; Oikawa, Y.; Motoyama, T.; Yamada, H. *J. Mater. Chem. C* **2013**, *1*, 6244. (g) Yamaguchi, Y.; Suzuki, M.; Motoyama, T.; Sugii, S.; Katagiri, C.; Takahira, K.; Ikeda, S.; Yamada, H.; Nakayama, K. *Sci. Rep.* **2014**, *4*, 7151.

(8) (a) Aramaki, S.; Sakai, Y.; Ono, N. *Appl. Phys. Lett.* **2004**, *84*, 2085. (b) Hirao, A.; Akiyama, T.; Okujima, T.; Yamada, H.; Uno, H.; Sakai, Y.; Aramaki, S.; Ono, N. *Chem. Commun.* **2008**, 4714. (c) Matsuo, Y.; Sato, Y.; Niinomi, T.; Soga, I.; Tanaka, H.; Nakamura, E. *J. Am. Chem. Soc.* **2009**, *131*, 16048. (d) Saeki, H.; Kurimoto, O.; Nakaoka, H.; Misaki, M.; Kuzuhara, D.; Yamada, H.; Ishida, K.; Ueda, Y. *J. Mater. Chem. C* **2014**, *2*, 5357.

(9) (a) Murphy, A. R.; Fréchet, J. M.; Chang, P.; Lee, J.; Subramanian, V. *J. Am. Chem. Soc.* **2004**, *126*, 1596. (b) Murphy, A. R.; Chang, P.; VanDyke, P.; Liu, J.; Fréchet, J. M.; Subramanian, V.; DeLongchamp, D. M.; Sambasivan, S.; Fischer, D. A.; Lin, E. K. *Chem. Mater.* **2005**, *17*, 6033.

(10) (a) Liu, J.; Kadnikova, E. N.; Liu, Y.; McGehee, M. D.; Fréchet, J. M. *J. Am. Chem. Soc.* **2004**, *126*, 9486. (b) Lee, J.; Han, A.-R.; Hong, J.; Seo, J. H.; Oh, J. H.; Yang, C. *Adv. Funct. Mater.* **2012**, *22*, 4128. (c) Sun, B.; Hong, W.; Aziz, H.; Li, Y. *J. Mater. Chem.* **2012**, *22*, 18950. (d) Uemura, T.; Mamada, M.; Kumaki, D.; Tokito, S. *ACS*

Macro Lett. **2013**, **2**, 830.

(11) Saito, S.; Matsuo, K.; Yamaguchi, S. *J. Am. Chem. Soc*. **2012**, *134*, 9130.

(12) Matsuo, K.; Saito, S.; Yamaguchi, S. *J. Am. Chem. Soc*. **2014**, *136*, 12580.

(13) (a) Dou, C.; Saito, S.; Matsuo, K.; Hisaki, I.; Yamaguchi, S. *Angew. Chem. Int. Ed*. **2012**, *51*, 12206. (b) Osumi, S.; Saito, S.; Dou, C.; Matsuo, K. Kume, K.; Yoshikawa, H.; Awaga, K.; Yamaguchi, S. *Chem. Sci*. **2016**, *7*, 219.

(14) Cardona, C. M.; Li, W.; Kaifer, A. E.; Stockdale, D.; Bazan, G. C. *Adv. Mater*. **2011**, *23*, 2367.

(15) (a) Noda, T.; Shirota, Y. *J. Am. Chem. Soc*. **1998**, *120*, 9714. (b) Tanaka, D.; Takeda, T.; Chiba, T.; Watanabe, S.; Kido, J. *Chem. Lett*. **2007**, *36*, 262. (c) Numata, M.; Yasuda, T.; Adachi, C. *Chem. Commun*. **2015**, *51*, 9443. (d) Kitamoto, Y.; Namikawa, T.; Ikemizu, D.; Miyata, Y.; Suzuki, T.; Kita, H.; Sato, T.; Oi, S. *J. Mater. Chem. C* **2015**, *3*, 9122. (e) Hirai, H.; Nakajima, K.; Nakatsuka, S.; Shiren, K.; Ni, J.; Nomura, S.; Ikuta, T.; Hatakeyama, T. *Angew. Chem. Int. Ed*. **2015**, *54*, 13581. (f) Suzuki, K.; Kubo, S.; Shizu, K.; Fukushima, T.; Wakamiya, A.; Murata, Y.; Adachi, C.; Kaji, H. *Angew. Chem. Int. Ed*. 2015, *54*, 15231. (g) Kinoshita, M.; Fujii, N.; Tsuzuki, T.; Shirota, Y. *Synthetic Metals*, **2001**, *121*, 1571. (h) Cataldo, S.; Fabiano, S.; Ferrante, F.; Oreviti, F.; Patanè, S.; Pignataro, B. *Macromol. Rapid Commun*. **2010**, *31*, 1281.

Conclusion

In this thesis, the author has successfully developed the boron-embedded polycyclic π-electron systems, which can be regarded as the models of boron-doped graphene. These molecules exhibit not only high stability, but also intriguing properties and an unprecedented dynamic behavior reflecting characteristic features of the boron atom, including strong electron-accepting ability and Lewis acidity. In addition, they form an attractive molecular alignment in the solid state, which suggests a potential application to organic electronics. Throughout these studies, several important findings can be extracted, which are summarized as follow:

1. The boron-embedded polycyclic π-electron systems show not only high chemical stability toward oxygen and water but also high thermal stability despite the absence of steric protection around the boron atom. In particular, complete ring-fusion of the three aryl substituents on the boron atom is not necessary for gaining sufficient stability to be handled without special caution.
2. Connection among the three aryl groups on the boron atom directly with the $C(sp^2)$–$C(sp^2)$ bond produces polycyclic π-electron systems embedding a boron atom at the center, in which effective expanded π-conjugation gives rise to significant bathochromic shifts in their absorption and fluorescence, and higher electron-accepting abilities.
3. Highly planar structure of the boron-embedded polycyclic π-electron systems enables the formation of π-stacked array in the solid state, which is relevant to the charge transport properties as organic semiconducting material.
4. Despite their structural constraints, the boron-embedded polycyclic π-electron systems exhibit high Lewis acidity and spontaneously form Lewis acid-base adducts with Lewis bases, such as fluoride ion and pyridine. Moreover, the Lewis acidity can be modulated by tuning the structural flexibility around the boron atom.
5. The B–N coordinate bonds in the Lewis acid-base adducts are labile and the adducts exhibit dynamic behavior in solution. Heating and photoirradiation result in thermochromism and dual fluorescence, respectively.
6. Photodissociation of the B–N coordinate bond in the Lewis acid-base adducts is reminiscent of the photogeneration of carbenium ions from triarylmethane leuco dyes. Isoelectronic relationship between trivalent tricoordinate boron and carbenium ion is responsible for this similarity.
7. The dynamic behavior of the Lewis acid-base adduct is also useful for solution-processed fabrication of organic thin-film transistor with the boron-embedded

PAH.

These findings show new avenues in the organoboron chemistry, particularly directed toward materials science. The boron-embedded polycyclic π-electron systems are promising scaffolds for stimuli responsive materials and solution-processable organic semiconducting materials. Moreover the author believes that these results will contribute to the progress in the fundamental understanding for boron-doped graphene at the molecular level.

List of Publications

（副論文）

1. Polycyclic π-Electron System with Boron at its Center
Shohei Saito, Kyohei Matsuo, Shigehiro Yamaguchi
J. Am. Chem. Soc. **2012**, *134*, 9130.

2. Photodissociation of B–N Lewis Adducts: A Partially Fused Trinaphthylborane with Dual Fluorescence
Kyohei Matsuo, Shohei Saito, Shigehiro Yamaguchi
J. Am. Chem. Soc. **2014**, *136*, 12580.

（参考論文）

1. Boron-containing PAH as a Substructure of Boron-doped Graphene
Chuandong Dou, Shohei Saito, Kyohei Matsuo, Ichiro Hisaki, Shigehiro Yamaguchi
Angew. Chem. Int. Ed. **2012**, *51*, 12206.

2. Boron-doped Nanographene: Lewis Acidity, Redox Properties and Battery Electrode Performance
Shinichiro Osumi, Shohei Saito, Chuandong Dou, Kyohei Matsuo, Keita Kume, Hirofumi Yoshikawa, Kunio Awaga, Shigehiro Yamaguchi
Chem. Sci. **2016**, *7*, 219.